bioRxiv preprint doi: https://doi.org/10.1101/2022.04.03.486893; this version posted April 6, 2022. The copyright holder for this preprint (which was not certified by peer review) is the author/funder, who has granted bioRxiv a license to display the preprint in perpetuity. It is made available under aCC-BY 4.0 International license.

Non-cancer stem cell-derived Fibromodulin activates Integrin-dependent Notch signaling in endothelial cells to promote tumor angiogenesis and growth

Shreoshi Sengupta[1], Mainak Mondal[1], Kaval Reddy Prasasvi[1], Arani Mukherjee[1], Prerna Magod[2], Serge Urbach[4], Dinorah Friedmann-Morvinski[2,3*], Philippe Marin[4*] and Kumaravel Somasundaram[1*]

[1]Department of Microbiology and Cell Biology, Indian Institute of Science, Bangalore 560012, India; [2]School of Neurobiology, Biochemistry and Biophysics, The George S. Wise Faculty of Life Sciences, Tel Aviv University, Tel Aviv 69978, Israel; [3]Sagol School of Neuroscience, Tel Aviv University, Tel Aviv 69978, Israel, [4]Institut de Génomique Fonctionnelle, Université de Montpellier, CNRS, INSERM, Montpellier, France

* Corresponding authors

Tel: +91-80-23607171

Fax: +91-80-23602697

Email: KS: skumar1@iisc.ac.in; ksomasundaram1@gmail.com;

PM: philippe.marin@igf.cnrs.fr; DFM: dino@tauex.tau.ac.il

Running title: Differentiated cancer cell-derived FMOD promotes tumor growth

Conflict of Interest: The authors declare no potential conflicts of interest.

Keywords: Cancer stem-like cells, Differentiated bulk tumor cells, Glioma stem-like cells, Differentiated glioma cells, Fibromodulin, Angiogenesis, Glioblastoma

Abbreviations: FMOD, Fibromodulin; CSC, Cancer stem-like cell; GSC, Glioma stem-like cell; DGC, Differentiated glioma cell; GBM, Glioblastoma; CM, Conditioned medium; GSI, γ-secretase inhibitor, TDEC, Tumor derived endothelial cells; VM, Vascular mimicry

bioRxiv preprint doi: https://doi.org/10.1101/2022.04.03.486893; this version posted April 6, 2022. The copyright holder for this preprint (which was not certified by peer review) is the author/funder, who has granted bioRxiv a license to display the preprint in perpetuity. It is made available under aCC-BY 4.0 International license.

Abstract

Cancer stem cells alone can initiate and maintain tumors, but the function of non-cancer stem cells that form the tumor bulk remains poorly understood. Proteomic analysis showed a higher abundance of the extracellular matrix small leucine-rich proteoglycan Fibromodulin (FMOD) in the conditioned medium of non-cancer stem cells (DGCs; differentiated glioma cells) of glioma compared to that of glioma stem-like cells (GSCs). DGCs silenced for FMOD fail to cooperate with co-implanted GSCs to promote tumor growth. FMOD downregulation neither affects GSC growth and differentiation nor DGC growth and reprogramming *in vitro*. DGC-secreted FMOD promotes angiogenesis by activating Integrin-dependent Notch signaling in endothelial cells. Furthermore, conditional silencing of FMOD in newly generated DGCs *in vivo* inhibits the growth of GSC-initiated tumors due to poorly developed vasculature and increases mouse survival. Collectively, these findings demonstrate that DGC-secreted FMOD promotes glioma tumor angiogenesis and growth through paracrine signaling in endothelial cells and identifies a DGC-produced protein as a potential therapeutic target in glioma.

bioRxiv preprint doi: https://doi.org/10.1101/2022.04.03.486893; this version posted April 6, 2022. The copyright holder for this preprint (which was not certified by peer review) is the author/funder, who has granted bioRxiv a license to display the preprint in perpetuity. It is made available under aCC-BY 4.0 International license.

Introduction

Tumors and their microenvironment form an ecosystem with many cell types that support tumor growth. The key constituents of this ecosystem include cancer stem-like cells (CSCs), non-cancer stem cells (non-CSCs) or differentiated cancer cells, and various other cell types that collectively make up the tumor stroma ***(Prager et al., 2019)***. It is well established that the tumor-initiating capacity lies solely with CSCs, thereby making them the crucial architects of tumor-stroma interactions that favor tumor growth and progression ***(Rheinbay et al., 2013)***. CSCs have a dichotomous division pattern, as they are capable of self-renewal and give rise to differentiated cells that form the bulk of the tumor ***(Olmeda and Ben Amar, 2019).*** The indispensable role of CSCs, which usually constitute only a minority population within tumors, is well documented in many solid tumors ***(Galli et al., 2004; Ignatova et al., 2002; Singh et al., 2004; Yang et al., 2020a).***

The tumor microenvironment is a vital driver of plasticity and heterogeneity in cancer ***(Carnero and Lleonart, 2016; Heddleston et al., 2010)***. The presence of hypoxic and necrotic regions is the hallmark of very aggressive tumors like glioblastoma (GBM), which have a highly vascular niche that supplies nutrients to cancer cells and makes a conducive environment for the tumor cells to thrive ***(Hambardzumyan and Bergers, 2015; Huang et al., 2016).*** Paracrine signaling mediated by proteins secreted from tumor cells, particularly glioma stem-like cells (GSCs), helps acquire this highly vascular phenotype by attracting blood vessels towards themselves and inducing pro-angiogenic signaling in endothelial cells through extracellular matrix remodeling ***(Dittmer and Leyh, 2014; Rupp et al., 2016).*** A reciprocal relationship exists between GSCs and endothelial cells by which endothelial cells induce stemness phenotype in cancer cells through activation of Notch, Sonic-Hedgehog, and Nitric Oxide Synthase signaling pathways ***(Jeon et al., 2014; Zhu et al., 2011)***, while GSCs drive vascularization of the tumor via endogenous endothelial cell stimulation, vascular mimicry, and GBM-endothelial cell transdifferentiation ***(Hardee and Zagzag, 2012; Soda et al., 2011)***. Recent reports have shown that CSCs induce such a high vascularization of tumors such as GBM by migrating along blood vessel scaffolds to invade novel vascular niches, thereby ensuring surplus and continuous blood supply at their disposal ***(Prager et al., 2020)***. In GBM, CD133+ and Nestin+ cells (representing GSCs) are located in close proximity of the tumor microvascular density (MVD), whereas a lower number of CD133- and Nestin- cells (representing differentiated glioma cells; DGCs) are located

bioRxiv preprint doi: https://doi.org/10.1101/2022.04.03.486893; this version posted April 6, 2022. The copyright holder for this preprint (which was not certified by peer review) is the author/funder, who has granted bioRxiv a license to display the preprint in perpetuity. It is made available under aCC-BY 4.0 International license.

in the vicinity of the blood vessels. It has also been reported that the depletion of brain tumor blood vessels causes a decrease in the number of tumor-initiating GSCs ***(Calabrese et al., 2007).***

Besides CSC self-renewal, their differentiation to form the bulk cancer cells also plays a crucial role in tumor growth and maintenance ***(Jin et al., 2017).*** Epigenome unique to CSCs compared to differentiated cancer cells has been documented ***(Suva et al., 2014; Zhou et al., 2018).*** Reciprocally, a set of four reprogramming transcription factors, POU3F2, SOX2, SALL2, and OLIG2, is identified in GBM that are sufficient to reprogram DGCs and create the epigenetic landscape of native GSCs, thus creating "induced" cancer stem cells (***Suva et al., 2014***). The epigenetic regulation forms the basis of cellular plasticity, which creates a dynamic equilibrium between CSCs and differentiated cancer cells ***(Safa et al., 2015).*** Oncogene-induced dedifferentiation of mature cells in the brain was also reported using a mouse model of glioma, and the reprogrammed CSCs were proposed to contribute to the heterogeneous cell state populations observed in malignant gliomas ***(Friedmann-Morvinski et al., 2012; Friedmann-Morvinski and Verma, 2014***). Lineage tracing analyses revealed the reprogramming of DGCs to GSCs that act as a reservoir for initiating relapse of the tumors upon Temozolomide chemotherapy ***(Auffinger et al., 2014).*** Hypoxia has also been reported to reprogram differentiated cells to form CSCs in glioma, hepatoma, and lung cancer (***Prasad et al., 2017; Wang et al., 2017)***. Spontaneous conversion of differentiated cancer cells to CSCs has also been reported in breast cancer ***(Klevebring et al., 2014).***

Collectively, these studies highlight the crucial role of CSCs in cellular cross-talk in the tumor niche and establish CSCs as critical drivers of tumorigenesis. However, the massive imbalance in the proportions of CSCs and non-CSCs or differentiated cancer cells in tumors raises several important questions. Considering that differentiated cancer cells constitute the bulk of tumors, do they have specific functions, or do they only constitute the tumor mass? Do they contribute to the complex paracrine signaling occurring within the tumor microenvironment? Do they support tumor growth by promoting CSC growth and maintenance? It has been recently shown in GBM that DGCs cooperate with GSCs through a paracrine feedback loop involving neurotrophin signaling to promote tumor growth ***(Wang et al., 2018).*** While this study suggests a supporting role for differentiated cancer cells in tumor growth, the large proportion of them in tumors suggests a role in paracrine interactions with other stromal cells in the tumor niche.

bioRxiv preprint doi: https://doi.org/10.1101/2022.04.03.486893; this version posted April 6, 2022. The copyright holder for this preprint (which was not certified by peer review) is the author/funder, who has granted bioRxiv a license to display the preprint in perpetuity. It is made available under aCC-BY 4.0 International license.

We used quantitative proteomics to identify DGC-secreted proteins that might support their paracrine interactions within the tumor microenvironment. We show an essential role of Fibromodulin (FMOD) secreted by DGCs in promoting tumor angiogenesis via a cross-talk with endothelial cells. FMOD promotes Integrin-dependent Notch signaling in endothelial cells to enhance their migratory and blood vessel forming capacity. These findings indicate that DGCs are crucial for supporting tumor growth in the complex tumor microenvironment by promoting multi-faceted interactions between tumor cells and the stroma.

Results

DGC and GSC secretomes have distinct proteomes revealed by tandem mass spectrometry

While GSCs alone can initiate a tumor, the overall tumor growth requires functional interactions between GSCs and DGCs ***(Singh et al., 2004; Wang et al., 2018)***. To further understand the respective roles of GSCs vs. DGCs in tumor growth, we compared the conditioned medium (CM) derived from three patient-derived human GSC cell lines (MGG4, MGG6, and MGG8) ***(Wakimoto et al., 2009)*** and their corresponding DGCs, using a quantitative proteomic strategy. Proteins in CMs were systematically analyzed by nano-flow liquid chromatography coupled to Fourier transform tandem mass spectrometry (nano-LC-FT-MS/MS), and their relative abundance in DGC vs. GSC CM was determined by label-free quantification. We found that 119 proteins are more abundant in GSC CM, while 185 proteins are more abundant in the DGC CM ($p<0.05$, **Figure 1A; Supplementary Table S1**). Analysis of overrepresented functional categories among proteins exhibiting differential abundances in GSC vs. DGC CMs using Perseus with a p< value 0.05 revealed that the DGC CM is enriched in proteins known to exhibit extracellular or cell surface localization, such as proteins annotated as extracellular matrix (ECM) organization while terms related to DNA replication and many signaling pathways are enriched in GSC CM (**Supplementary Figures 1A and B**).

TGFβ signaling controls the expression of Fibromodulin (FMOD) in DGCs

The enrichment of the "extracellular matrix" (ECM) annotation among proteins exhibiting higher abundance in DGC secretome prompted us to focus on ECM proteoglycans in line with their critical role in facilitating cancer cell signaling through their interaction with growth factor receptors, extracellular ligands and matrix components, and in promoting tumor-microenvironment interactions ***(Winkler et al., 2020)***. Six ECM proteoglycans were found to be

bioRxiv preprint doi: https://doi.org/10.1101/2022.04.03.486893; this version posted April 6, 2022. The copyright holder for this preprint (which was not certified by peer review) is the author/funder, who has granted bioRxiv a license to display the preprint in perpetuity. It is made available under aCC-BY 4.0 International license.

more abundant in DGC CM compared with GSC CM (**Figure 1B**). The role of five of them (LAMB2, SERPINEE1, ITGB1, TNC, and LAMA5) in tumor growth has been well established ***(Angel et al., 2020; Bartolini et al., 2016; Long et al., 2016; Wang et al., 2021; Yang et al., 2020b).*** We thus focused on FMOD that exhibited the highest DGC CM/GSC CM protein ratio. FMOD is a small leucine-rich repeat proteoglycan upregulated in GBM due to the loss of promoter methylation orchestrated by TGFβ1-dependent epigenetic regulation ***(Mondal et al., 2017).*** FMOD promotes glioma cell migration through actin cytoskeleton remodeling mediated by an Integrin-FAK-Src-Rho-ROCK signaling pathway but does not affect colony-forming ability, growth on soft agar, chemosensitivity, and glioma cell proliferation ***(Mondal et al., 2017).*** We first confirmed the higher abundance of FMOD seen in DGC CM compared to GSC CM (**Figure 1C**) both at the transcript level (**Figure 1D)** and at the protein level (**Figures 1E and F**) in three GSC cell lines (MGG4, MGG6, and MGG8).

In line with our previous findings indicating that TGFβ signaling controls FMOD expression in glioma ***(Mondal et al., 2017),*** we next explored the possible role of this pathway in FMOD overexpression in DGCs. Gene Set Enrichment Analysis (GSEA) analysis of differentially regulated transcripts in GSC vs. DGC showed significant depletion of several TGFβ signaling pathway genes (**Supplementary Figure 2; Supplementary Table S2),** suggesting an enhanced TGFβ signaling in DGCs. Likewise, GSEA revealed an enrichment of several TGFβ signaling pathway genes in most GBM transcriptome datasets (**Supplementary Figure 3),** further supporting activation of TGFβ signaling in DGCs that represent the bulk of GBMs. In addition, the DGCs used in this study that express a high level of FMOD showed enrichment in mesenchymal signature, compared to GSCs (**Supplementary Figure 4**), consistent with the elevated TGF TGFβ signaling and FMOD levels we observed in the mesenchymal GBM subtype (**Supplementary Figures 5A and B**). Moreover, treating MGG8-DGCs with the TGFβ inhibitor (SB431542) significantly decreased luciferase activity of SBE–Luc (a TGFβ responsive reporter and contains Smad binding elements) and FMOD Promoter-Luc reporters (**Supplementary Figures 5C and D**). We also found higher levels of FMOD and TGM2 (a bonafide TGFβ target gene) transcripts and FMOD and pSMAD2 (an indicator of activated TGFβ signaling) proteins in MGG8-DGCs than MGG8-GSCs (**Figures 1G to 1I**). The addition of a TGFβ inhibitor (SB431542) significantly decreased transcript levels of FMOD and TGM2, and protein levels of FMOD and pSMAD2 in MGG8-DGCs (**Figures 1G to 1I**). Further, chromatin

bioRxiv preprint doi: https://doi.org/10.1101/2022.04.03.486893; this version posted April 6, 2022. The copyright holder for this preprint (which was not certified by peer review) is the author/funder, who has granted bioRxiv a license to display the preprint in perpetuity. It is made available under aCC-BY 4.0 International license.

immunoprecipitation experiments revealed pSMAD2 occupancy on FMOD promoter in MGG8 DGCs that was significantly reduced by pretreating cells with SB431542 (**Figure 1J**). These results demonstrate a predominant expression and secretion of FMOD by DGCs that are promoted by TGFβ signaling.

Tumor growth requires FMOD secreted by DGCs

We next investigated the role of FMOD in GSC and DGC growth and interconversion between both cell populations *in vitro* using two human (MGG8 and U251) and two murine (AGR53 and DBT-Luc) glioma cell lines. We found that the absence of FMOD neither affected GSC growth and differentiation to DGC (**Supplementary Figures 6 to 8**) nor DGC growth and reprogramming to form GSCs (**Supplementary Figures 9 to 11**; more details in **Supplementary information**), consistent with our previous findings showing that FMOD does not affect glioma cell proliferation *in vitro* ***(Mondal et al., 2017).*** In line with previous findings that DGCs cooperate with GSCs to promote tumor growth ***(Wang et al., 2018),*** we then evaluated the ability of DGCs silenced for FMOD to support the growth of tumors initiated by GSCs in co-implantation experiments in a syngeneic mouse model using GSCs and DGCs derived from DBT-Luc glioma cells. Reminiscent of our observations in MGG8 cell line, DBT-Luc-DGCs express higher levels of FMOD than DBT-Luc-GSCs (**Supplementary Figures 10C and D**). To silence the expression of FMOD in DBT-Luc-DGCs, we used a doxycycline-inducible construct that contains an inducible mCherry-shRNA downstream of the Tet-responsive element ***(Angel et al., 2020)*** (**Figure 2A**). The scheme of the co-implantation experiment is described on **Figure 2B**. DBT-Luc-GSC cells were coinjected with either DBT-Luc-DGC/miRNT (non-targeting shRNA) or DBT-Luc-DGC/miRFMOD (FMOD shRNA). In both groups, 50% of the mice received doxycycline on alternated days from day nine post-injection until the end of the experiment. Tumors in mice coinjected with DBT-Luc-GSCs and DBT-Luc-DGCs/miRNT grew much faster and reached a significantly larger size (measured by bioluminescence) than tumors in mice injected with DBT-Luc-GSCs alone, regardless of doxycycline treatment (**Figures 2B to 2D, compare black and purple lines with blue line; Supplementary Table S3**). Notably, mice treated with doxycycline did show mCherry expression in tumors (**Figure 2C**). In contrast, injected DBT-Luc-DGC/miRFMOD cells failed to support the growth of tumors initiated by DBT-Luc-GSCs in doxycycline-treated mice compared to doxycycline untreated mice (**Figures 2B to 2D; compare red line with orange line; Supplementary Table S3)**. While mice injected with DBT-Luc-GSCs

bioRxiv preprint doi: https://doi.org/10.1101/2022.04.03.486893; this version posted April 6, 2022. The copyright holder for this preprint (which was not certified by peer review) is the author/funder, who has granted bioRxiv a license to display the preprint in perpetuity. It is made available under aCC-BY 4.0 International license.

+ DBT-Luc-DGCs/miRFMOD (Dox+) showed an increase in tumor growth until the onset of doxycycline treatment (as seen in the rise in bioluminescence), subsequent tumor growth was drastically reduced. As expected, mice injected with DBT-Luc-DGCs alone developed substantially small tumors (**Figures 2C and D**). The small tumors formed in animals injected with either DBT-Luc-GSC + DBT-Luc-DGC/miRFMOD (Dox+) or DBT-Luc-GSC alone expressed significantly less FMOD protein than other tumors (**Supplementary Figure 12**). These results indicate that FMOD secreted by DGCs is essential for the growth of tumors initiated by GSCs.

FMOD induces angiogenesis of host-derived and tumor-derived endothelial cells

Tumor cell interactions with stromal cells are critical for glioma tumor growth ***(Pine et al., 2020).*** Small leucine-rich proteoglycans such as FMOD promote angiogenesis in the context of cutaneous wound healing ***(Pang et al., 2019)***. In addition, we previously found a significant enrichment of the term "Angiogenesis" among differentially regulated genes in FMOD-silenced U251 glioma cells (***Mondal et al., 2017***). In light of these observations, we next examined the impact of FMOD on tumor angiogenesis. First, we tested the ability of glioma cell-derived FMOD to induce angiogenic network formation by immortalized human pulmonary microvascular endothelial cells (ST1). We used LN229 and U251 glioma cells, which express low and high levels of FMOD, respectively, for overexpression and silencing studies ***(Mondal et al., 2017)***. We found that the CM derived from LN229 cells stably expressing FMOD (LN229/FMOD) induced more angiogenesis than LN229/Vector stable cells (**Figures 3A and B**). Further, the CM of FMOD-silenced U251 cells was less efficient in promoting angiogenesis than the CM of cells expressing non-targeting siRNA (**Figure 3C; Supplementary Figure 13A)** or shRNA (**Supplementary Figure 13B**). The addition of recombinant human FMOD (rhFMOD) to the CM of U251/siFMOD cells rescued its ability to induce angiogenesis (**Figure 3C; Supplementary Figure 13A**). More importantly, the addition of rhFMOD directly to endothelial cells induced angiogenesis in the presence of a control antibody (IgG) but not in the presence of an FMOD neutralizing antibody (**Supplementary Figure 13C**).

Both CMs derived from three DGCs and their corresponding GSCs also induced angiogenesis efficiently (**Supplementary Figure 13D**). Further, pretreating cells with an FMOD antibody significantly reduced the ability of MGG8-DGC CM, but not that of MGG8-GSC CM, to induce angiogenesis (**Figure 3D**). The reduced ability of the FMOD antibody-pretreated DGC CM to promote angiogenesis was rescued by the exogenous addition of an excess of rhFMOD

bioRxiv preprint doi: https://doi.org/10.1101/2022.04.03.486893; this version posted April 6, 2022. The copyright holder for this preprint (which was not certified by peer review) is the author/funder, who has granted bioRxiv a license to display the preprint in perpetuity. It is made available under aCC-BY 4.0 International license.

(**Figure 3D**). Moreover, CM derived from FMOD-silenced MGG8-DGCs was less efficient in promoting angiogenesis than the CM of shNT (**Figure 3D**) or siNT (**Supplementary Figure 13E)** transfected MGG-DGC cells. The effect of FMOd silencing was rescued by adding exogenous rhFMOD (**Figure 3D; Supplementary Figure 13E**). Both rhFMOD and FMOD present in the CM collected from MGG8-DGC induced the migration and invasion but not the proliferation of ST1 cells (**Supplementary Figures 14A to 14E).** Further, CM from MGG8-DGC/shNT cells was more efficient than CM from MGG8-DGC/shFMOD cells to promote angiogenic network formation by human brain-derived primary endothelial cells (HBMECs) and mouse brain-derived immortalized endothelial cells (B.End3) (**Figures 3E and F; Supplementary Figure 14F**). Again, the effect of FMOD silencing was rescued by adding rhFMOD (**Figures 3 E and F**; **Supplementary Figure 14F).**

Vascular mimicry (VM) is one of the alternative mechanisms of angiogenesis wherein tumor-derived endothelial cells (TDECs) originate from glioblastoma cells ***(Angara et al., 2017; Ricci-Vitiani et al., 2010; Soda et al., 2011).*** To assess the ability of FMOD to induce TDECs derived from DGCs to form angiogenic networks, we used MGG8-DGC and U87 cells. MGG8-DGC/shNT cells grown in endothelial media (M199) under hypoxia (1% O_2) differentiated to TDECS as evidenced by an increase in CD31 (**Figures 3 G and H**). MGG8-DGC/shFMOD also differentiated to form TDECs, albeit with less efficiency (**Figures 3G and H**). Further, the addition of rhFMOD induced both MGG8-DGC/shNT-TDEC and MGG8-DGC/shFMOD-TDEC cells to form angiogenic networks efficiently (**Figures 3 I and J**). Similarly, U87 cells differentiated to TDECs (**Supplementary Figures 15A and B),** which readily formed angiogenic networks in the presence of rhFMOD **(Supplementary Figures 15 C and D).** Collectively, these results demonstrate that DGC CM can induce angiogenesis and identify FMOD as a critical mediator of DGC-induced angiogenesis.

FMOD activates Integrin/FAK/Src-dependent Notch pathway in endothelial cells to induce angiogenesis

To dissect the signaling mechanisms underlying FMOD-induced angiogenesis, we subjected protein extracts derived from ST1 endothelial cells treated or not with rhFMOD to Reverse Phase Protein Array (RPPA). A total of 12 proteins exhibited differential abundance in a time-dependent manner in rhFMOD-treated ST1 endothelial cells (**Figure 4A**). These include HES1, a downstream target of the Notch signaling pathway that has been shown to promote

bioRxiv preprint doi: https://doi.org/10.1101/2022.04.03.486893; this version posted April 6, 2022. The copyright holder for this preprint (which was not certified by peer review) is the author/funder, who has granted bioRxiv a license to display the preprint in perpetuity. It is made available under aCC-BY 4.0 International license.

angiogenesis (***Zhao et al., 2017***). We thus investigated the possible involvement of Notch signaling in FMOD-induced angiogenesis. The addition of rhFMOD induced luciferase activity of Notch-dependent CSL-Luc and HES-Luc reporters in ST1 cells, but not in γ-secretase inhibitor-(GSI; a Notch pathway inhibitor) pretreated cells (**Supplementary Figures 16A and B**). The addition of rhFMOD also increased HES1 mRNA and protein levels in ST1 cells, an effect abolished by GSI pretreatment of cells **(Figures 4B and C).** rhFMOD treatment also resulted in the translocation of NICD (Notch intracellular domain) from the cytosol to the nucleus, as shown by subcellular fractionation and confocal microscopy **(Supplementary Figures 16C and D**). Furthermore, rhFMOD failed to induce angiogenic network formation by GSI-pretreated ST1 cells (**Figure 4D**). In addition, ST1 cells having a stable expression of NICD (ST1/NICD) showed enhanced angiogenic network formation than ST1 vector stable (ST1/Vector) cells (**Supplementary Figures 17A to 17D).** FMOD present in CM from MGG8-DGCs induced ST1/Vector cells, but not ST1/NICD cells to form more angiogenic networks, suggesting that Notch activation in endothelial cells is an essential step in FMOD-induced angiogenesis.

The increase in phosphorylated FAK (pFAK, FAK_Py397-R-V; the molecule downstream of Integrin signaling) levels in rhFMOD-treated endothelial cells, as shown by RPPA (**Figure 4A**), also suggested a possible role of integrin signaling in FMOD-induced angiogenesis. This is consistent with our previous findings indicating that FMOD activates Integrin signaling *via* type I collagen to engage the FAK-Src-Rho-ROCK pathway and promote the migration of glioma cells ***(Mondal et al., 2017).*** We first confirmed the activation of Integrin signaling by FMOD, as assessed by increased pFAK in rhFMOD-treated ST1cells, but not in cells pretreated with RGD peptide, an Integrin inhibitor (**Figure 4E**). The addition of RGD peptide inhibited angiogenesis induced by LN229/FMOD CM (**Figure 4F**). Likewise, angiogenesis induced by LN229/FMOD CM was completely inhibited when ST1 cells were pretreated with inhibitors of FAK (FAKi) or Src (PP2), two signaling molecules downstream of Integrin (**Figure 4F**). These treatments also strongly reduced the basal level of angiogenesis elicited by the CM of LN229/Vector cells. In contrast, an inactive analog of Src inhibitor (PP3), as well as inhibitors of RAC1 and ROCK, failed to inhibit the ability of CM derived from LN229/FMOD cells to induce angiogenesis (**Figure 4F**). Our previous report also demonstrated that the interaction of FMOD with type I collagen is essential for integrin activation ***(Mondal et al., 2017).*** The C-terminal region of FMOD comprises 11 leucine-rich-repeats (LRRs), of which the 11th repeat binds to type I collagen ***(Oldberg et al.,***

bioRxiv preprint doi: https://doi.org/10.1101/2022.04.03.486893; this version posted April 6, 2022. The copyright holder for this preprint (which was not certified by peer review) is the author/funder, who has granted bioRxiv a license to display the preprint in perpetuity. It is made available under aCC-BY 4.0 International license.

2007). A synthetic interfering peptide (**RLDGN*EIK*R**) corresponding to the 11th LRR of type 1 collagen, but not a modified peptide (**RLDGNQI*M*R**), competes with rhFMOD for binding to type I collagen to activate integrin signaling in glioma cells ***(Mondal et al., 2017; Oldberg et al., 2007).*** Consistent with these findings, rhFMOD-induced luciferase activity of CSL-Luc and HES-Luc (**Supplementary Figures 18A and B**) and angiogenesis by ST1 cells (**Supplementary Figure 18C**) were significantly inhibited by the interfering peptide, but not the modified peptide, suggesting a crucial role of type I collagen-dependent activation of Integrin signaling in FMOD-induced angiogenesis. To identify the α and β subunits of integrin involved in FMOD-mediated activation of integrin signaling in endothelial cells, we chose ITGA6, ITGB1, and ITGAV for investigation based on analysis of transcriptome data derived from laser capture dissected microvessels from the human brain (more detail in **Supplementary information**). Silencing either of the selected three integrin subunits in ST1 cells reduced significantly the ability of rhFMOD to activate integrin as assessed by reduced pFAK levels (**Supplementary Figures 18B to 18I**), thus demonstrating the involvement of αv/β1 and α6/β1 heterodimeric integrin receptors in FMOD activation of integrin signaling in endothelial cells.

Next, to examine a possible cross-talk between Integrin and Notch signaling in FMOD-treated endothelial cells, we tested the effect of the RGD peptide on the ability of rhFMOD to induce Notch signaling. Pretreatment of ST1 cells with RGD peptide significantly reduced rhFMOD-elicited CSL-Luc and HES-Luc activation (Supplementary **Figures 4E and F**). Likewise, pretreatment of cells with FAKi or PP2, but not PP3, significantly reduced rhFMOD-induced CSL-Luc and HES-Luc activity in ST1 cells **(Supplementary Figures 19A to 19D).** Further, rhFMOD failed to increase HES1 transcript and protein levels in ST1 cells treated with either RGD peptide, FAKi, or PP2, but not in cells treated with PP3 **(Figures 4G and H; Supplementary Figures 19E to 19H)**.

We next investigated the mechanistic link between Integrin and Notch signaling in FMOD-treated ST1 cells. Since Notch activation by FMOD is sensitive to GSI treatment, we explored activation of Notch ligands by Integrin-FAK signaling in FMOD-treated cells. While the addition of rhFMOD induced DLL3 and JAG1 transcripts in ST1 cells, RGD peptide pretreatment abolished JAG1 induction (**Supplementary Figure 20A**), suggesting that JAG1 might be a potential linking molecule. Consistently, pretreatment of cells with either FAKi or PP2, but not PP3, also abolished the ability of rhFMOD to induce JAG1 transcript in ST1 cells (**Supplementary**

bioRxiv preprint doi: https://doi.org/10.1101/2022.04.03.486893; this version posted April 6, 2022. The copyright holder for this preprint (which was not certified by peer review) is the author/funder, who has granted bioRxiv a license to display the preprint in perpetuity. It is made available under aCC-BY 4.0 International license.

Figures 20B and C). Further, JAG1 silencing significantly decreased rhFMOD-induced activity of CSL-Luc and HES-Luc reporters and HES1 transcript/protein levels in ST1 cells (**Supplementary Figures 20D and E; Figures 4I to 4K**). JAG1 silencing also abolished the ability of rhFMOD to induce angiogenic networks by ST1 cells (**Figure 4L**). In addition, rhFMOD induced expression of the FAK inducible transcription factor KLF8 mRNA in ST1 cells, an effect abolished by pretreating cells with RGD peptide (**Supplementary Figure 20F)**. Further, KLF8 silencing in ST1 cells significantly reduced the ability of rhFMOD to increase pFAK level (**Supplementary Figures 20G and H**), suggesting that KLF8 activates JAG1 through an integrin-dependent pathway in FMOD-treated endothelial cells. Collectively, these results identify JAG1 as a molecular link between Integrin and Notch signaling pathways in FMOD-treated endothelial cells and demonstrate a key role of Integrin-FAK-JAG1-Notch-HES1 signaling in FMOD-induced angiogenesis.

To further explore the clinical relevance of these findings, we interrogated transcriptome datasets from multiple sources (more detail in **Supplementary Information**). We found a significant upregulation of transcript levels of FMOD, JAG1 and HES1 in GBM from various datasets (**Supplementary Figures 21A to 21C).** We also found a positive correlation between FMOD and HES1 transcripts and between FMOD and JAG1 transcripts in the majority of GBM datasets analyzed (**Supplementary Figures 21D and E)**, which further substantiates the functional link between FMOD, JAG1, and HES1. We also show that high FMOD transcript levels and hypomethylation of FMOD promoter are associated with poor prognosis in most datasets (**Supplementary Figures 22F and G)**. These observations provide additional support for the activation of Integrin-Notch signaling in FMOD-treated endothelial cells.

DGC-secreted FMOD is required for the growth of murine and human GSC-initiated tumors

While GSCs alone can initiate a tumor, tumor growth requires continuous differentiation to form DGCs, which form the bulk of the tumor mass. In line with our co-implantation experiments (**Figure 2**), we sought to define the importance of FMOD secreted by DGCs generated through a differentiation program initiated by GSCs during tumor growth *in vivo*, using a syngenic intracranial glioma mouse model. We injected AGR53-GSC-miRNT and AGR53-GSC-miRFMOD cells intracranially into C57/black mice and allowed them to form tumors. Thirteen days after intracranial injections, both groups received doxycycline as indicated (**Figure 5A**). The understanding is that as the tumors start growing, GSCs, in addition to their self-renewal, will start

bioRxiv preprint doi: https://doi.org/10.1101/2022.04.03.486893; this version posted April 6, 2022. The copyright holder for this preprint (which was not certified by peer review) is the author/funder, who has granted bioRxiv a license to display the preprint in perpetuity. It is made available under aCC-BY 4.0 International license.

differentiating *de novo* to form DGCs, which would express high levels of FMOD. However, doxycycline treatment would inhibit FMOD expression, and thus one could investigate the importance of DGC-secreted FMOD in tumor growth. AGR53-GSC/miRNT and AGR53-GSC/miRFMOD cell-initiated tumors showed a similar size seven days after doxycycline treatment as shown by mCherry fluorescence (**Figures 5B and C; day 21)**. However, upon subsequent follow-up, doxycycline administration significantly inhibited the growth of AGR53-GSC/miRFMOD-initiated tumors over time but not that of AGR53-GSC/miRNT tumors (**Figures 5B, C, and E**). Further, doxycycline administration increased the survival of mice injected with AGR53-GSC/miRFMOD cells compared to AGR53-GSC/miRNT cells (**Figure 5D**). AGR53-GSC/miRFMOD initiated tumors showed decreased FMOD, mCherry, and GFP expression compared to AGR53-GSC/miRNT initiated tumors (**Figures 5F and G**). DBT-Luc GSC/miRFMOD, another murine glioma GSC cell line, produced similar results: FMOD silencing after doxycycline administration resulted in reduced tumor growth (**Supplementary Figures 23A and B**), increased mice survival (**Supplementary Figures 23C**), and decreased FMOD expression (**Supplementary Figure 23D**).

To determine the relevance of our findings for the human pathology, we investigated the importance of DGC-secreted FMOD in the growth of tumors initiated by MGG8 and U251 cells using a xenograft mouse glioma model. The enrichment of cancer stem cells in MGG8 GSC neurospheres was confirmed by the higher expression of CD133, compared to MGG8 DGCs (**Figure 6A**). We established orthotopic xenografts using MGG8-GSC/shNT and MGG8-GSC/shFMOD cells. Reminiscent of results obtained using transplantation of murine glioma cells, MGG8-GSC/shNT-transplanted mice readily developed intracranial tumors, whereas MGG8-GSC/shFMOD mice showed impaired tumor formation and increased mice survival (**Figures 6B, and C**). Immunostaining and confocal microscopy analysis showed high expression of FMOD in MGG8-GSC/shNT while FMOD was barely detectable in MGG8-GSC/shFMOD tumors (**Figure 6D**). Likewise, U251/shFMOD cells that showed reduced FMOD protein level compared to U251/shNT (**Supplementary Figure 11A)**, developed smaller tumors (**Figures 6E to 6H**), and mice bearing U251/shFMOD tumors had longer survival than those carrying U251/shNT tumors (**Figure 6G)**. As expected, the expression of FMOD was more elevated in U251/shNT tumors than in U251/shFMOD tumors (**Figure 6I**). Collectively, these findings indicate that DGC-secreted FMOD is essential for the growth of both human and mouse glioma.

bioRxiv preprint doi: https://doi.org/10.1101/2022.04.03.486893; this version posted April 6, 2022. The copyright holder for this preprint (which was not certified by peer review) is the author/funder, who has granted bioRxiv a license to display the preprint in perpetuity. It is made available under aCC-BY 4.0 International license.

Reduced angiogenesis in small tumors formed in FMOD-silenced conditions

Next, we investigated the mechanism underlying reduced tumor growth in FMOD-silenced conditions. First, we measured the expression of CD133 and GFAP markers as the representation of GSCs and DGCs in the tumors formed in the animal models. The CD133 positive cells are much less in proportion compared to GFAP positive cells in tumors formed by AGR53-GSC, DBT-Luc-GSCs, and MGG8-GSCs under FMOD non-targeting conditions (**Supplementary Figures 24A, and B, 25A and B, and 26A and B**), in good correlation to the low proportion of GSCs seen in brain tumors (**Singh et al., 2004, Galli et al., 2004, and Calabrese et al., 2007**). Further, most GFAP positive cells are also positive for FMOD expression compared to CD133 positive cells (**Supplementary Figures 24A and C, 25A and C, and 26A and C**), recapitulating the results we obtained *in vitro*, where FMOD is expressed specifically by DGCs (**Figure 1**). We also found a similar expression pattern of CD133 and GFAP markers in small tumors formed under FMOD-silenced conditions in all three tumor models (**Supplementary Figures 24D and E, 25D and E, and 26D and E).** The GFAP staining in these tumors confirms the occurrence of an efficient differentiation program even in FMOD-silenced conditions, which confirms our results obtained *in vitro*, where the absence of FMOD failed to affect the GSC differentiation to form DGCs **(Supplementary Figures 6 and 8)**. As expected, the small tumors formed in FMOD-silenced conditions showed substantially reduced FMOD staining (**Supplementary Figures 24D and F, 25D and F, and 26D and F).**

We next evaluated the extent of blood vessel formation by measuring the endothelial cell marker immunostaining in the tumors. The small size tumors formed by AGR53-GSC/miRFMOD cells after doxycycline treatment showed reduced staining for CD31 and vWF (von Willebrand factor) compared to AGR53-GSC/miRNT tumors (**Figures 7A to 7C, and Supplementary Figures 27A to 27C**). Tumors formed by DBT-Luc-GSC/miRFMOD cells in doxycycline-treated mice also showed significantly reduced CD31 staining compared to that measured in the absence of doxycycline treatment (**Supplementary Figures 27D to 27F**). Reminiscent of murine glioma tumors, tumors induced by MGG8-GSC/shFMOD cells also showed reduced CD31 staining compared to MGG8-GSC/shNT cells (**Figures 7D to 7F**). We then tested the extent of blood vessel formation by TDECs. In all three tumor models (AGR53-GSCs, DBT-Luc-GSCs, and MGG8-GSCs), blood vessels formed by TDECs were significantly reduced in tumors formed in FMOD-silenced conditions (**Figures 7G to 7L; Supplementary Figures 27G to 27I**). These findings

bioRxiv preprint doi: https://doi.org/10.1101/2022.04.03.486893; this version posted April 6, 2022. The copyright holder for this preprint (which was not certified by peer review) is the author/funder, who has granted bioRxiv a license to display the preprint in perpetuity. It is made available under aCC-BY 4.0 International license.

confirm our previous results obtained *in vitro*, where the absence of FMOD decreased the ability of host-derived endothelial cells and TDECs to form angiogenic networks (**Figure 3; Supplementary Figures 13 to 15**). Next, we investigated the involvement of Integrin-FAK-JAG1-Notch-HES1 signaling in FMOD-induced angiogenesis in the context of glioma tumors. Confocal microscopy analysis in tumors formed by MGG8-GSCs, AGR53-GSCs, and DBT-Luc-GSCs revealed a significant colocalization of the endothelial cell marker CD31 with FMOD, pFAK, JAG1, and HES1 in blood vessels (**Supplementary Figures 28A to 28C**). From these results, we conclude that angiogenesis induced by DGC-secreted FMOD is essential for glioma tumor growth.

Discussion

Cellular hierarchy is well established in GBM. The importance of GSCs in tumor initiation, growth, immune escape, angiogenesis, invasion into the normal brain and resistance to therapy is also well established ***(Bao et al., 2006; Wakimoto et al., 2009)***. GSCs are known for their ability to self-renew and to differentiate to form DGCs, the bulk cells of tumors (***Galli et al., 2004; Ignatova et al., 2002; Singh et al., 2004; Suva et al., 2014; Yang et al., 2020a***). However, the role of DGCs in tumor growth remains poorly understood. The key requirement of tumor cells for self-maintenance in a novel tumor niche is the supply of nutrients. GSCs are known to promote the establishment of a highly vascularized microenvironment by being in close physical contact with endothelial cells ***(Calabrese et al., 2007)***. The massive proportion of DGCs in the tumor suggests that GSC-initiated angiogenesis might not be sufficient to meet the large nutrient requirement of the entire tumor. Wang *et al.* demonstrated that DGC-secreted BDNF is essential for GSC growth and maintenance through DGC-GSC paracrine signaling, which highlights the crucial role of DGC- secreted proteins in tumor formation (***Wang et al., 2018***). Further, a possible interaction between DGCs and stromal cells, such as endothelial cells, cannot be ruled out. We hypothesized that in addition to GSCs, DGCs might play an essential role in autocrine and paracrine signaling involving different types of cells to augment tumor growth. The present study demonstrates the existence of paracrine signaling between DGCs and endothelial cells, which promotes angiogenesis and glioma tumor growth.

Previously, we have demonstrated that FMOD is highly expressed in GBMs compared to normal brain tissues. The loss of FMOD expression hampers the migratory function of glioma

bioRxiv preprint doi: https://doi.org/10.1101/2022.04.03.486893; this version posted April 6, 2022. The copyright holder for this preprint (which was not certified by peer review) is the author/funder, who has granted bioRxiv a license to display the preprint in perpetuity. It is made available under aCC-BY 4.0 International license.

cells but has no impact on glioma cell proliferation ***(Mondal et al., 2017).*** This study identifies that FMOD is expressed exclusively by DGCs and further showed that FMOD is not needed for GSC/DGC growth and their plasticity to form one from the other. Given these facts, the inability of DGCs silenced for FMOD to support the growth of tumors initiated by GSCs was unexpected. However, it enlightened us that DGC-secreted FMOD has some essential yet unidentified functions supporting GSC-initiated tumor growth.

Here, we explored the mechanisms underlying the role of DGCs acting as critical support for GSC-initiated tumor growth. We demonstrate that DGC-secreted FMOD promotes tumor growth by inducing angiogenesis through integrin-dependent Notch signaling in endothelial cells, thus highlighting the importance of DGCs in tumor-stroma interactions that contribute to a sustainable niche for tumor growth. We further investigated the mechanism by which FMOD activates integrin-dependent Notch signaling in endothelial cells. Based on RPPA data which showed upregulation of HES1 in endothelial cells upon FMOD treatment, we demonstrated that activation of Notch signaling is essential for FMOD-induced angiogenesis. The importance of Notch signaling in glioma, especially in GSC growth and angiogenesis, is well documented ***(Bazzoni and Bentivegna, 2019; Stockhausen et al., 2010; Teodorczyk and Schmidt, 2014)***. Similarly, activation of Notch signaling in endothelial cells has been involved in tumor development and angiogenesis ***(Gridley, 2007; Kofler et al., 2011; Phng and Gerhardt, 2009).*** RPPA data also showed an increase in pFAK in FMOD-treated glioma cells. Our previous study showed that FMOD acts on glioma cells via the Integrin-FAK-Src-Rho axis to promote migration ***(Mondal et al., 2017).*** The present study demonstrates that FMOD-activated Integrin signaling is essential for Notch pathway activation in ST1 cells. Integrin signaling in endothelial cells has been shown to play a crucial role in angiogenesis (***Short et al., 1998; Silva et al., 2008***). Based on our results indicating that FMOD-activated Notch signaling in endothelial cells is inhibited by GSI, we predicted that FMOD-elicited activation of the Notch pathway could involve Notch ligand-dependent process. Our experiments identified that JAG1 is the linker molecule that integrates Integrin signaling to the Notch pathway. We also found a significant colocalization of endothelial cell marker CD31 with FMOD, pFAK, JAG1, and HES1 in blood vessels of tumors formed in mouse models. Finally, endothelial cells stably expressing NICD showed enhanced angiogenic network formation in an FMOD-independent manner, suggesting that Notch activation is an essential step in FMOD-induced angiogenesis. Thus, our results show that Integrin-FAK-Src-

bioRxiv preprint doi: https://doi.org/10.1101/2022.04.03.486893; this version posted April 6, 2022. The copyright holder for this preprint (which was not certified by peer review) is the author/funder, who has granted bioRxiv a license to display the preprint in perpetuity. It is made available under aCC-BY 4.0 International license.

KLF8-JAG1-dependent Notch signaling activation in endothelial cells mediates FMOD-induced angiogenesis.

Finally, in an orthotopic intracranial GBM mouse model, we show that conditional silencing of FMOD in newly generated DGCs during tumor growth leads to a significant reduction of tumor growth. Supporting our *in vitro* data indicating that FMOD is not required for GSC growth and their differentiation, we found that the small tumors formed in FMOD-silenced conditions show differentiation of GSCs. However, these tumors exhibited poorly developed blood vasculatures of host-derived endothelial cells and TDECs. The lower tumor burden in the absence of FMOD might be attributed to insufficient nutrient supply to sustain tumor growth due to the reduced blood vessel density. Thus, our study establishes an essential role of paracrine signaling between the DGCs and the stroma in the context of tumor growth in the natural tumor niche complexity. It also demonstrates the importance of FMOD secreted by DGCs in promoting human glioma tumor growth in a mouse model. We propose a tumor evolution model (**Figure 7M**), whereby GSCs, in addition to their self-renewal, continuously differentiate to form DGCs, which secrete protein factors like FMOD that mediate paracrine signaling in the different cell types of the tumor, thus creating a niche favorable to tumor growth.

In conclusion, the present study demonstrates that in addition to GSCs, DGCs have an essential role in tumor growth and maintenance. While the therapy-resistant and self-renewing GSCs trigger the early events of transformation and growth, DGCs, the proportion of which continues to increase during tumor growth, progressively become essential. Thus, targeting both CSCs and differentiated cancer bulk cells is vital to achieving a durable therapeutic response. The study also highlights the potential of GSC and DGC CM analysis to uncover novel targets in cancer therapy and the critical influence of DGC-secreted FMOD in glioma tumor growth.

Author Contributions

SS carried out the experiments, MM carried out bioinformatic analyses, AM helped in some experiments related to cell culture, KRP and PM^{2} helped in animal experiments, SU carried out mass spectrometry experiments, DFM and PM^{4} corrected the manuscript and helped in planning experiments, KS wrote the manuscript and executed the whole study.

bioRxiv preprint doi: https://doi.org/10.1101/2022.04.03.486893; this version posted April 6, 2022. The copyright holder for this preprint (which was not certified by peer review) is the author/funder, who has granted bioRxiv a license to display the preprint in perpetuity. It is made available under aCC-BY 4.0 International license.

Acknowledgments

The results published here are in whole or part based upon data generated by The Cancer Genome Atlas pilot project established by the NCI and NHGRI. Information about TCGA and the investigators and institutions that constitute the TCGA research network can be found at http://cancergenome.nih.gov/. We acknowledge the shRNA consortium (Dr. Subba Rao), IISc, India, for shRNA constructs. SS acknowledges IISc for fellowship. KS acknowledges CEFIPRA DBT, DST, and CSIR (Govt. of India) for research grants. Infrastructure supported by DST FIST, DBT-IISc partnership program, and UGC is acknowledged. KS is awarded J. C. Bose Fellowship from DST. This research was supported in part by grants to DFM from the Israel Science Foundation (Grant no.1315/15 and 1429/20). PM was supported by grants from Fondation pour la Recherche Médicale and CEFIPRA (n° IFC/5603-C/2016/503). Mass spectrometry experiments were carried out using the facilities of the Montpellier Proteomics Platform (PPM, BioCampus Montpellier).

Declaration of Interest

The authors declare no competing interests.

Figure legends

Figure 1: Quantitative proteomics shows higher abundance of fibromodulin under the control of TGFβ signaling in the DGC secretome. A. Volcano plot depicting relative protein abundance in GSC (MGG4, MGG6 and MGG8) *vs.* their corresponding DGC conditioned media (CMs). The black dots represent the non-significant proteins ($p>0.05$), while the red (higher abundance in GSC CM) and green (lower abundance in GSC CM) dots represent the significant ones ($p<0.05$) with a Log_2 fold change cut-off of >0.58 or <-0.58. **B.** Venn diagram showing proteins upregulated in DGC CM and those annotated as ECM proteoglycans. Of the common proteins, FMOD exhibits the highest DGC/GSC ratio (indicated by the more intense red color). **C.** Label-free quantification (LFQ) of FMOD, expressed as Log_2 fold change in GSCs *vs.* DGCs CM. **D.** Real-time qRT-PCR analysis shows upregulation of FMOD transcript in DGCs (red bars) *vs.* GSCs (blue bars). **E.** Western blotting shows the presence of higher amounts of intracellular FMOD in DGCs compared with corresponding GSCs. **F.** Top: Western blotting shows the presence of higher amounts of FMOD in the DGC CM *vs*. GSC CM. Bottom: Equal loading of the

bioRxiv preprint doi: https://doi.org/10.1101/2022.04.03.486893; this version posted April 6, 2022. The copyright holder for this preprint (which was not certified by peer review) is the author/funder, who has granted bioRxiv a license to display the preprint in perpetuity. It is made available under aCC-BY 4.0 International license.

proteins assessed by Ponceau Red staining. **G.** Real-time qRT-PCR analysis showing showing reduction of high FMOD transcript level in DGCs upon treatment SB431542 (10 μM), a TGF-β inhibitor. Red bars indicate FMOD expression, and blue bars represent TGM2 (a bonafide TGF-β pathway target gene) expression. **H.** Western blotting shows that the high FMOD level in DGCs is inhibited by treating cells with SB431542 (10 μM); intracellular-top, and secreted-bottom. Equal loading of the secreted proteins assessed by Ponceau Red staining (bottom). **I.** Western blotting shows higher expression of pSAMD2 in DGCs than in GSCs, which is reduced by SB431542 treatment. **J.** Real-time qRT-PCR shows significantly higher fold enrichment of pSMAD2 in the FMOD promoter, which is inhibited upon SB431542 treatment (10 μM). for panels C, D, G, and J, p-value is calculated by unpaired t test with Welch's correction. p value less than 0.05 is considered significant with *, **, *** representing p value less than 0.05, 0.01 and 0.001 respectively.

Figure 2: DGC-secreted FMOD is essential for tumor growth initiated by GSCs *in vivo* in a co-implantation experiment.

A. Inducible shFMOD lentiviral construct. **B.** Schema depicting the GSC-DGC co-implantation experiment in C57BL/6 mice (n=5 for each group). Mice were injected with a combination of DBT-Luc-GSCs + DBT-Luc-DGCs (two groups for miRNT, Dox+ and Dox-. Same strategy for miRFMOD group.) The control groups were only injected with 10^5 DBT-Luc-GSCs or 10^6 DBT-Luc-DGCs and did not receive doxycycline. **C**. *In vivo* imaging of the injected mice, showing tumor growth over time by both bioluminescence and mCherry fluorescence, according to the timeline shown in **B. D.** Quantification of the total radiance. The different colors represent the different groups of animals. Significant differences between each of the groups were calculated using ANOVA. The p-values for days 28 and 32 are shown. A detailed comparison of the p values between different groups is provided in Supplementary Table 2.

Figure 3: DGC-secreted FMOD promotes angiogenesis. A. Representative images of *in vitro* network formation by ST1 cells treated with LN229/Vector CM *vs.* LN229/FMOD CM. In the positive control condition (top left), cells are plated in complete endothelial cell media (Medium 199) supplemented with Endothelial Cell Growth Factors (ECGS) and 20% FBS, and in the negative control (top right), where cells are plated in incomplete Medium 199 (without serum and ECGS). Significantly more networks are formed when ST1 cells are treated with LN229/FMOD CM (right bottom), compared with cells treated with LN229/Vector CM (left bottom).

bioRxiv preprint doi: https://doi.org/10.1101/2022.04.03.486893; this version posted April 6, 2022. The copyright holder for this preprint (which was not certified by peer review) is the author/funder, who has granted bioRxiv a license to display the preprint in perpetuity. It is made available under aCC-BY 4.0 International license.

Magnification 10X, Scale bar = 100 μm. **B**. Quantification of the number of complete networks formed in **A. C.** Quantification of the number of networks formed by ST1 cells shows that cells treated with U251-DGC/siFMOD (low FMOD) CM form a significantly lesser number of networks than cells treated with U251-DGC/siNT (high FMOD) CM. This reduction in the number of networks is rescued by addition of rhFMOD (400 nM) in U251-DGC/siFMOD CM. **D.** Quantification of the number of networks formed in the *in vitro* angiogenesis assay showing that DGC-secreted FMOD induces network formation by ST1 cells, which is reduced when an FMOD-neutralizing antibody is added to the CM and rescued by adding rhFMOD. Furthermore, MGG8-DGC/shFMOD CM forms lesser networks than MGG8-DGC/shNT CM, which is rescued by adding rhFMOD to the MGG8-DGC/shFMOD CM. **E.** Representative images of *in vitro* network formation by primary human brain-derived microvascular endothelial cells (HBMECs). Significant reduction in the number of networks formed when the cells are treated with MGG8-DGC/shFMOD CM compared with MGG8-DGC/shNT CM, which is rescued by the exogenous addition of rhFMOD. Magnification 4X, Scale bar = 200 μm. **F.** Quantification of the number of complete networks formed in **E. G.** Real-time qRT-PCR analysis showing CD31 (blue bars) and FMOD (orange bars) expression in ST1, MGG8-DGC/shNT and MGG8-DGC/shFMOD cells before and after transdifferentiation (the groups labeled as TDECs represent the transdifferentiated cells). **H.** Western blotting analysis showing the expression of FMOD and CD31 in MGG8-DGC/shNT and MGG8-DGC/shFMOD cells before and after transdifferentiation (the groups labeled as TDECs represent the transdifferentiated cells). **I.** Representative images of *in vitro* network formation by MGG8-DGC/shNT TDECs and MGG8-DGC/shFMOD TDECs upon BSA and rhFMOD treatments. Magnification 4X, Scale bar = 200 μm. **J.** Quantification of the number of complete networks formed in **I.** For panels B, C, D, F, G, and J, p-values were calculated by unpaired t-test with Welch's correction. p values < 0.05 were considered significant with *, **, *** representing p values < 0.05, 0.01 and 0.001 respectively. ns stands for non-significant.

Figure 4: Integrin/FAK/Src/JAG1-dependent Notch pathway activation in endothelial cells mediates FMOD-induced angiogenesis A. Heatmap showing differentially regulated proteins in endothelial cells (treated with vehicle or 400 nM rhFMOD for 10, 30 and 60 min, Log_2 fold change >/< 0.2), assessed by RPPA (Reverse Phase Protein Array). Red and green depict upregulated and downregulated proteins in ST1 cells, respectively. The red arrows indicate HES1 and pFAK. **B.** qRT-PCR analysis shows that rhFMOD treatment of ST1 cells causes a time-dependent increase

bioRxiv preprint doi: https://doi.org/10.1101/2022.04.03.486893; this version posted April 6, 2022. The copyright holder for this preprint (which was not certified by peer review) is the author/funder, who has granted bioRxiv a license to display the preprint in perpetuity. It is made available under aCC-BY 4.0 International license.

in HES1 mRNA, which is inhibited in cells pre-treated with GSI (10 μM). **C.** Western blotting showing rhFMOD treatment of ST1 cells causes an increase in HES1 protein, which is inhibited in cells pre-treated with GSI. **D.** Quantification of the number of networks formed in *in vitro* angiogenesis assay shows that the rhFMOD-mediated increase in the number of networks formed by ST1 cells is abolished in cells pre-treated with GSI. **E.** Western blotting shows a time-dependent increase in phospho-FAK level in FMOD-treated ST1 cells. This increase is suppressed when the cells are pre-treated with RGD peptide (10 μM), an Integrin inhibitor. **F.** Quantification of networks upon treatment of ST1 cells with either LN229/Vector CM or LN229/FMOD CM. ST1 cells are pretreated with the indicated inhibitors (PP2, PP3, and FAK inhibitor- PF573228 were used at a concentration of 10 μM, ROCK1 inhibitor-H1152 was used at a concentration of 0.5 μM, Rac1 inhibitor was used at a concentration of 10 μM). **G.** qRT-PCR analysis shows that rhFMOD treatment of ST1 cells causes a time-dependent increase in HES1 mRNA, which is inhibited in cells are pre-treated with RGD peptide. **H.** Western blotting showing rhFMOD treatment of ST1 cells causes an increase in HES1 protein level, which is inhibited in cells pre-treated with the RGD peptide. **I**. Western blotting validating the knockdown of JAG1 in shJAG1-transfected ST1 cells. **J.** qRT-PCR analysis shows that rhFMOD-induced expression of HES1 mRNA is significantly decreased in ST1/shJAG1 cells compared with ST1/shNT cells. **K.** rhFMOD-induced expression of HES1 protein is decreased in ST1/shJAG1 cells compared with ST1/shNT cells. **L.** Quantification of networks formed in *in vitro* angiogenesis assay upon treatment of ST1/shNT and ST1/shJAG1 cells with BSA or rhFMOD. For panels B, D, F, G, J, and L, the p-value calculated by unpaired t-test with Welch's correction are indicated. p-value less than 0.05 was considered significant with *, **, *** representing p-value less than 0.05, 0.01 and 0.001 respectively.

Figure 5. Conditional silencing of FMOD in DGCs formed *de novo* by GSC-initiated tumors inhibits tumor growth. A. Schema is showing the timeline of the *in vivo* experiments. AGR53-GSCs (stably expressing miRNT or miRFMOD) were injected (1 x 10^5 cells per animal) on Day 0. Tumors were allowed to grow till day 13, and then doxycycline (100 μg/animal) administration was started. Please note, *in vitro* characterization show that the highest knockdown of FMOD was obtained on the 7^{th} day after doxycycline administration. First, *in vivo* imaging for mCherry expression depicting tumor size was done on day 21 post-injection, followed by imaging at regular intervals (as noted by the orange marks). **B.** *In vivo* fluorescence imaging of mice injected with either AGR53-GSC/miRNT or AGR53-GSC/miRFMOD cells. **C.** Radiance Efficiency for each

bioRxiv preprint doi: https://doi.org/10.1101/2022.04.03.486893; this version posted April 6, 2022. The copyright holder for this preprint (which was not certified by peer review) is the author/funder, who has granted bioRxiv a license to display the preprint in perpetuity. It is made available under aCC-BY 4.0 International license.

time point in the two groups of animals was plotted as a measure of tumor size at the indicated days. **D**. Kaplan-Meier graphs showing the survival of mice bearing AGR53-GSC/miRNT (Dox+) and AGR53-GSC/miRFMOD (Dox+) cells. **E.** Haematoxylin and Eosin staining show a larger tumor (depicted by dark blue color due to extremely high cell density) in mice brain injected with AGR53-GSC/miRNT (Dox+) cells (top), compared to that of AGR53-GSC/miRFMOD (Dox+) cells (bottom). Magnification=0.8 X **F**. Immunohistochemical analysis showing FMOD expression in brains of mice injected with AGR53-GSC/miRNT (Dox+) and AGR53-GSC/miRFMOD (Dox+) cells. Red indicates FMOD, and Blue indicates H33342. The merged images have been shown for representation. Magnification = 20x, Scale= 50 μm **G.** Brain sections showing areas of fluorescence for both AGR53-GSC/miRNT (Dox+) (left panel) and AGR53-GSC/miRFMOD (Dox+) (right panel) groups of animals. Please note that AGR53 cell lines stably express GFP. mCherry expression is induced upon doxycycline addition. On day 13, prior to the administration of doxycycline, both miRNT(left) and miRFMOD (right) do not have any mCherry expression but have almost equal GFP expression. However, over time after the onset of doxycycline administration, both mCherry and GFP expression decreased in miRFMOD group but not in the miRNT group. Merged images show an overlap of GFP and mCherry-positive tumor areas. Magnification=20x, Scale= 50μm . For panels C and D, p-value less than 0.05 was considered significant with *, **, *** representing p-value less than 0.05, 0.01, and 0.001, respectively.

Figure 6: Growth of human GSC-initiated tumors require secreted FMOD A. Flow-cytometry analysis showing enrichment of CD133-positive cells in MGG8-GSCs compared to MGG8-DGCs. **B.** Kaplan-Meier graphs showing the survival of mice injected with MGG8-GSC/shNT or MGG8-GSC/shFMOD cells. **C.** Haematoxylin and Eosin staining showing tumors in brains of mice injected with MGG8-GSC/shNT and MGG8-GSC/shFMOD cells. Magnification= 0.8 X **D.** Immunohistochemical labeling showing FMOD expression in brains of mice injected with MGG8-GSC/shNT or MGG8-GSC/shFMOD cells. Red indicates FMOD, and Blue indicates H33342. The merged images have been shown for representation. Magnification = 20x, Scale, 50 μm. **E.** *In vivo* bioluminescence imaging of two groups of animals injected with either U251/shNT or U251/shFMOD cells. The tumor formation was followed over 26 days. **F.** Total radiance for each time point was plotted as an index of tumor size for both animal groups. **G.** Kaplan-Meier graphs showing the survival of mice injected with U251-DGC/shNT or U251-DGC/shFMOD cells. **H.** Haematoxylin and Eosin staining showing tumors in brains of mice

bioRxiv preprint doi: https://doi.org/10.1101/2022.04.03.486893; this version posted April 6, 2022. The copyright holder for this preprint (which was not certified by peer review) is the author/funder, who has granted bioRxiv a license to display the preprint in perpetuity. It is made available under aCC-BY 4.0 International license.

injected with U251-DGC/shNT or U251-DGC/shFMOD cells. Scale= 0.8 X. **I.** Immunohistochemical analysis showing FMOD expression in brains of mice injected with U251-DGC/shNT or U251-DGC/shFMOD cells. Red indicates FMOD, and Blue indicates H33342. The merged images have been shown for representation. Magnification = 20x, Scale = 50 μm. For panels B, F, and G, a p-value less than 0.05 was considered significant with *, **, *** representing p values less than 0.05, 0.01, and 0.001, respectively. ns stands for non-significant.

Figure 7: Reduced angiogenesis is characteristic of tumors initiated by FMOD-silenced glioma cells. A. Immunohistochemical analysis showing blood vessels lined by cells expressing CD31 in brains of mice injected with AGR53-GSC/miRNT or AGR53-GSC/miRFMOD cells after doxycycline administration. **B.** Quantification of the mean fluorescence intensity of CD31 in brains of mice injected with AGR53-GSC/miRNT or AGR53-GSC/miRFMOD cells after doxycycline administration. **C.** Quantification of the mean area of blood vessels in brains of mice injected with AGR53-GSC/miRNT or AGR53-GSC/miRFMOD cells after doxycycline administration. **D.** Immunohistochemical analysis showing CD31 expression in brains of mice injected with MGG8-GSC/shNT or MGG8-GSC/shFMOD. **E.** Quantification of the mean fluorescence intensity of CD31 in brains of mice injected with MGG8-GSC/shNT or MGG8-GSC/shFMOD cells. **F.** Quantification of the mean, mean area of blood vessels in brains of mice injected with MGG8-GSC/shNT or MGG8-GSC/shFMOD cells. **G.** Immunohistochemical analysis showing overlap of CD31 (red) and GFP (green) expression in brains of mice injected with AGR53-GSC/miRNT or AGR53-GSC/miRFMOD cells after doxycycline administration. The yellow arrow indicates the region exhibiting colocalization of both markers. **H.** Quantification of the colocalization coefficient in the AGR53-GSC/miRNT and AGR53-GSC/miRFMOD groups of animals after doxycycline injection. **I.** Quantification of the TDEC+ blood vessels, indicating the measure of vascular mimicry (VM) in the AGR53-GSC/miRNT and AGR53-GSC/miRFMOD groups. **J.** Immunohistochemical analysis showing overlap of CD31 (red) and GFAP (green) expression in brains of mice injected with MGG8-GSC/shNT or MGG8-GSC/shFMOD cells. The yellow arrow indicates the region exhibiting colocalization of both markers **K.** Quantification of the colocalization coefficient in the MGG8-GSC/shNT and MGG8-GSC/shFMOD groups. **L.** Quantification of the TDEC+ blood vessels, indicating the measure of vascular mimicry (VM) in the MGG8-GSC/shNT and MGG8-GSC/shFMOD groups. **M.** A model depicting how GBM tumors are made up of a small proportion of GSCs, and a massive number of DGCs that form the

bioRxiv preprint doi: https://doi.org/10.1101/2022.04.03.486893; this version posted April 6, 2022. The copyright holder for this preprint (which was not certified by peer review) is the author/funder, who has granted bioRxiv a license to display the preprint in perpetuity. It is made available under aCC-BY 4.0 International license.

tumor bulk. FMOD, primarily secreted by DGCs, upregulates JAG1 through the activation of integrin signaling in ST1 cells. The higher expression of JAG1 causes the activation of the Notch signaling pathway, which results in the transcriptional upregulation of HES1 in endothelial cells. The integrin-dependent Notch pathway activation promotes angiogenesis and vascular mimicry, leading to glioma tumor growth. For panels A, D, G, and J, the magnification used is 20 X (Scale = 50 μm). For panels B, C, E, F, H, I, K, and L, a p-value less than 0.05 was considered significant with *, **, *** representing a p-value less than 0.05, 0.01, and 0.001, respectively.

MATERIALS AND METHODS

RESOURCE AVAILABILITY

Further information and requests for resources and reagents should be directed to and will be fulfilled by the lead contact Dr. Kumaravel Somasundaram (skumar1@iisc.ac.in).

MATERIALS AVAILABILITY

This study did not generate any new unique reagents.

DATA AND AVAILABILITY

Label-free mass spectrometry data between the GSC and DGC showing protein ratios in the GSC and DGC secretome and p values are shown on Supplementary Table S1 for proteins exhibiting significant differences in abundance in both conditions. The mass spectrometry data obtained the current study are available from the corresponding author on request.

EXPERIMENTAL MODEL AND SUBJECT DETAILS

Experiments were performed in C57&BL/6J female mice and Athymic Nude female mice (6-8 week old) following the approved by the Institute Ethical Committee for Animal Experimentation. The mice were kept in a 12h light and dark cycle, fed *ad libitum* with a normal diet and the experiments were done in the light phase of the cycle.

Cell lines used:

The GBM adherent cell lines LN229 and U251 were purchased from Sigma Aldrich, Saint Louis, Missouri, USA. Primary human tumour-derived GSCs MGG4, MGG6, and MGG8 were kindly gifted by Dr. Wakimoto (Massachusetts General Hospital, Boston, USA). AGR53 mouse-derived cell line is described before ***(Angel et al., 2020).*** DBT-Luc cells were a kind gift from Dr. Dinesh Thotala, Washington University in St. Louis St Louis, Missouri, United States. ST1 endothelial cells were a kind gift from Dr. Ron Unger, Johannes Gutenberg University, Germany. B.End3 cell

bioRxiv preprint doi: https://doi.org/10.1101/2022.04.03.486893; this version posted April 6, 2022. The copyright holder for this preprint (which was not certified by peer review) is the author/funder, who has granted bioRxiv a license to display the preprint in perpetuity. It is made available under aCC-BY 4.0 International license.

line purchased from The American Type Culture Collection (ATCC, #CRL-2299). The HBMECs were purchased from Cell Biologics, USA (#H-6023).

Plasmids:

The RAR3G vector (in which miRNT and miRFMOD are cloned for the inducible shRNA experiments) is previously described (***Friedmann-Morvinski et al., 2012***). shRNA for FMOD (miRFMOD) was cloned following the mir30 (miRNT) inducible backbone under the TRE (Tetracycline response element) promoter which is placed downstream of mCherry reporter gene. The m2RtTA transactivator is expressed from the same vector in the opposite direction under the EF1α promoter, and following a 2A peptide, the puromycin gene is placed for selection *in vitro*. The FMOD overexpression plasmid was bought from Origene, USA (#LY419579). NICD pCMV Neo/intracellular domain of human Notch1 (NIC-1) and CSL Luc were kind gifts from Prof. Thomas Kandesch, Department of Genetics, University of Pennsylvania School of Medicine. Hes-Luc plasmid was bought from Addgene, USA (#43806).

Antibodies used:

Primary antibodies: FMOD (Abgent AP9243b, 1:2000), FAK (Cell Signaling Technology 3285S, 1:1000), pFAK (Cell Signaling Technology #3283S, 1:500), GAPDH (Sigma #G8795, 1:20,000), Actin (Sigma A3854, 1:20,000), HES1 (Cell Signaling Technology #D6P2U, 11988S, 1:1000), vWF (Abcam #6994, 1:2000), CD31 (Cell Signaling Technology #89C2, Mouse mAb 1:200 for IHC), JAG1 (Cell Signaling Technology, Jagged1 (D4Y1R) XP® Rabbit mAb #70109, 1:200 for IHC, 1:1000 for WB), FMOD (Fibromodulin Polyclonal Antibody PA5-26250, Invitrogen, IHC 1:100, WB 1:1000), CD133 (Recombinant Anti-CD133 antibody-EPR20980-104 #ab216323 abcam, Flow Cyt. 1:100, Prom1 Monoclonal Antibody-2F8C5, #MA1-219, IHC 1:100), SOX2 (Cell Signaling Technology #3579 Rabbit mAb, IHC 1:100), GFAP (Anti-GFAP antibody ab7260, abcam ICC 1:200, Recombinant Anti-GFAP antibody [EPR1034Y] - Mouse IgG2a (ab279290), IHC 1:200), NICD (NOTCH1 (Cleaved Val1744) Polyclonal Antibody PA5-99448, WB 1:200), SMAD2 (Smad2 (D43B4) XP® Rabbit mAb #5339, Wb 1:1000), pSMAD2 (Phospho-SMAD2 (Ser465/Ser467) (E8F3R) Rabbit mAb #18338, WB 1:1000), Integrin beta-1 (Cell Signaling Technology #9699 Rabbit mAb, WB 1:1000), Integrin alphaV (Cell Signaling Technology #4711 Rabbit Ab, WB 1:1000), Integrin alpha-6 (Recombinant Anti-Integrin alpha 6 antibody [EPR18124] (ab181551), WB 1:500), KLF8 (Anti-KLF8 antibody (ab168527), WB 1:500)

bioRxiv preprint doi: https://doi.org/10.1101/2022.04.03.486893; this version posted April 6, 2022. The copyright holder for this preprint (which was not certified by peer review) is the author/funder, who has granted bioRxiv a license to display the preprint in perpetuity. It is made available under aCC-BY 4.0 International license.

Secondary antibodies: Goat Anti mouse HRP conjugate (Biorad #170-5047, WB 1:5000), Goat anti rabbit (H+L) secondary HRP conjugate (Invitrogen, #31460, WB 1:5000), Goat anti-Mouse IgG (H+L) Highly Cross-Adsorbed Secondary Antibody, Alexa Fluor 488) (Invitrogen, #A-11029), Goat anti-Rabbit IgG (H+L) Highly Cross-Adsorbed Secondary Antibody, Alexa Fluor 488 (Invitrogen, # Catalog # A-11034), Goat anti-Mouse IgG (H+L) Highly Cross-Adsorbed Secondary Antibody, Alexa Fluor 594 (Invitrogen, # Catalog # A-11032), Goat anti-Rabbit IgG (H+L) Highly Cross-Adsorbed Secondary Antibody, Alexa Fluor 594 (Invitrogen, # Catalog # A-11037), Goat anti-Rabbit IgG (H+L) Highly Cross-Adsorbed Secondary Antibody, Alexa Fluor 405 Plus (Invitrogen, # A48254), Goat anti-Mouse IgG (H+L) Highly Cross-Adsorbed Secondary Antibody, Alexa Fluor 405 Plus (Invitrogen, # Catalog # A48255). All Alexafluor conjugated antibodies were used at a dilution of 1:500 for IHC and ICC.

Resource Table

REAGENT or RESOURCE	SOURCE	IDENTIFIER
Antibodies		
Rabbit polyclonal anti-FMOD	Abgent	Cat# AP9243b RRID:AB_10612142
Rabbit polyclonal anti-FAK	Cell Signaling Technology	Cat#T9026; RRID: AB_477593 RRID:AB_2269034
Rabbit polyclonal anti-phospho FAK (Tyr397)	Cell Signaling Technology	Cat# 3283, RRID:AB_2173659
Mouse Anti-GAPDH Monoclonal Antibody, Unconjugated, Clone GAPDH-71.1	Sigma-Aldrich	Cat# G8795, RRID:AB_1078991
Mouse Anti-Actin, beta Monoclonal Antibody, Horseradish Peroxidase Conjugated, Clone AC-15	Sigma-Aldrich	Cat# A3854, RRID:AB_262011
Rabbit Monoclonal HES1 (D6P2U) antibody	Cell Signaling Technology	Cat# 11988, RRID:AB_2728766
Rabbit polyclonal Von Willebrand Factor antibody	Abcam	Cat# ab6994, RRID:AB_305689
Mouse monoclonal CD31 antibody	Cell Signaling Technology	Cat#89C2 RRID:AB_2160882
JAG1 Rabbit monoclonal antibody	Cell Signaling Technology	Cat#70109 RRID: AB_2799774
FMOD Rabbit polyclonal antibody	Invitrogen	Cat#PA5-26250 RRID: AB_2543750

bioRxiv preprint doi: https://doi.org/10.1101/2022.04.03.486893; this version posted April 6, 2022. The copyright holder for this preprint (which was not certified by peer review) is the author/funder, who has granted bioRxiv a license to display the preprint in perpetuity. It is made available under aCC-BY 4.0 International license.

CD133 Recombinant antibody	Abcam	Cat#ab216323 RRID: AB_2847920
Prom1 Monoclonal antibody	Invitrogen	Cat#MA1-219 RRID: AB_2725113
SOX2 Rabbit monoclonal antibody	Cell Signaling Technology	Cat#3579 RRID: AB_2195767
GFAP Mouse antibody	Abcam	Cat#ab279290 RRID: AB_1209224
GFAP Recombinant antibody	Abcam	Cat#ab7260 RRID:AB_305808
NOTCH1 Polyclonal antibody	Invitrogen	Cat#PA5-99448 RRID:AB_2818381
SMAD2 Rabbit monoclonal antibody	Cell Signaling Technology	Cat#5339 RRID:AB_10626777
pSMAD2 Rabbit monoclonal antibody	Cell Signaling Technology	Cat#18338 RRID:AB_2798798
Integrin beta-1 Rabbit monoclonal antibody	Cell Signaling Technology	Cat#9699 RRID:AB_11178800
Integrin alpha-V Rabbit monoclonal antibody	Cell Signaling Technology	Cat#4711 RRID:AB_2128178
Integrin Alpha 6 antibody	Abcam	Cat#ab181551 RRID:
KLF8 antibody	ABcam	Cat#ab168527 RRID:
Goat Anti mouse HRP conjugate	Biorad	Cat#170-5047 RRID:AB_11125753
Goat anti rabbit (H+L) secondary HRP conjugate	Invitrogen	Cat#31460 RRID: AB_228341
Goat anti-Mouse IgG (H+L) Highly Cross-Adsorbed Secondary Antibody, Alexa Fluor 488	Invitrogen	Cat#A-11029 RRID: AB_138404
Goat anti-Rabbit IgG (H+L) Highly Cross-Adsorbed Secondary Antibody, Alexa Fluor 488	Invitrogen	Cat#A-11034 RRID:AB_2576217
Goat anti-Mouse IgG (H+L) Highly Cross-Adsorbed Secondary Antibody, Alexa Fluor 594	Invitrogen	Cat#A-11032 RRID:AB_2534091
Goat anti-Rabbit IgG (H+L) Highly Cross-Adsorbed Secondary Antibody, Alexa Fluor 594	Invitrogen	Cat#A-11037 RRID:AB_2534095
Goat anti-Rabbit IgG (H+L) Highly Cross-Adsorbed Secondary Antibody, Alexa Fluor 405 Plus	Invitrogen	Cat#A48254 RRID:AB_2890548
Goat anti-Mouse IgG (H+L) Highly Cross-Adsorbed Secondary Antibody, Alexa Fluor 405 Plus	Invitrogen	Cat#A48255 RRID:AB_2890536
Biological samples		
Healthy adult C57BL/6 brain tissue	In this study	
GBM adult C57BL/6 brain tissue	In this study	

bioRxiv preprint doi: https://doi.org/10.1101/2022.04.03.486893; this version posted April 6, 2022. The copyright holder for this preprint (which was not certified by peer review) is the author/funder, who has granted bioRxiv a license to display the preprint in perpetuity. It is made available under aCC-BY 4.0 International license.

Healthy adult nude mice brain tissue	In this study	
GBM adult nude mice brain tissue	In this study	
GBM adult C57BL/6 subcutaneous tumor tissue	In this study	
Chemicals, peptides, and recombinant proteins		
γ-Secretase inhibitor (GSI)	Merck	565750
RGD peptide (Integrin inhibitor)	Sigma-Aldrich	**A8052** CAS Number: 99896-85-2
FAK inhibitor (PF-573228)	Sigma-Aldrich	PZ0117 CAS Number: 869288-64-2
PP2 (Src inhibitor)	Sigma-Aldrich	**P0042**; CAS Number: 172889-27-9
PP3 (negative control, structural analogue of PP2)	Sigma-Aldrich	529574 CAS 5334-30-5
ROCK1 inhibitor	Sigma-Aldrich	555550 CAS 871543-07-6
RAC1 inhibitor	Sigma-Aldrich	553502 CAS 1177865-17-6
TGFB R1 inhibitor SB431542	Sigma-Aldrich	616464 CAS 301836-41-9
Fibromodulin (FMOD) (NM_002023) Human Recombinant Protein	Origene	**CAT#: TP306534**
Deposited data		
Label-free mass spectrometry performed with conditioned media from MGG4, MGG6 and MGG8 GSC vs DGC.	This paper	Supplementary Table S1
Experimental models: cell lines		
Human cell line: LN229	Sigma Aldrich	
Human cell line: U251-MG	Sigma Aldrich	09063001
Human cell line: MGG4, MGG6. MGG8	Gift from Dr. Wakimoto (Massachusetts General Hospital, Boston, USA).	
Mouse Cell line: AGR-53	Lab of Dr. Dinorah Friedmann-Morvinski, Tel Aviv University, Israel	
Mouse Cell line: DBT-Luc	Lab of Dr. Dinesh Thotala, Washington University in St. Louis St Louis, Missouri, United States	
Human Cell line: ST1 (HPMECs)	Lab of Dr. Ron Unger, Johannes Gutenberg University, Germany.	
Human brain-derived microvascular endothelial cells (HBMECs)	Cell Biologics, USA	#H-6023
B.End3 Mouse brain-derived immortalized endothelial cells	The American Type Culture Collection	#CRL-2299
Experimental models: organisms/strains		

bioRxiv preprint doi: https://doi.org/10.1101/2022.04.03.486893; this version posted April 6, 2022. The copyright holder for this preprint (which was not certified by peer review) is the author/funder, who has granted bioRxiv a license to display the preprint in perpetuity. It is made available under aCC-BY 4.0 International license.

Mouse: C57BL/6J, females, 6-8 weeks old	The Jackson Laboratory	JAX:000664
Mouse: Athymic nude, Nude, 6-8 weeks old, females	The Jackson Laboratory	JAX 002019
Oligonucleotides		
All shRNA sequences used in the study are provided in the methods section.		
Primers for gene expression, detail given in the methods section		
Recombinant DNA	Gene Tools	
Plasmid: RAR3G (TetOn)	Lab of Dr. Dinorah Friedmann-Morvinski	
Plasmid: FMOD overexpression construct in pcMV-entry backbone	Origene	#LY419579
Plasmid: CSL Luc	Lab of Prof. Thomas Kandesch, Department of Genetics, University of Pennsylvania School of Medicine.	
Plasmid: pHes1(2.5k)-luc	Addgene	Cat # 43806
NICD pCMV Neo/intracellular domain of human Notch1 (NIC-1)	Lab of Prof. Thomas Kandesch, Department of Genetics, University of Pennsylvania School of Medicine.	
Software and algorithms		
ImageJ	Chen et al., 2013	
MaxQuant software package	Cox et al., 2008	
Zen Black from Zeiss	https://www.zeiss.com/microscopy/int/products/microscope-software/zen.html	
Other		
Reverse Phase Protein Array (RPPA) analysis	https://www.mdanderson.org/research/research-resources/core-facilities/functional-proteomics-rppa-core.html	M.D. Anderson Cancer Center, University of Texas, USA.

Neurosphere culturing

The GSCs are obtained by dissecting GBM tumor tissue and then treating with Tryspin, followed by Trypsin inhibitor. The chopped tissue is then passed through a cell strainer to remove the debris and the obtained filtrate is plated in ultra-low attachment plates using the stem cell for neurosphere formation media described in the following sentence. Then neurospheres were grown in Neurobasal medium (#21103049, Gibco) supplemented with 1X L-Glutamine (# 25030081, stock 200 mM i.e.,100X, Gibco), Heparin 2µg/ml (#H3393 Sigma), 1X B27 supplement

bioRxiv preprint doi: https://doi.org/10.1101/2022.04.03.486893; this version posted April 6, 2022. The copyright holder for this preprint (which was not certified by peer review) is the author/funder, who has granted bioRxiv a license to display the preprint in perpetuity. It is made available under aCC-BY 4.0 International license.

(#17504044, Gibco, stock concentration 50X), 0.5X N2 supplement (#17502048, Gibco, stock concentration 100X), 20ng/ml rhEGF (#g5021, Promega), 2ng/ml rhFGF-basic (#100-18B-100 µg, Peprotech) and Penicillin and Streptomycin. To make single-cell suspensions for re-plating, the spheres are chemically dissociated after 7 days of plating, using NeuroCult™ Chemical Dissociation Kit (Mouse, #05707) from Stem Cell Technologies according to the manufacturer's instructions.

Differentiation of GSCs to DGCs

For differentiation of GSCs to DGCs, fully grown neurospheres were collected from the ultra-low attachment plates (Corning, USA) and plated on normal cell culture dishes in DMEM media supplemented with 10% FBS and antibiotics as mentioned earlier, for 15-20 days (***Suva et al., 2014***).

Reprogramming of DGCs

The differentiated counterparts of GSCs as well as differentiated GBM cell lines were removed from 10% FBS containing DMEM, spun down twice in PBS to remove any trace of FBS and plated on ultra-low attachment plates in Neurobasal medium containing all the supplements mentioned earlier and antibiotics for 7-10 days.

Neurosphere assay

Viral infection was done in the GSCs using lentivirus for non-targeting shRNA (shNT) or shRNA for the gene of interest. The small pellets of cells were collected 48 hours after viral infection, dissociated to form single cells that were counted and re-plated in 6-well plates (30,000 cells/well) in complete Neurobasal medium. At the same time, cells were harvested and checked for specific gene manipulation (like knockdown verification). Media was replenished every 2-3 days and sphere formation was monitored till the 6^{th} or 7^{th} day after re-plating. The number of spheres, sphere diameter and size were analyzed using Image J software. Spheres having area less than 50 μm^2 were excluded from the analysis.

Limiting Dilution assay

For each condition, 1, 10, 50, 100 and 200 GSCs (single cells) were plated in 10 wells each, respectively, of a 96-well plate and sphere formation was assessed over the next 5-7days. The number of wells not forming spheres were counted and plotted against the number of cells per well. Extreme Limiting Dilution Assay using the ELDA software available online (https://www.elda.at/cdscontent/?contentid=10007.854970&portal=eldaportal).

bioRxiv preprint doi: https://doi.org/10.1101/2022.04.03.486893; this version posted April 6, 2022. The copyright holder for this preprint (which was not certified by peer review) is the author/funder, who has granted bioRxiv a license to display the preprint in perpetuity. It is made available under aCC-BY 4.0 International license.

CM collection, concentration and sample preparation for mass spectrometry

GSC cell lines growing as neurospheres were grown in complete Neural Stem Cell medium containing Glutamine, Heparin, N2, B27, EGF and FGF for 6 days. They were thoroughly washed using PBS and re-plated without disrupting them in Neural Stem Cell medium devoid of supplements and growth factors. Thirty-six hours after plating in incomplete medium, the conditioned medium was collected, spun at 1,500 rpm for 15 min, filtered using 0.45 micron syringe filters and stored at -80°C. The DGCs were grown in complete DMEM supplemented with 10% FBS, then washed with PBS and CM was collected after 36 hours in incomplete medium and similarly stored.

The conditioned media were concentrated using Centricons (3 kDa cut off; Merck) from 8 ml to 100 µl, followed by precipitation of proteins with trichloroacetic acid (TCA 10% for 30 min at 4°C). Equal amounts of proteins from each condition were run on gradient (4-20 %) SDS gels and stained with Colloidal Coomassie blue. The gels were then destained and each lane cut into 5 equal pieces. Proteins were digested in-gel using trypsin (Gold Promega, 1 µg per band, overnight at 30°C,) as previously described (***Thouvenot et al., 2008***).

Mass Spectrometry, protein identification and relative quantification

Trypsic peptides were analysed online by nano-flow liquid chromatography coupled to tandem-mass spectrometry using a Q-Exactive+ mass spectrometer (Thermo Fisher Scientific, Waltham USA) coupled to a RSLC-U3000 HPLC (Thermo Fisher Scientific). Desalting and pre-concentration of samples were performed on-line on a Pepmap® pre-column (0.3 mm × 10 mm, Dionex). A gradient consisting of 2–25% B for 80 min, 25-40 % B for 20 min and finally 40-90% B for 5 min (A = 0.1% formic acid; B = 0.1% formic acid in 80% acetonitrile) at 300 nL/min was used to elute peptides from the capillary reverse-phase column (0.075 mm × 150 mm, Acclaim Pepmap 100® C18, Thermo Fisher Scientific). Eluted peptides were electro-sprayed online at a voltage of 1.5 kV into the Q-Exactive+ mass spectrometer. A cycle of one full-scan mass spectrum (MS1, 375–1,500 m/z) at a resolution of 70,000, followed by 12 data-dependent tandem-mass (MS2) spectra was repeated continuously throughout the nano-LC separation. Parameters used for MS2 spectra were: resolution of 17,500, AGC target of 1e5, a normalized collision energy of 28 and an isolation window of 1.2 m/z. Mass spectra were processed using the MaxQuant software package (v 1.5.5.1, ***Cox and Mann, 2008***) against the UniProtKB Reference proteome UP000005640 database for Homo sapiens (release 2018_11) and contaminant database. The

bioRxiv preprint doi: https://doi.org/10.1101/2022.04.03.486893; this version posted April 6, 2022. The copyright holder for this preprint (which was not certified by peer review) is the author/funder, who has granted bioRxiv a license to display the preprint in perpetuity. It is made available under aCC-BY 4.0 International license.

following parameters were used: enzyme specificity set as Trypsin/P with a maximum of two missed cleavages, Oxidation (M) and Acetyl (Protein N-term) set as variable modifications and carbamidomethyl (C) as fixed modification, and a mass tolerance of 0.5 Da for fragment ions. The maximum false peptide and protein discovery rate was specified as 0.01. Match between runs was used to transfer identification from run to run. Relative protein quantification was performed using LFQ intensity in MaxQuant. For statistical analysis, missing values were defined using the imputation tool of the Perseus software (v. 1.6.1.1, ***Tyanova et al., 2016***).

Lentivirus preparation and transduction of cells

HEK-293T cells were seeded in 60 mm or 90 mm Poly-L-Lysine coated cell culture dishes. The cells were transfected with shRNA plasmid and helper plasmids psPAX2 and pMD2.G using Opti-MEM (Invitrogen #22600-050) medium and lipofectamine (https://www.thermofisher.com/order/catalog/product/12566014 Invitrogen), when the cells were 60-70% confluent. Six hours after transfection, the Opti-MEM medium was replaced by fresh DMEM medium supplemented with 10% FBS. Sixty hours post-transfection, the supernatant from the transfected cells were collected in 15 ml falcon tubes, centrifuged at 5000 rpm for 10 min, filtered through 0.45 μm, and stored in -80^{o} C for future use.

For virus used in endothelial cells, DMEM was removed after 24 hours of transfection and changed to complete M199 and the virus was collected after sixty hours as mentioned previously. The same method was used for virus to be used for GSCs (DMEM was changed to NBM).The shRNA construct number TRCN0000152163 from Sigma human TRC shRNA library was used for knockdown studies of human FMOD. The shRNA construct number TRCN000094248 from Sigma mouse TRC shRNA library was used for knockdown studies of mouse FMOD. A pooled lentivirus using the construct numbers TRCN000024441, TRCN000024441, TRCN000024441, and TRCN000024420 were used for knock-down studies of JAG1 in the ST1 cells.

Endothelial cell culture

ST1 cells were grown in Medium 199 (Sigma #M4530) supplemented with 20% FBS and ECGS (Sigma #E2759), Heparin, Glutamine (1X) and 1X Antibiotic-Antimycotic Solution (Sigma, # A5955, stock concentration 100X).

bioRxiv preprint doi: https://doi.org/10.1101/2022.04.03.486893; this version posted April 6, 2022. The copyright holder for this preprint (which was not certified by peer review) is the author/funder, who has granted bioRxiv a license to display the preprint in perpetuity. It is made available under aCC-BY 4.0 International license.

Transdifferentiation of DGCs

The MGG8-DGCs were grown in Medium 199 having the same composition as mentioned above, for three days and subjected to hypoxia (1% O_2) for 8 hours. The cells then formed transdifferentiated endothelial cells (TDECs), showed endothelial morphology (data not shown), were harvested for checking markers levels, and were also plated for the *in vitro* angiogenesis assay.

NICD stable generation

For NICD stable cell-line generation, the ST1 cells were transfected with NICD pCMV Neo/intracellular domain of human Notch1 (NIC-1) plasmid using Lipofectamine 200 (Invitrogen), and then were harvested 48 hours after transfection for western blot and *in vitro* angiogenesis assay.

RNA isolation, cDNA conversion and Real-Time Quantitative RT-PCR analysis

Total RNA from the cells was isolated from cells using the TRI reagent (#T9424 Sigma) according to the manufacturer's instructions. Next, the integrity of the RNA was checked by running it on 2% MOPS-formaldehyde gel. RNAs were quantified by Nanodrop. Two µg of total RNA were used for cDNA conversion using the High capacity cDNA reverse transcription kit (Applied Biosystems, USA) according to the manufacturer's protocol. The cDNAs were diluted in a ratio of 1:10 with nuclease-free water to make its final concentration 10 ng/µl. Subsequently, real-time quantitative PCR was done using the ABI Quant Studio 5 and 6 (Life technologies, USA). The cDNA was used as template and DyNAmo Flash SYBR Green qPCR kit (#F-416L) was used. Gene-specific primer sets were used for the reaction (Table at the end of the Methods section0) under the following conditions: 95°C for 15 min, 40 cycles of 95°C for 20 sec, 60°C for 25 sec and 72°C for 30 sec followed by the dissociation cycle for melt curve generation. Each sample was run either in duplicate or triplicate. GAPDH (Glyceraldehyde 3-phosphate dehydrogenase), ACTB (beta actin), 18S rRNA, RPL35a (ribosomal protein L35a) and *ATP5G1* [ATP synthase, H+ transporting, mitochondrial F0 complex, subunit C1 (subunit 9)] were used as reference genes for human gene expression analysis. For mouse gene expression analysis,

bioRxiv preprint doi: https://doi.org/10.1101/2022.04.03.486893; this version posted April 6, 2022. The copyright holder for this preprint (which was not certified by peer review) is the author/funder, who has granted bioRxiv a license to display the preprint in perpetuity. It is made available under aCC-BY 4.0 International license.

Cyclophilin was used as a housekeeping gene. ΔΔCT method was used for the calculation of gene expression, which was transformed to log2 ratio and then to absolute scale for plotting.

Western Blotting

For Western blot analysis, cell pellets were lysed in RIPA lysis buffer (containing 1 mM sodium orthovanadate, 5mM sodium fluoride, 1 mM phenylmethanesulfonyl fluoride and 1X protease inhibitor cocktail, Sigma, USA), and proteins were isolated from the cells by spinning at 13,000 rpm for 30 mins. The supernatant, containing the proteins was collected. Protein concentrations were measured using the Bradford's reagent and a standard BSA curve was used to determine the protein concentrations. Equal amounts of proteins from all conditions were mixed with protein loading dye (1X), denatured at 95°C for 15 mins, loaded in each well of an SDS polyacrylamide gel and the gel was run for around 8 hours. For preparation of SDS-polyacrylamide gel, resolving and stacking gels were prepared at a concentration of 10-12 concentrations.. The gel was run at 70V-100V and then the proteins were transferred onto a polyvinyl fluoride (PVDF) membrane using the semi-dry transfer method. After the transfer, the membrane was blocked using 5% skimmed milk in 1X Tris-buffered saline-Tween (TBST) for 1 h. Subsequently, the membrane was washed in TBST for 30 min and probed initially with primary antibodies in 5% BSA-TBST for 14-16 hours at 4°C. Then the membrane was washed in TBST for 30 min and secondary antibody, diluted in 5% skimmed milk in TBST was added and incubated at room temperature for 2-3 h. Finally, the blot was washed and developed using Perkin-Elmer ECL Plus lightning and Biorad Clarity and Clarity Plus ECL chemiluminescent reagent using GE Image Quant machine.

Chromatin immunoprecipitation (ChIP)

ChIP assay was conducted with chromatin isolated from ST1 cells treated with 10 μM TGFβ RI inhibitor (SB431542) and DMSO for 6 hrs. Briefly, after cross-linking, the nuclei were prepared and sonicated to generate chromatin fragments between 100 and 10,000 bp following the manufacturer's protocol using Simple Chromatin Immunoprecipitation kit (CST; Cat no. 9003). The sheared chromatin was collected by centrifugation (10000g for 10 min at 4°C) and a 10 μL aliquot was removed to serve as a positive input sample. Aliquots of 100 μL sheared chromatin

bioRxiv preprint doi: https://doi.org/10.1101/2022.04.03.486893; this version posted April 6, 2022. The copyright holder for this preprint (which was not certified by peer review) is the author/funder, who has granted bioRxiv a license to display the preprint in perpetuity. It is made available under aCC-BY 4.0 International license.

were incubated with 2 µg of the required antibody/antibodies followed by Protein G magnetic beads for the stipulated time. An equal amount of IgG and H3 antibodies were used as controls. The eluted DNA was analyzed by quantitative PCR using the FMOD promoter-specific primer set ChIP-F/ChIP-R (in list of primers) to amplify the desired region in FMOD promoter. Conditions of linear amplification were determined empirically for this primer. The PCR conditions were as follows: 95ºC for 5min; 95ºC for 30 sec, 56ºC for 30 s and 72ºC for 30 s for 35 cycles. PCR products were resolved by electrophoresis on a 2% agarose gel and visualized after ethidium bromide staining. Real time qPCR was performed with the same eluted DNA. The conditions were as follows: 95ºC for 3 min; 95ºC for 10 sec, 56ºC for 30 sec, 72ºC for 30 s for 40 cycles and 72ºC for 5 mins. The Ct values of different conditions were normalized to Ct values in IgG control.

Boyden chamber assay for cell migration

Trans-well assay was done in 24-well Boyden chambers with 8-µm pore size polycarbonate membranes (BD Biosciences, San Diego, USA). ST1 cells (5×10^4) were re-suspended in 500 µl serum-free Medium 199 and placed in the upper chamber, and the lower chamber was filled with serum-free Medium 199 with 750 µl conditioned medium or 400nm final concentration of recombinant protein dissolved in incomplete medium (serving as a chemo-attractant). After 24 hours of incubation, cells remaining on the upper surface of the membrane were removed with a wet cotton bud. The cells that have migrated to the lower surface of the membrane were fixed in ice-cold methanol and stained with crystal violet and imaged in a light microscope.

Boyden chamber assay for cell invasion

Trans-well assay was done in 24-well Boyden chambers with 8-µm pore size polycarbonate membranes coated with Matrigel (BD Biosciences, San Diego, USA). ST1 cells (5×10^4) were re-suspended in 500 µl serum-free Medium 199 and placed in the upper chamber, and the lower chamber was filled with serum-free Medium 199 with 750 µl conditioned medium or 400nm final concentration of recombinant protein dissolved in an incomplete medium (serving as a chemo-attractant). After 24 hours of incubation, cells remaining on the upper surface of the membrane were removed with a wet cotton bud. The cells that have invaded to the lower surface of the membrane were fixed in ice-cold methanol and stained with crystal violet and imaged in a light microscope.

bioRxiv preprint doi: https://doi.org/10.1101/2022.04.03.486893; this version posted April 6, 2022. The copyright holder for this preprint (which was not certified by peer review) is the author/funder, who has granted bioRxiv a license to display the preprint in perpetuity. It is made available under aCC-BY 4.0 International license.

Cell proliferation assay (MTT assay)

1.5 x 10^3 ST1 cells were plated 2% FBS-containing M199 Medium in each well of a 96-well plate. MTT assay was performed as per the established protocol. MTT was added to each well and Formazan crystals formed after 3 hours of incubation were dissolved in DMSO and the absorbance was measured at 420 nm. The first reading served as the untreated condition (0^{th} time-point). After this reading, the cells were treated with 400nm rhFMOD or an equivalent concentration of BSA, and readings were taken every 24 hrs, till 96 hours. The cell viability was then plotted as a line graph.

***In vitro* angiogenesis assay**

ST1 endothelial cells were seeded in 96-well plates (10,000-15,000 cells per well), coated with Geltrex (Invitrogen) and grown in Medium 199 (Sigma) without growth factors. Equal protein amounts (50-100 µg) from serum-free conditioned media from different conditions were added on top of the cells. After 10-12 hours of incubation, endothelial cells form tube-like structures. Each complete circular structure was considered as one complete network and the total number of networks for each condition was counted in a double-blind manner. For positive control, cells are plated in complete endothelial cell media (Medium 199) supplemented with Endothelial Cell Growth Factors (ECGS) and 20% FBS, and in the negative control, cells are plated in incomplete Medium 199 (without serum and ECGS).

Immunofluorescence staining of fixed cells

Cells were plated on coverslips in 12-well plates and allowed to attach. The cells were then fixed with 4% paraformaldehyde and permeabilized using PBS supplemented with 0.25% Triton-X100. Cells were then washed with PBS and blocked using PBS supplemented with 1% BSA, 0.3% Triton X-100 and 5% goat serum for 2 h at room temperature. After blocking, primary antibody, diluted in the blocking buffer, was added to the coverslips overnight at 4°C. Foor dual staining, the primary antibodies (one anti-mouse and the other anti-rabbit) were together added to the samples in the required dilutions. After removal of the primary antibody, cells were thoroughly washed with PBS 3 times for 5 mins each. Fluorescence-conjugated secondary antibody was dissolved in the blocking buffer and added to the cells for 3 h, after which the cells were washed three times with PBS for 5 min. The cells were stained with DAPI (1 µl/ml) for 5 min at room

bioRxiv preprint doi: https://doi.org/10.1101/2022.04.03.486893; this version posted April 6, 2022. The copyright holder for this preprint (which was not certified by peer review) is the author/funder, who has granted bioRxiv a license to display the preprint in perpetuity. It is made available under aCC-BY 4.0 International license.

temperature. Coverslips were mounted on glass slides using glycerol as mounting agent and imaged using a Zeiss LSM 880 confocal microscope.

Luciferase reporter assay

Cells were seeded in a 6-well plates and co-transfected with the reporter luciferase construct and pCMV-beta gal (as control), using lipofectamine according to the manufacturer's instructions. 24-48 h after transfection, cell extracts were made in reporter lysis buffer (Promega). Protein concentrations of the cell lysates were measured by Bradford assay reagent (Bio-Rad). Ten µg protein were mixed with 30 µl of luciferase assay reagent (LAR) to determine the luciferase activity and values were normalized to beta-galactosidase activity units.

Flow cytometry

The GSCs and DGCs are pelleted down and stained with live dead fluorescent stain (L34955 LIVE/DEAD™ Fixable Violet Dead Cell Stain Kit, for 405 nm excitation) for 15 mins at 37 ^{o}C. Then, the cells are blocked using 10% FCS and 1% Sodium Azide in PBS. After blocking, the cells are washed with PBS thrice, incubated with primary antibody for 2 hrs at room temperature, washed again thrice, and incubated with the secondary antibody for 2 hrs in the dark. The final pellet is washed thrice with PBS, dissolved in 200 µl 3% BSA in PBS and analysed using the BD FACS Verse flow cytometer.

RPPA analysis

Untreated ST1 cells and cells treated for 10, 30, and 60 mins with 400 nm rhFMOD were lysed using RPPA lysis buffer. Lysates were serially diluted in 5 two-fold dilutions using lysis buffer and printed on nitrocellulose-coated slides using an Aushon Biosystem 2470 arrayer. Slides were probed with 304 validated primary antibodies followed by detection with appropriate biotinylated secondary antibodies. Slides were scanned, analyzed, and quantified using Array-pro Analyzer software (Media Cybernetics) to generate spot intensity (level 1 data). Signals were visualized by a secondary streptavidin-conjugated HRP antibody and DAB colorimetric reaction. The list of 304 antibodies can be found at the link provided (http://www.mdanderson.org/research/research-resources/core-facilities/functional-proteomics-rppa-core/antibody-information-and-protocol.html).

Cryo-sectioning of fixed mouse brain

bioRxiv preprint doi: https://doi.org/10.1101/2022.04.03.486893; this version posted April 6, 2022. The copyright holder for this preprint (which was not certified by peer review) is the author/funder, who has granted bioRxiv a license to display the preprint in perpetuity. It is made available under aCC-BY 4.0 International license.

Mice were perfused intracardiacally using 4% paraformaldehyde solution and the brains were harvested and stored in PFA for 12 h and subsequently in 30% sucrose solution. The brains were then embedded in Poly-freeze solution (Sigma, #35059990) and sectioned into 20-µm thick sections using a Leica Cryostat. The sections were stored in -80°C in Tissue Cutting Solution (TCS).

IHC of free-floating sections

For immunofluorescence, the brain sections were removed from TCS, put in 96-well plates and washed thoroughly with PBS. Following that, the same protocol was followed for immunofluorescence staining of tissue sections, as that followed for monolayer cells grown on coverslips. At the final step, after adding the secondary antibody, DAPI and PBS washes, the sections were individually mounted on glass slides using the ProLong™ Glass Antifade Mountant (Invitrogen, #P36980) and covered by coverslips. Images were taken using the Zeiss LSM 880 confocal microscope using 10x, 20x, and 40x objectives, for various conditions.

For immunofluorescence of FFPE sections, an extra step of antigen retrieval was performed by de-paraffinizing the sections in xylene, followed by boiling in distilled water twice, for 5 mins each. After this, the rest of the steps (from permeabilization to mounting, the same steps were followed as that of immunofluorescence of free-floating sections.

Scoring methods for confocal images

The areas of the blood vessels and the fluorescence intensities for all the fluorophores used in the tissue sections were measured using the Zeiss black software (https://www.zeiss.com/microscopy/int/products/microscope-software.html), converted to percentages and plotted as bar diagrams. For determining the extent of vascular mimicry in the blood vessels of the tissues, the overlap of green (coming from GFP of the tumor cells) and red (measure of CD31 expression of the endothelial cells) forming yellow color was calculated as a measure of co-localization coefficients in the Zeiss black software. The absolute values of the co-localization coefficients were plotted for each condition.

bioRxiv preprint doi: https://doi.org/10.1101/2022.04.03.486893; this version posted April 6, 2022. The copyright holder for this preprint (which was not certified by peer review) is the author/funder, who has granted bioRxiv a license to display the preprint in perpetuity. It is made available under aCC-BY 4.0 International license.

Subcutaneous injection of DBT-Luc cells for the co-implantation mouse model

All animal procedures followed were approved by the Institute Ethical Committee for Animal Experimentation. Mouse cell line DBT-Luc-DGC, which grows as a monolayer cell line (stable for luciferase expression), were reprogrammed to form DBT-Luc-GSCs. A combination of 10^5 DBT-Luc-GSCs (without any shRNA) and 10^6 DBT-Luc-DGCs that carried either the miRNT or miRFMOD constructs (referred to as DBT-Luc-DGC/miRNT or DBT-Luc-DGC/miRFMOD respectively) were injected subcutaneously in the mice. Two groups of mice (n=5 each) received a combination of 10^5 DBT-Luc-GSCs + 10^6 DBT-Luc-DGC/miRNT and another two groups (n=5 each) received a combination of 10^5 DBT-Luc/GSCs + 10^6 DBT-Luc-DGC/miRFMOD (only one of the two groups for both miRNT and miRFMOD received Doxycycline). Doxycycline injection (intraperitoneal, 100 μg per animal) began on 9th day post the injection and was given on every day up to the 16th day, after which it was given on every alternate day, till the end of the experiment. Since the Doxycycline administration induced the mCherry expression along with the shRNA expression, the animals were imaged for both bioluminescence (marked by red on the timeline) and fluorescence (marked by orange on the timeline) on the days indicated in the timeline. Two other groups (n=5 each) received either only 10^5 DBT-Luc-GSCs or 10^6 DBT-Luc-DGCs (not stables for any shRNA), as controls.

Intra-cranial injection of GBM cells

Cells were harvested in incomplete DMEM or NBM depending on the cell type to be injected. 250,000 DGCs or 100,000 GSCs were injected intracranially (in the hippocampus, 3 mm deep) in each animal using a stereotaxic apparatus. The animals were imaged on the 3rd day after injection and subsequently, every 5 to 6 days until the end of the experiment. In experiments using inducible shRNAs, doxycycline was injected every day for 10 days (from 13th day after injection) and on every alternate day until the end of the experiment. MGG8-GSC (MGG8-GSC/shNT vs. MGG8-GSC/shFMOD), AGR53-GSCs (AGR53-GSC/miRNT vs. AGR53-GSC/miRFMOD), and DBT-Luc-GSCs (DBT-Luc-GSC/miRFMOD) cells were intracranially injected in this study.

bioRxiv preprint doi: https://doi.org/10.1101/2022.04.03.486893; this version posted April 6, 2022. The copyright holder for this preprint (which was not certified by peer review) is the author/funder, who has granted bioRxiv a license to display the preprint in perpetuity. It is made available under aCC-BY 4.0 International license.

In vivo imaging

In vivo imaging was done for bioluminescence or fluorescence with the Perkin Elmer IVIS Spectrum by using mild gas anesthesia (using isoflurane) for the animals.

Hematoxylin and Eosin staining

Brains from perfused mice were paraffin embedded and sectioned using a microtome (5µ sections). Sections were mounted on glass slides and removed from paraffin, rehydrated and stained with Harris Hematoxylin for nuclear staining and Eosin Y solution for cytoplasmic staining. The sections were then mounted using DPX mounting medium and imaged at 0.8X using a Lawrence and Mayo digital microscope.

Gene Set Enrichment Analysis (GSEA)

The differentially expressed genes between the GSC and DGC (as identified in GSE54792) were pre-ranked based on fold change and used as an input to perform GSEA. All the gene sets available in the Molecular Signature Database (MSigDB, roughly 18,000 gene sets) were used to run the GSEA. We filtered out the TGF-beta pathway related gene sets to identify that most of them were significantly enriched in the DGCs over the GSCs. Similarly, the same analysis was carried out in multiple publicly available GBM vs. normal samples datasets to show the significant enrichment of TGF-beta gene sets in GBM over normal. We acknowledge our use of the GSEA software and MSigDB (Subramanian et al., 2005) (http://www.broad.mit.edu/gsea/). SIngle

Single Sample GSEA (ssGSEA)

Gene set variation analysis (gsva) was performed using ssGSEA to determine the enrichment of the different molecular subtypes of GBM in GSE54792 and also the enrichment of the TGF-beta Hallmark gene set from MSigDb. The higher gsva score indicates the highest enrichment which gradually decreases.

Survival analysis

Kaplan-Meier survival analysis was done using GraphPad Prism 5.0 (GraphPad Software, San Diego, California, USA).

Heatmap generation

The heatmaps were generated using the Multiple Experiment Viewer (MEV) software (http://www.tm4.org/mev.html) version 4.8.1. LFQ values for protein expression from mass-spec

bioRxiv preprint doi: https://doi.org/10.1101/2022.04.03.486893; this version posted April 6, 2022. The copyright holder for this preprint (which was not certified by peer review) is the author/funder, who has granted bioRxiv a license to display the preprint in perpetuity. It is made available under aCC-BY 4.0 International license.

data, mean pixel density for the RPPA were used as inputs for Heatmap generation. A non-parametric t-test was performed with a false discovery rate (FDR) and a p-value cut-off of 0.05.

Quantification and Statistical analysis

Bar diagrams are generated using Microsoft excel. The box plots are generated using GraphPad Prism 5.0 (GraphPad Software, San Diego, California, USA). p-value is calculated by unpaired t test with Welch's correction are indicated or student t-test was done using Microsoft Excel. ANOVA p value was calculated using GraphPad Prism 5 software. p value less than 0.05 is considered significant with *, **, *** representing p value less than 0.05, 0.01 and 0.001 respectively. ns stands for non-significant.

List of primer used in this study

1	FMOD	ACCTGCAGCTTGGAGAAGT	CAACACCAACCTGGAGAACC
2	SOX2	AACCCCAAGATGCACAACTC	GCTTAGCCTCGTCGATGAAC
3	SALL2	TAATCTCGGACTGCGAAGGT	TAGAACATGCGTTCTGGTGG
4	POU3F2	TGACGATCTCCACGCAGTAG	GGCAGAAAGCTGTCCAAGTC
5	OLIG2	CCAGAGCCCGATGACCTTTT	AGGACGACTTGAAGCCACTG
6	DLL4	CTGCGAGAAGAAAGTGGACAGG	ACAGTCGCTGACGTGGAGTTCA
7	DLL3	CACTCAACAACCTAAGGACGCAG	GAGCGTAGATGGAAGGAGCAGA
8	JAG1	TGCTACAACCGTGCCAGTGACT	TCAGGTGTGTCGTTGGAAGCCA
9	JAG2	GCTGCTACGACCTGGTCAATGA	AGGTGTAGGCATCGCACTGGAA
10	HES1	GGAAATGACAGTGAAGCACCTCC	GAAGCGGGTCACCTCGTTCATG
11	Mouse FMOD	CCCTTACCCCTATGAGCCC	GACAGTCGCATTCTTGGGGA
12	OSMR	CATCCCGAAGCGAAGTCTTGG	GGCTGGGACAGTCCATTCTAAA
13	ACSBG1	GAACATCTGGTGCACGGTATAG	GAGGAAGCTGGTGGAGTATTG
14	ALDH1L	GAGGAAGCTGGTGGAGTATTG	ACGGTTGGCTGAAAGAAGAA
15	S100B	CCCTGTAGAAGAGTCACCTGTA	GCTGTGGGTCTGTAGATGTATG
16	GFAP	CGGAGACGCATCACCTCTG	AGGGAGTGGAGGAGTCATTCG
17	MELK	TATGAAACGATTGGGACAGGTG	CCCTAGCGCATTCTTATCCATGA
18	NESTIN	GGAATCTCTGAGGTCTCTTGATG	TCTGCTCCTCCTCTTCTACTT
19	BMI1	CAAGAAGAGGTGGAGGGAATAC	CCAGAGAGATGGACTGACAAAT

bioRxiv preprint doi: https://doi.org/10.1101/2022.04.03.486893; this version posted April 6, 2022. The copyright holder for this preprint (which was not certified by peer review) is the author/funder, who has granted bioRxiv a license to display the preprint in perpetuity. It is made available under aCC-BY 4.0 International license.

20	KLF4	GTGCCCCGACTAACCGTTG	GTCGTTGAACTCCTCGGTCT
21	TWIST2	CCAAGGCTCTCAGAACAAGAA	GGAGACGTAAAGAACAGGAGTATG
22	PTGS2	TGAGCAACTATTCCAAACCAGC	GCACGTAGTCTTCGATCACTATC
23	S100A6	ATGGCATGCCCTCTGGATCAG	TTATTTCAGAGCTTCATTGTAGATC
24	Cyclophilin	CAGACGCCACTGTCGCTTT	TGTCTTTGGAACTTTGTCTG
25	ATP5G	CCAGACGGGAGTTCCAGAC	GACGGGTTCCTGGCATAGC
26	GAPDH	TTGTCAAGCTCATTTCCTGG	TGATGGTACATGACAAGGTGC
27	cPPT (for sequencing)	GAAGGAATAGAAGAAGAAGGT GGAGAG	
28	KLF8	CCTGAAAGCTCACCGCAGAATC	TGCTTGCGGAAATGGCGAGTGA
29	FOXP1	CAAAGAACGCCTGCAAGCCATG	GGAGTATGAGGTAAGCTCTGTGG
30	ETS1	GAGTCAACCCAGCCTATCCAGA	GAGCGTCTGATAGGACTCTGTG
31	GATA4	GCGGTGCTTCCAGCAACTCCA	GACATCGCACTGACTGAGAACG
32	ATF2	GGTAGCGGATTGGTTAGGACTC	TGCTCTTCTCCGACGACCACTT
33	ITGB1	GGATTCTCCAGAAGGTGGTTTCG	TGCCACCAAGTTTCCCATCTCC
34	ITGA6	CGAAACCAAGGTTCTGAGCCCA	CTTGGATCTCCACTGAGGCAGT
35	ITGAV	AGGAGAAGGTGCCTACGAAGCT	GCACAGGAAAGTCTTGCTAAGGC

List of shRNAs used in the study (all IDs are of Sigma TRC whole-genome shRNA library)

Sl.no	Gene Name	Clone 1	Clone 2	Clone 3	Clone 4	Clone 5
16	FMOD	TRCN0000153650	TRCN0000156734	TRCN0000152163	TRCN0000153199	TRCN0000151908
17	Mouse FMOD	TRCN0000094246	TRCN0000094245	TRCN0000094248		
18	KLF8	TRCN0000015878	TRCN0000015879	TRCN0000015880	TRCN0000015881	TRCN0000015882
19	JAG1	TRCN0000033439	TRCN0000033440	TRCN0000033441	TRCN0000033442	TRCN0000033443
20	ITGA6	TRCN0000057773	TRCN0000057774	TRCN0000057775	TRCN0000057776	TRCN0000057777
21	ITGB1	TRCN0000275134	TRCN0000275133	TRCN0000275083	TRCN0000275135	TRCN0000275082
22	ITGAV	TRCN0000003238	TRCN0000003239	TRCN0000003240	TRCN0000003241	

List of inhibitors used:

S.No.	Inhibitor Name	Target Molecule	Catalog Number
1	Gamma- secretase inhibitor (GSI)	Gamma Secretase	565750 (Merck)
2	RGD Peptide	Integrins	A5082 (Sigma Aldrich)
3	PP2	Src	P0042 (Sigma Aldrich)
4	PP3	Structural analog to PP2	529574 (Calbiochem)
5	H1152	ROCK1	555550 (Calbiochem)

bioRxiv preprint doi: https://doi.org/10.1101/2022.04.03.486893; this version posted April 6, 2022. The copyright holder for this preprint (which was not certified by peer review) is the author/funder, who has granted bioRxiv a license to display the preprint in perpetuity. It is made available under aCC-BY 4.0 International license.

6	RAC1 inhibitor	RAC1	553502 (Sigma Aldrich)
7	PF573228	FAK	PZ0117 (Sigma Aldrich)
8	SB431542	TGFB RI	616464 (Sigma Aldrich)

Supplemental item titles

1) Supplementary information
2) Supplementary figure legends
3) Supplementary Figures 1-28
4) Supplementary Table S1
5) Supplementary Table S2
6) Supplementary Table S3

References

Angara, K., Borin, T.F., and Arbab, A.S. (2017). Vascular Mimicry: A Novel Neovascularization Mechanism Driving Anti-Angiogenic Therapy (AAT) Resistance in Glioblastoma. Transl Oncol *10*, 650-660. 10.1016/j.tranon.2017.04.007.

Angel, I., Pilo Kerman, O., Rousso-Noori, L., and Friedmann-Morvinski, D. (2020). Tenascin C promotes cancer cell plasticity in mesenchymal glioblastoma. Oncogene *39*, 6990-7004. 10.1038/s41388-020-01506-6.

Auffinger, B., Tobias, A.L., Han, Y., Lee, G., Guo, D., Dey, M., Lesniak, M.S., and Ahmed, A.U. (2014). Conversion of differentiated cancer cells into cancer stem-like cells in a glioblastoma model after primary chemotherapy. Cell Death Differ *21*, 1119-1131. 10.1038/cdd.2014.31.

Bao, S., Wu, Q., Sathornsumetee, S., Hao, Y., Li, Z., Hjelmeland, A.B., Shi, Q., McLendon, R.E., Bigner, D.D., and Rich, J.N. (2006). Stem cell-like glioma cells promote tumor angiogenesis through vascular endothelial growth factor. Cancer Res *66*, 7843-7848. 10.1158/0008-5472.CAN-06-1010.

Bartolini, A., Cardaci, S., Lamba, S., Oddo, D., Marchio, C., Cassoni, P., Amoreo, C.A., Corti, G., Testori, A., Bussolino, F., et al. (2016). BCAM and LAMA5 Mediate the Recognition between Tumor Cells and the Endothelium in the Metastatic Spreading of KRAS-Mutant Colorectal Cancer. Clin Cancer Res *22*, 4923-4933. 10.1158/1078-0432.CCR-15-2664.

Bazzoni, R., and Bentivegna, A. (2019). Role of Notch Signaling Pathway in Glioblastoma Pathogenesis. Cancers (Basel) *11*. 10.3390/cancers11030292.

Calabrese, C., Poppleton, H., Kocak, M., Hogg, T.L., Fuller, C., Hamner, B., Oh, E.Y., Gaber, M.W., Finklestein, D., Allen, M., et al. (2007). A perivascular niche for brain tumor stem cells. Cancer Cell *11*, 69-82. 10.1016/j.ccr.2006.11.020.

Carnero, A., and Lleonart, M. (2016). The hypoxic microenvironment: A determinant of cancer stem cell evolution. Bioessays *38 Suppl 1*, S65-74. 10.1002/bies.201670911.

Dittmer, J., and Leyh, B. (2014). Paracrine effects of stem cells in wound healing and cancer progression (Review). Int J Oncol *44*, 1789-1798. 10.3892/ijo.2014.2385.

Friedmann-Morvinski, D., Bushong, E.A., Ke, E., Soda, Y., Marumoto, T., Singer, O., Ellisman, M.H., and Verma, I.M. (2012). Dedifferentiation of neurons and astrocytes by oncogenes can induce gliomas in mice. Science *338*, 1080-1084. 10.1126/science.1226929.

bioRxiv preprint doi: https://doi.org/10.1101/2022.04.03.486893; this version posted April 6, 2022. The copyright holder for this preprint (which was not certified by peer review) is the author/funder, who has granted bioRxiv a license to display the preprint in perpetuity. It is made available under aCC-BY 4.0 International license.

Friedmann-Morvinski, D., and Verma, I.M. (2014). Dedifferentiation and reprogramming: origins of cancer stem cells. EMBO Rep *15*, 244-253. 10.1002/embr.201338254.

Galli, R., Binda, E., Orfanelli, U., Cipelletti, B., Gritti, A., De Vitis, S., Fiocco, R., Foroni, C., Dimeco, F., and Vescovi, A. (2004). Isolation and characterization of tumorigenic, stem-like neural precursors from human glioblastoma. Cancer Res *64*, 7011-7021. 10.1158/0008-5472.CAN-04-1364.

Gridley, T. (2007). Notch signaling in vascular development and physiology. Development *134*, 2709-2718. 10.1242/dev.004184.

Hambardzumyan, D., and Bergers, G. (2015). Glioblastoma: Defining Tumor Niches. Trends Cancer *1*, 252-265. 10.1016/j.trecan.2015.10.009.

Hardee, M.E., and Zagzag, D. (2012). Mechanisms of glioma-associated neovascularization. Am J Pathol *181*, 1126-1141. 10.1016/j.ajpath.2012.06.030.

Heddleston, J.M., Li, Z., Lathia, J.D., Bao, S., Hjelmeland, A.B., and Rich, J.N. (2010). Hypoxia inducible factors in cancer stem cells. Br J Cancer *102*, 789-795. 10.1038/sj.bjc.6605551.

Huang, W.J., Chen, W.W., and Zhang, X. (2016). Glioblastoma multiforme: Effect of hypoxia and hypoxia inducible factors on therapeutic approaches. Oncol Lett *12*, 2283-2288. 10.3892/ol.2016.4952.

Ignatova, T.N., Kukekov, V.G., Laywell, E.D., Suslov, O.N., Vrionis, F.D., and Steindler, D.A. (2002). Human cortical glial tumors contain neural stem-like cells expressing astroglial and neuronal markers in vitro. Glia *39*, 193-206. 10.1002/glia.10094.

Jeon, H.M., Kim, S.H., Jin, X., Park, J.B., Kim, S.H., Joshi, K., Nakano, I., and Kim, H. (2014). Crosstalk between glioma-initiating cells and endothelial cells drives tumor progression. Cancer Res *74*, 4482-4492. 10.1158/0008-5472.CAN-13-1597.

Jin, X., Jin, X., and Kim, H. (2017). Cancer stem cells and differentiation therapy. Tumour Biol *39*, 1010428317729933. 10.1177/1010428317729933.

Klevebring, D., Rosin, G., Ma, R., Lindberg, J., Czene, K., Kere, J., Fredriksson, I., Bergh, J., and Hartman, J. (2014). Sequencing of breast cancer stem cell populations indicates a dynamic conversion between differentiation states in vivo. Breast Cancer Res *16*, R72. 10.1186/bcr3687.

Kofler, N.M., Shawber, C.J., Kangsamaksin, T., Reed, H.O., Galatioto, J., and Kitajewski, J. (2011). Notch signaling in developmental and tumor angiogenesis. Genes Cancer *2*, 1106-1116. 10.1177/1947601911423030.

Long, N.P., Lee, W.J., Huy, N.T., Lee, S.J., Park, J.H., and Kwon, S.W. (2016). Novel Biomarker Candidates for Colorectal Cancer Metastasis: A Meta-analysis of In Vitro Studies. Cancer Inform *15*, 11-17. 10.4137/CIN.S40301.

Mondal, B., Patil, V., Shwetha, S.D., Sravani, K., Hegde, A.S., Arivazhagan, A., Santosh, V., Kanduri, M., and Somasundaram, K. (2017). Integrative functional genomic analysis identifies epigenetically regulated fibromodulin as an essential gene for glioma cell migration. Oncogene *36*, 71-83. 10.1038/onc.2016.176.

Oldberg, A., Kalamajski, S., Salnikov, A.V., Stuhr, L., Morgelin, M., Reed, R.K., Heldin, N.E., and Rubin, K. (2007). Collagen-binding proteoglycan fibromodulin can determine stroma matrix structure and fluid balance in experimental carcinoma. Proc Natl Acad Sci U S A *104*, 13966-13971. 10.1073/pnas.0702014104.

Olmeda, F., and Ben Amar, M. (2019). Clonal pattern dynamics in tumor: the concept of cancer stem cells. Sci Rep *9*, 15607. 10.1038/s41598-019-51575-1.

Pang, X., Dong, N., and Zheng, Z. (2019). Small Leucine-Rich Proteoglycans in Skin Wound Healing. Front Pharmacol *10*, 1649. 10.3389/fphar.2019.01649.

bioRxiv preprint doi: https://doi.org/10.1101/2022.04.03.486893; this version posted April 6, 2022. The copyright holder for this preprint (which was not certified by peer review) is the author/funder, who has granted bioRxiv a license to display the preprint in perpetuity. It is made available under aCC-BY 4.0 International license.

Phng, L.K., and Gerhardt, H. (2009). Angiogenesis: a team effort coordinated by notch. Dev Cell *16*, 196-208. 10.1016/j.devcel.2009.01.015.

Pine, A.R., Cirigliano, S.M., Nicholson, J.G., Hu, Y., Linkous, A., Miyaguchi, K., Edwards, L., Singhania, R., Schwartz, T.H., Ramakrishna, R., et al. (2020). Tumor Microenvironment Is Critical for the Maintenance of Cellular States Found in Primary Glioblastomas. Cancer Discov *10*, 964-979. 10.1158/2159-8290.CD-20-0057.

Prager, B.C., Bhargava, S., Mahadev, V., Hubert, C.G., and Rich, J.N. (2020). Glioblastoma Stem Cells: Driving Resilience through Chaos. Trends Cancer *6*, 223-235. 10.1016/j.trecan.2020.01.009.

Prager, B.C., Xie, Q., Bao, S., and Rich, J.N. (2019). Cancer Stem Cells: The Architects of the Tumor Ecosystem. Cell Stem Cell *24*, 41-53. 10.1016/j.stem.2018.12.009.

Prasad, P., Mittal, S.A., Chongtham, J., Mohanty, S., and Srivastava, T. (2017). Hypoxia-Mediated Epigenetic Regulation of Stemness in Brain Tumor Cells. Stem Cells *35*, 1468-1478. 10.1002/stem.2621.

Rheinbay, E., Suva, M.L., Gillespie, S.M., Wakimoto, H., Patel, A.P., Shahid, M., Oksuz, O., Rabkin, S.D., Martuza, R.L., Rivera, M.N., et al. (2013). An aberrant transcription factor network essential for Wnt signaling and stem cell maintenance in glioblastoma. Cell Rep *3*, 1567-1579. 10.1016/j.celrep.2013.04.021.

Ricci-Vitiani, L., Pallini, R., Biffoni, M., Todaro, M., Invernici, G., Cenci, T., Maira, G., Parati, E.A., Stassi, G., Larocca, L.M., and De Maria, R. (2010). Tumour vascularization via endothelial differentiation of glioblastoma stem-like cells. Nature *468*, 824-828. 10.1038/nature09557.

Rupp, T., Langlois, B., Koczorowska, M.M., Radwanska, A., Sun, Z., Hussenet, T., Lefebvre, O., Murdamoothoo, D., Arnold, C., Klein, A., et al. (2016). Tenascin-C Orchestrates Glioblastoma Angiogenesis by Modulation of Pro- and Anti-angiogenic Signaling. Cell Rep *17*, 2607-2619. 10.1016/j.celrep.2016.11.012.

Safa, A.R., Saadatzadeh, M.R., Cohen-Gadol, A.A., Pollok, K.E., and Bijangi-Vishehsaraei, K. (2015). Glioblastoma stem cells (GSCs) epigenetic plasticity and interconversion between differentiated non-GSCs and GSCs. Genes Dis *2*, 152-163. 10.1016/j.gendis.2015.02.001.

Short, S.M., Talbott, G.A., and Juliano, R.L. (1998). Integrin-mediated signaling events in human endothelial cells. Mol Biol Cell *9*, 1969-1980. 10.1091/mbc.9.8.1969.

Silva, R., D'Amico, G., Hodivala-Dilke, K.M., and Reynolds, L.E. (2008). Integrins: the keys to unlocking angiogenesis. Arterioscler Thromb Vasc Biol *28*, 1703-1713. 10.1161/ATVBAHA.108.172015.

Singh, S.K., Hawkins, C., Clarke, I.D., Squire, J.A., Bayani, J., Hide, T., Henkelman, R.M., Cusimano, M.D., and Dirks, P.B. (2004). Identification of human brain tumour initiating cells. Nature *432*, 396-401. 10.1038/nature03128.

Soda, Y., Marumoto, T., Friedmann-Morvinski, D., Soda, M., Liu, F., Michiue, H., Pastorino, S., Yang, M., Hoffman, R.M., Kesari, S., and Verma, I.M. (2011). Transdifferentiation of glioblastoma cells into vascular endothelial cells. Proc Natl Acad Sci U S A *108*, 4274-4280. 10.1073/pnas.1016030108.

Stockhausen, M.T., Kristoffersen, K., and Poulsen, H.S. (2010). The functional role of Notch signaling in human gliomas. Neuro Oncol *12*, 199-211. 10.1093/neuonc/nop022.

Suva, M.L., Rheinbay, E., Gillespie, S.M., Patel, A.P., Wakimoto, H., Rabkin, S.D., Riggi, N., Chi, A.S., Cahill, D.P., Nahed, B.V., et al. (2014). Reconstructing and reprogramming the tumor-propagating potential of glioblastoma stem-like cells. Cell *157*, 580-594. 10.1016/j.cell.2014.02.030.

bioRxiv preprint doi: https://doi.org/10.1101/2022.04.03.486893; this version posted April 6, 2022. The copyright holder for this preprint (which was not certified by peer review) is the author/funder, who has granted bioRxiv a license to display the preprint in perpetuity. It is made available under aCC-BY 4.0 International license.

Thouvenot, E., S. Urbach, C. Dantec, J. Poncet, M. Seveno, E. Demettre, P. Jouin, J. Touchon, J. Bockaert and P. Marin (2008). "Enhanced detection of CNS cell secretome in plasma protein-depleted cerebrospinal fluid." J Proteome Res 7(10): 4409-4421.

Tyanova, S., T. Temu, P. Sinitcyn, A. Carlson, M. Y. Hein, T. Geiger, M. Mann and J. Cox (2016). "The Perseus computational platform for comprehensive analysis of (prote)omics data." Nat Methods 13(9): 731-740.

Teodorczyk, M., and Schmidt, M.H.H. (2014). Notching on Cancer's Door: Notch Signaling in Brain Tumors. Front Oncol *4*, 341. 10.3389/fonc.2014.00341.

Wakimoto, H., Kesari, S., Farrell, C.J., Curry, W.T., Jr., Zaupa, C., Aghi, M., Kuroda, T., Stemmer-Rachamimov, A., Shah, K., Liu, T.C., et al. (2009). Human glioblastoma-derived cancer stem cells: establishment of invasive glioma models and treatment with oncolytic herpes simplex virus vectors. Cancer Res *69*, 3472-3481. 10.1158/0008-5472.CAN-08-3886.

Wang, P., Wan, W.W., Xiong, S.L., Feng, H., and Wu, N. (2017). Cancer stem-like cells can be induced through dedifferentiation under hypoxic conditions in glioma, hepatoma and lung cancer. Cell Death Discov *3*, 16105. 10.1038/cddiscovery.2016.105.

Wang, S., Pang, L., Liu, Z., and Meng, X. (2021). SERPINE1 associated with remodeling of the tumor microenvironment in colon cancer progression: a novel therapeutic target. BMC Cancer *21*, 767. 10.1186/s12885-021-08536-7.

Wang, X., Prager, B.C., Wu, Q., Kim, L.J.Y., Gimple, R.C., Shi, Y., Yang, K., Morton, A.R., Zhou, W., Zhu, Z., et al. (2018). Reciprocal Signaling between Glioblastoma Stem Cells and Differentiated Tumor Cells Promotes Malignant Progression. Cell Stem Cell *22*, 514-528 e515. 10.1016/j.stem.2018.03.011.

Winkler, J., Abisoye-Ogunniyan, A., Metcalf, K.J., and Werb, Z. (2020). Concepts of extracellular matrix remodelling in tumour progression and metastasis. Nat Commun *11*, 5120. 10.1038/s41467-020-18794-x.

Yang, L., Shi, P., Zhao, G., Xu, J., Peng, W., Zhang, J., Zhang, G., Wang, X., Dong, Z., Chen, F., and Cui, H. (2020a). Targeting cancer stem cell pathways for cancer therapy. Signal Transduct Target Ther *5*, 8. 10.1038/s41392-020-0110-5.

Yang, X., Wang, S., Yu, W., Zheng, Y., and Wu, Y. (2020b). Inhibition of ITGB1 enhance the anti-tumor effect of cetuximab in colorectal cancer cell. Medicine (Baltimore) *99*, e20944. 10.1097/MD.0000000000020944.

Zhou, D., Alver, B.M., Li, S., Hlady, R.A., Thompson, J.J., Schroeder, M.A., Lee, J.H., Qiu, J., Schwartz, P.H., Sarkaria, J.N., and Robertson, K.D. (2018). Distinctive epigenomes characterize glioma stem cells and their response to differentiation cues. Genome Biol *19*, 43. 10.1186/s13059-018-1420-6.

Zhu, T.S., Costello, M.A., Talsma, C.E., Flack, C.G., Crowley, J.G., Hamm, L.L., He, X., Hervey-Jumper, S.L., Heth, J.A., Muraszko, K.M., et al. (2011). Endothelial cells create a stem cell niche in glioblastoma by providing NOTCH ligands that nurture self-renewal of cancer stem-like cells. Cancer Res *71*, 6061-6072. 10.1158/0008-5472.CAN-10-4269.

Main figures 1 to 7

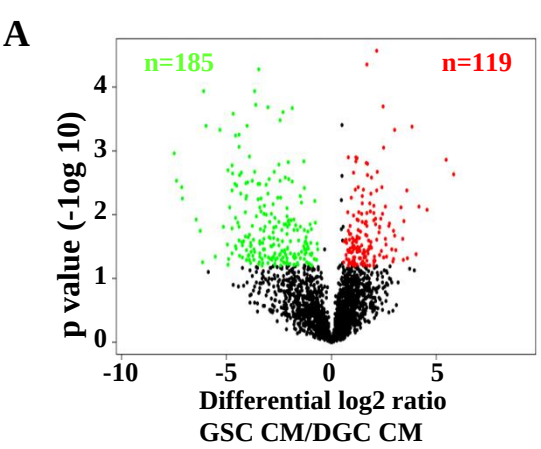

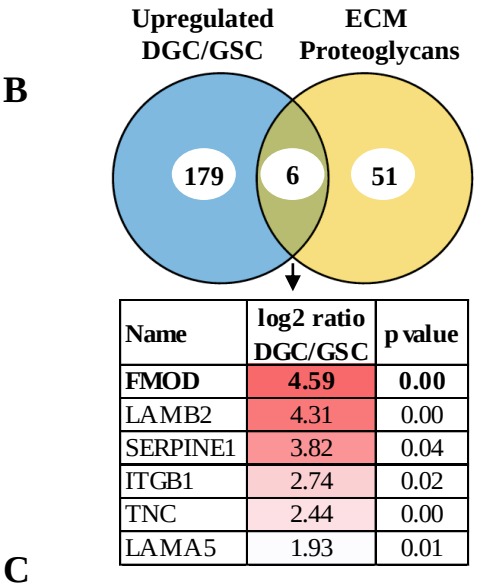

Name	log2 ratio DGC/GSC	p value
FMOD	**4.59**	**0.00**
LAMB2	4.31	0.00
SERPINE1	3.82	0.04
ITGB1	2.74	0.02
TNC	2.44	0.00
LAMA5	1.93	0.01

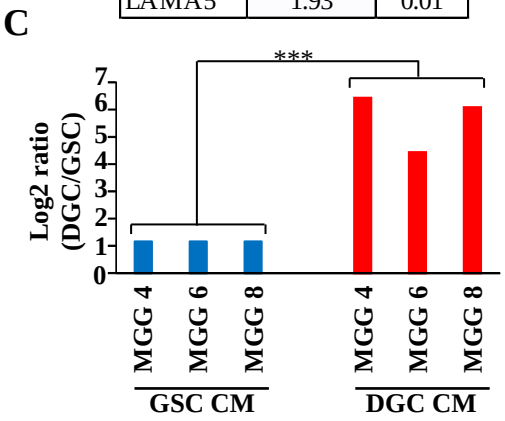

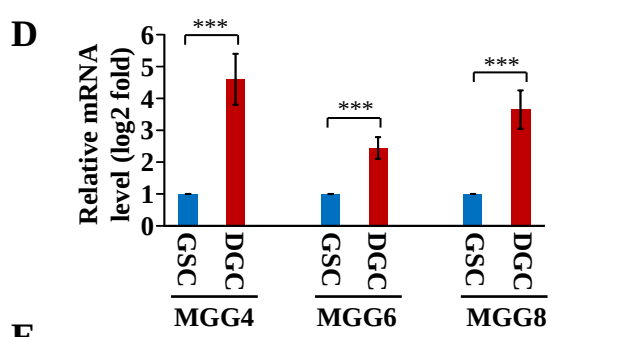

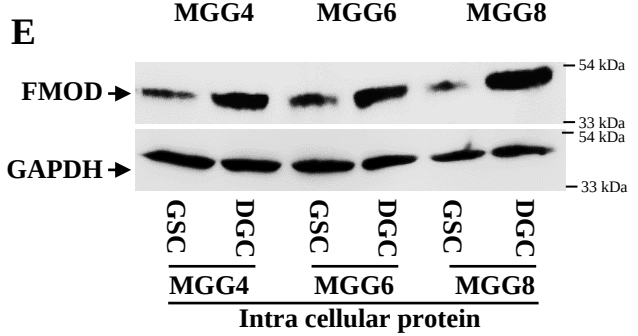

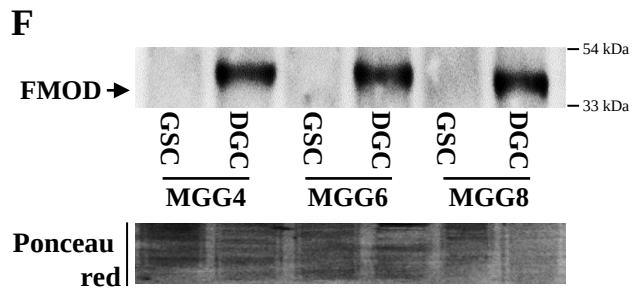

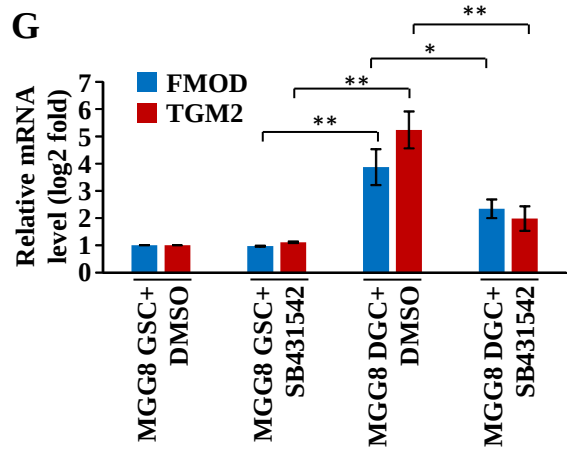

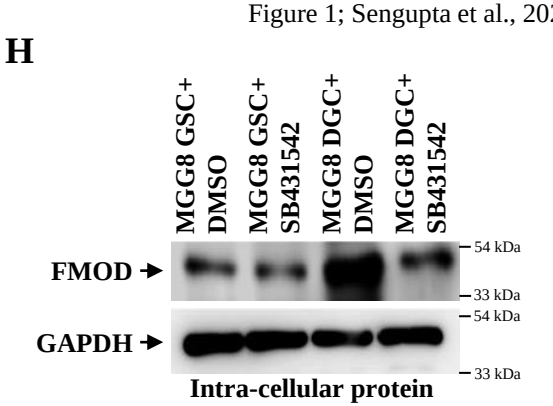

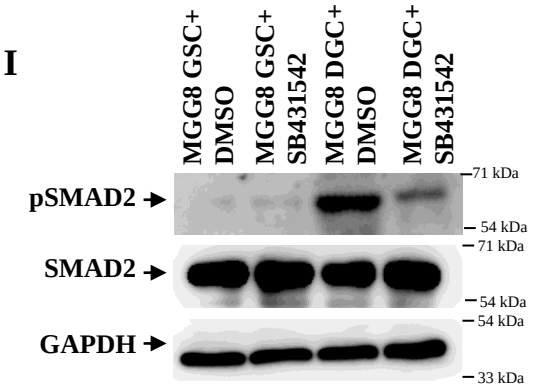

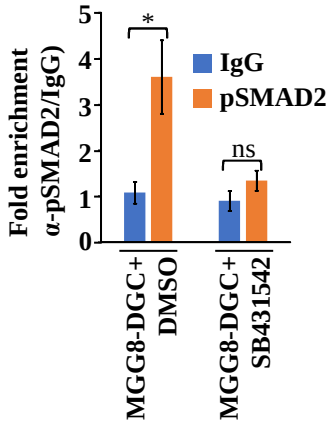

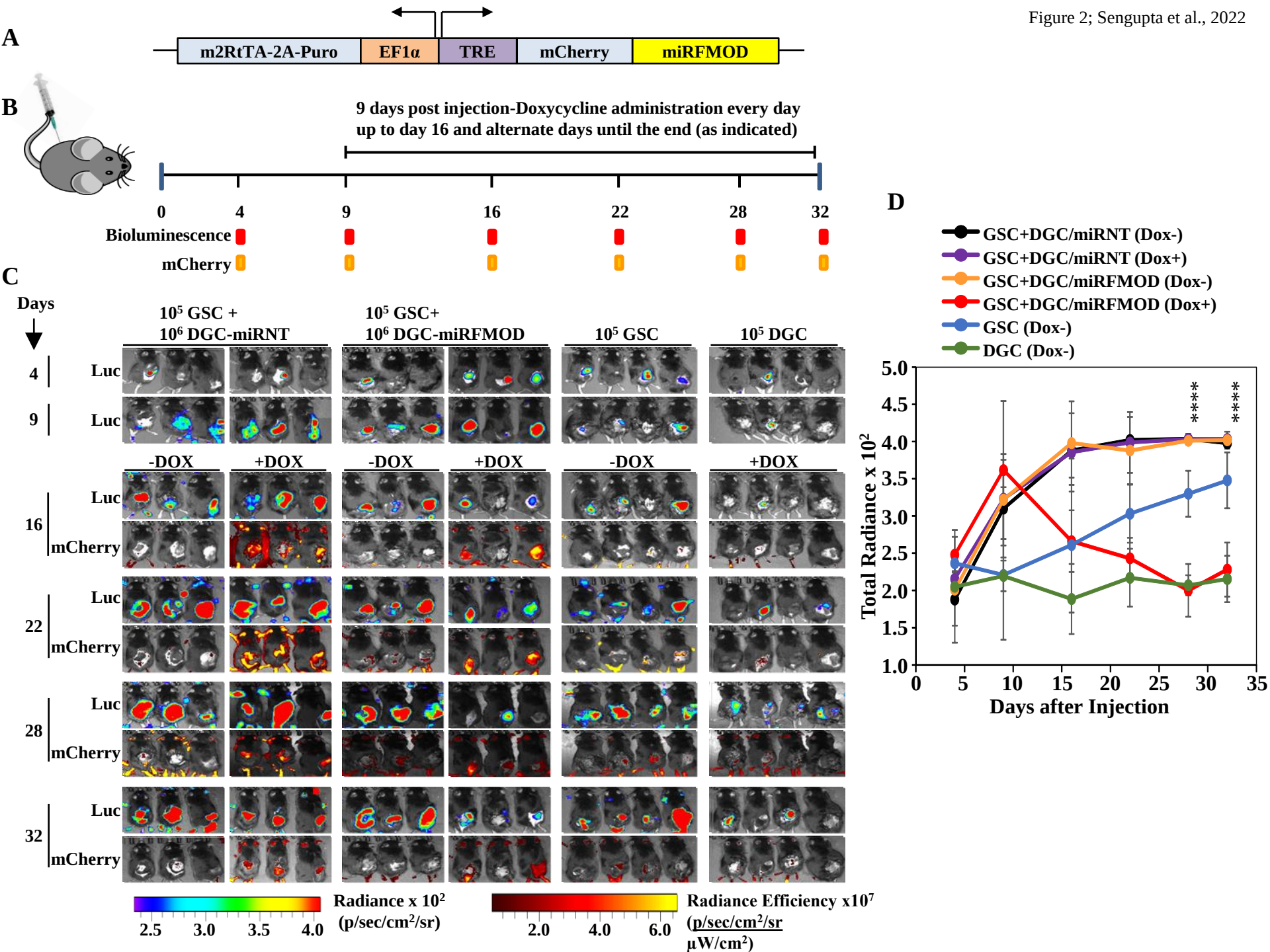
A
m2RtTA-2A-Puro
EF1α
TRE
mCherry
miRFMOD
B
9 days post injection-Doxycycline administration every day
up to day 16 and alternate days until the end (as indicated)
0
4
9
16
22
28
32
Bioluminescence
mCherry
C
Days
10^5 GSC +
10^6 DGC-miRNT
10^5 GSC+
10^6 DGC-miRFMOD
10^5 GSC
10^5 DGC
Luc
mCherry
-DOX
+DOX
Radiance x 10^2
(p/sec/cm^2/sr)
2.5
3.0
3.5
4.0
Radiance Efficiency x10^7
(p/sec/cm^2/sr
μW/cm^2)
2.0
4.0
6.0
D
GSC+DGC/miRNT (Dox-)
GSC+DGC/miRNT (Dox+)
GSC+DGC/miRFMOD (Dox-)
GSC+DGC/miRFMOD (Dox+)
GSC (Dox-)
DGC (Dox-)
Total Radiance x 10^2
Days after Injection
****
****

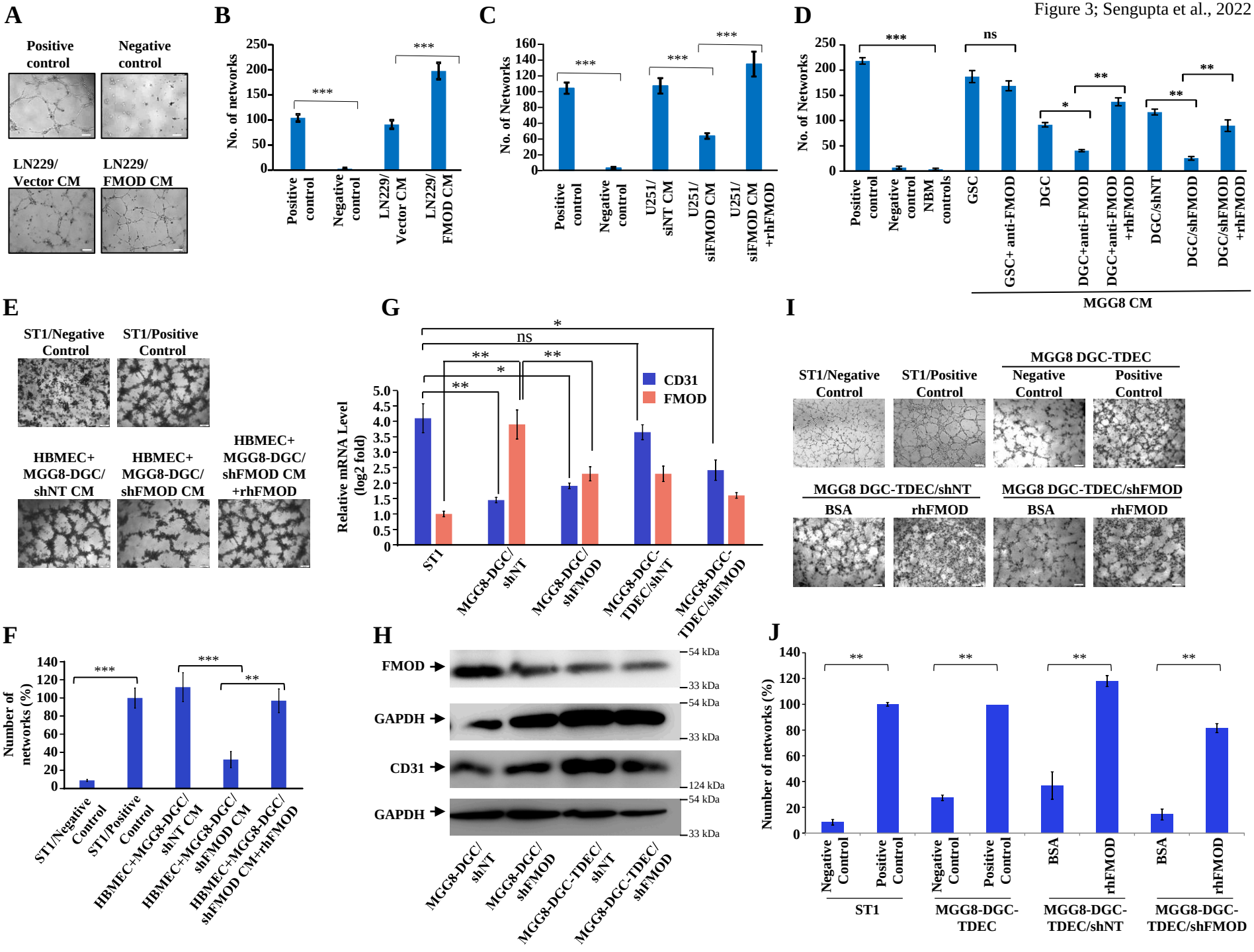
A
Positive control
Negative control
LN229/ Vector CM
LN229/ FMOD CM
B
No. of networks
Positive control
Negative control
LN229/ Vector CM
LN229/ FMOD CM
C
No. of Networks
Positive control
Negative control
U251/ siNT CM
U251/ siFMOD CM
U251/ siFMOD CM +rhFMOD
D
No. of Networks
Positive control
Negative control
NBM controls
GSC
GSC+ anti-FMOD
DGC
DGC+anti-FMOD
DGC+anti-FMOD +rhFMOD
DGC/shNT
DGC/shFMOD
DGC/shFMOD +rhFMOD
MGG8 CM
E
ST1/Negative Control
ST1/Positive Control
HBMEC+ MGG8-DGC/ shNT CM
HBMEC+ MGG8-DGC/ shFMOD CM
HBMEC+ MGG8-DGC/ shFMOD CM +rhFMOD
G
Relative mRNA Level (log2 fold)
CD31
FMOD
ST1
MGG8-DGC/ shNT
MGG8-DGC/ shFMOD
MGG8-DGC-TDEC/shNT
MGG8-DGC-TDEC/shFMOD
I
ST1/Negative Control
ST1/Positive Control
MGG8 DGC-TDEC
Negative Control
Positive Control
MGG8 DGC-TDEC/shNT
BSA
rhFMOD
MGG8 DGC-TDEC/shFMOD
BSA
rhFMOD
F
Number of networks (%)
ST1/Negative Control
ST1/Positive Control
HBMEC+MGG8-DGC/ shNT CM
HBMEC+MGG8-DGC/ shFMOD CM
HBMEC+MGG8-DGC/ shFMOD CM+rhFMOD
H
FMOD
GAPDH
CD31
GAPDH
54 kDa
33 kDa
54 kDa
33 kDa
124 kDa
54 kDa
33 kDa
MGG8-DGC/ shNT
MGG8-DGC/ shFMOD
MGG8-DGC-TDEC/ shNT
MGG8-DGC-TDEC/ shFMOD
J
Number of networks (%)
Negative Control
Positive Control
Negative Control
Positive Control
BSA
rhFMOD
BSA
rhFMOD
ST1
MGG8-DGC-TDEC
MGG8-DGC-TDEC/shNT
MGG8-DGC-TDEC/shFMOD

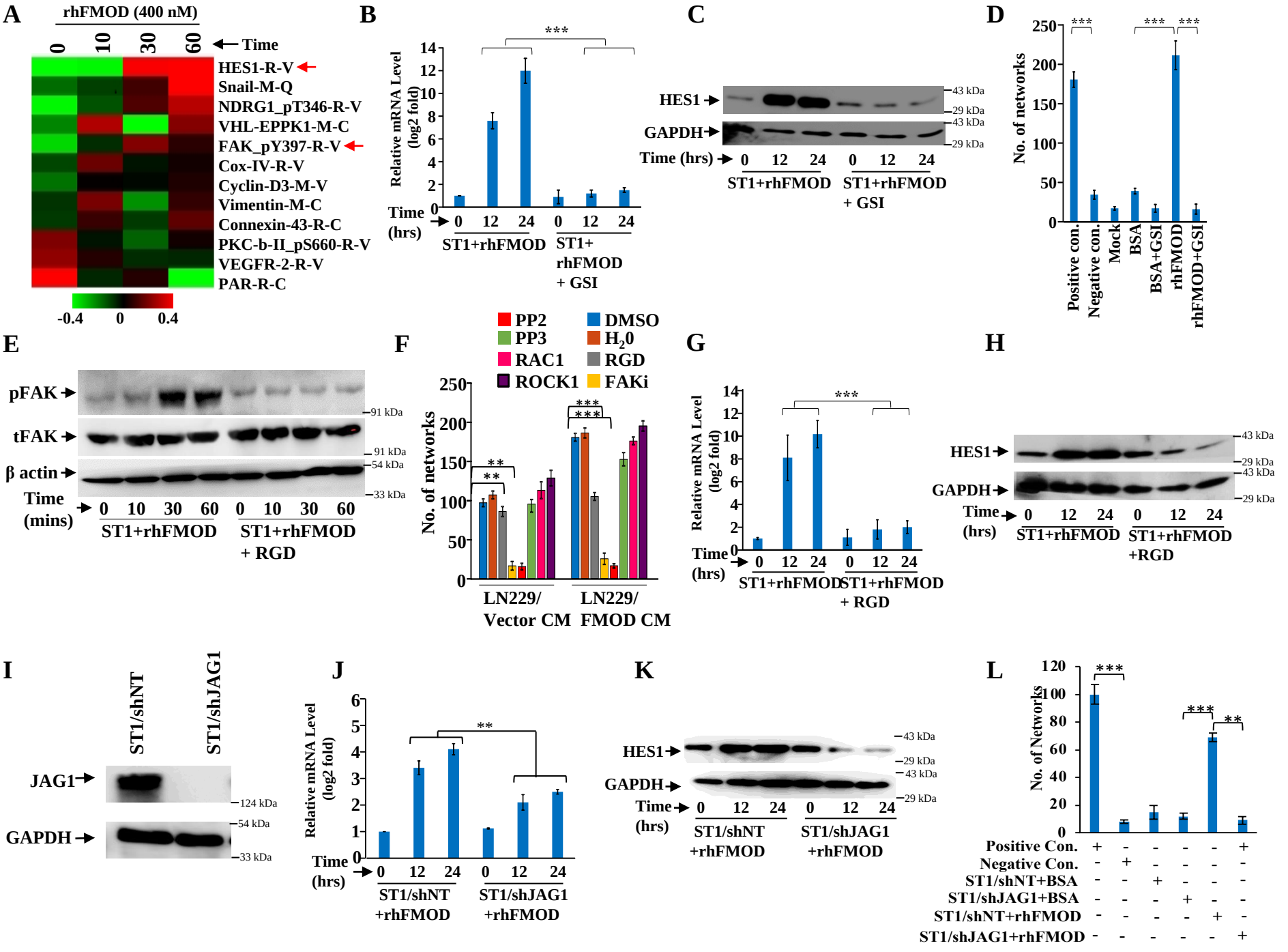
A
rhFMOD (400 nM)
0
10
30
60
Time
HES1-R-V
Snail-M-Q
NDRG1_pT346-R-V
VHL-EPPK1-M-C
FAK_pY397-R-V
Cox-IV-R-V
Cyclin-D3-M-V
Vimentin-M-C
Connexin-43-R-C
PKC-b-II_pS660-R-V
VEGFR-2-R-V
PAR-R-C
-0.4
0
0.4
B
Relative mRNA Level (log2 fold)
Time (hrs)
ST1+rhFMOD
ST1+ rhFMOD + GSI
C
HES1
GAPDH
Time (hrs)
ST1+rhFMOD
ST1+rhFMOD + GSI
43 kDa
29 kDa
D
No. of networks
Positive con.
Negative con.
Mock
BSA
BSA+GSI
rhFMOD
rhFMOD+GSI
E
pFAK
tFAK
β actin
Time (mins)
ST1+rhFMOD
ST1+rhFMOD + RGD
91 kDa
54 kDa
33 kDa
F
PP2
PP3
RAC1
ROCK1
DMSO
H20
RGD
FAKi
No. of networks
LN229/ Vector CM
LN229/ FMOD CM
G
Relative mRNA Level (log2 fold)
Time (hrs)
ST1+rhFMOD
ST1+rhFMOD + RGD
H
HES1
GAPDH
Time (hrs)
ST1+rhFMOD
ST1+rhFMOD +RGD
I
ST1/shNT
ST1/shJAG1
JAG1
GAPDH
124 kDa
54 kDa
33 kDa
J
Relative mRNA Level (log2 fold)
Time (hrs)
ST1/shNT +rhFMOD
ST1/shJAG1 +rhFMOD
K
HES1
GAPDH
Time (hrs)
ST1/shNT +rhFMOD
ST1/shJAG1 +rhFMOD
L
No. of Networks
Positive Con.
Negative Con.
ST1/shNT+BSA
ST1/shJAG1+BSA
ST1/shNT+rhFMOD
ST1/shJAG1+rhFMOD

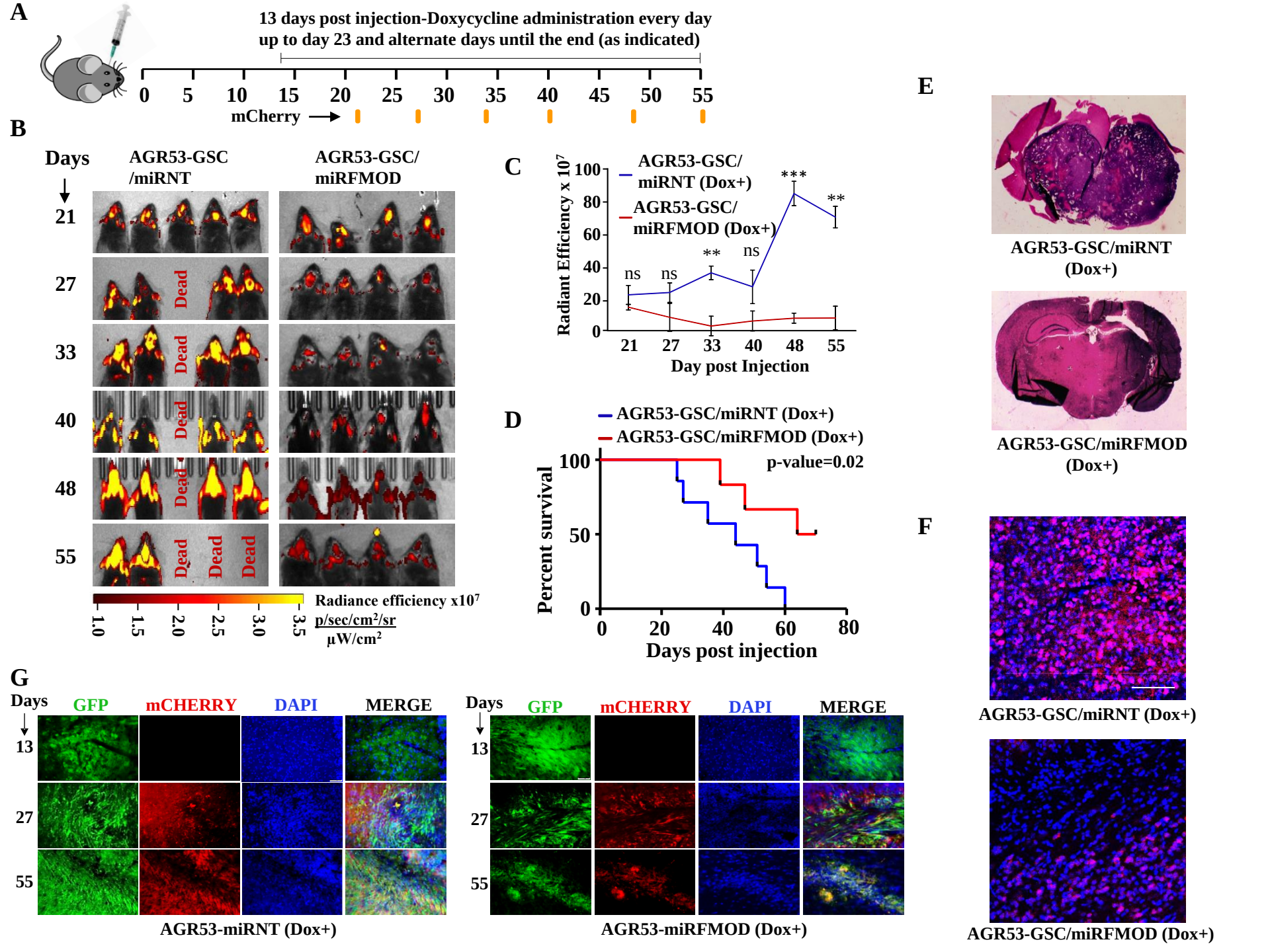
A
13 days post injection-Doxycycline administration every day
up to day 23 and alternate days until the end (as indicated)
0 5 10 15 20 25 30 35 40 45 50 55
mCherry
B
Days
AGR53-GSC /miRNT
AGR53-GSC/ miRFMOD
21
27
33
40
48
55
Dead
Radiance efficiency x10^7
p/sec/cm²/sr
µW/cm²
1.0 1.5 2.0 2.5 3.0 3.5
C
AGR53-GSC/ miRNT (Dox+)
AGR53-GSC/ miRFMOD (Dox+)
Radiant Efficiency x 10^7
ns ns ** ns *** **
Day post Injection
D
AGR53-GSC/miRNT (Dox+)
AGR53-GSC/miRFMOD (Dox+)
p-value=0.02
Percent survival
Days post injection
E
AGR53-GSC/miRNT (Dox+)
AGR53-GSC/miRFMOD (Dox+)
F
AGR53-GSC/miRNT (Dox+)
AGR53-GSC/miRFMOD (Dox+)
G
Days
GFP
mCHERRY
DAPI
MERGE
13
27
55
AGR53-miRNT (Dox+)
AGR53-miRFMOD (Dox+)

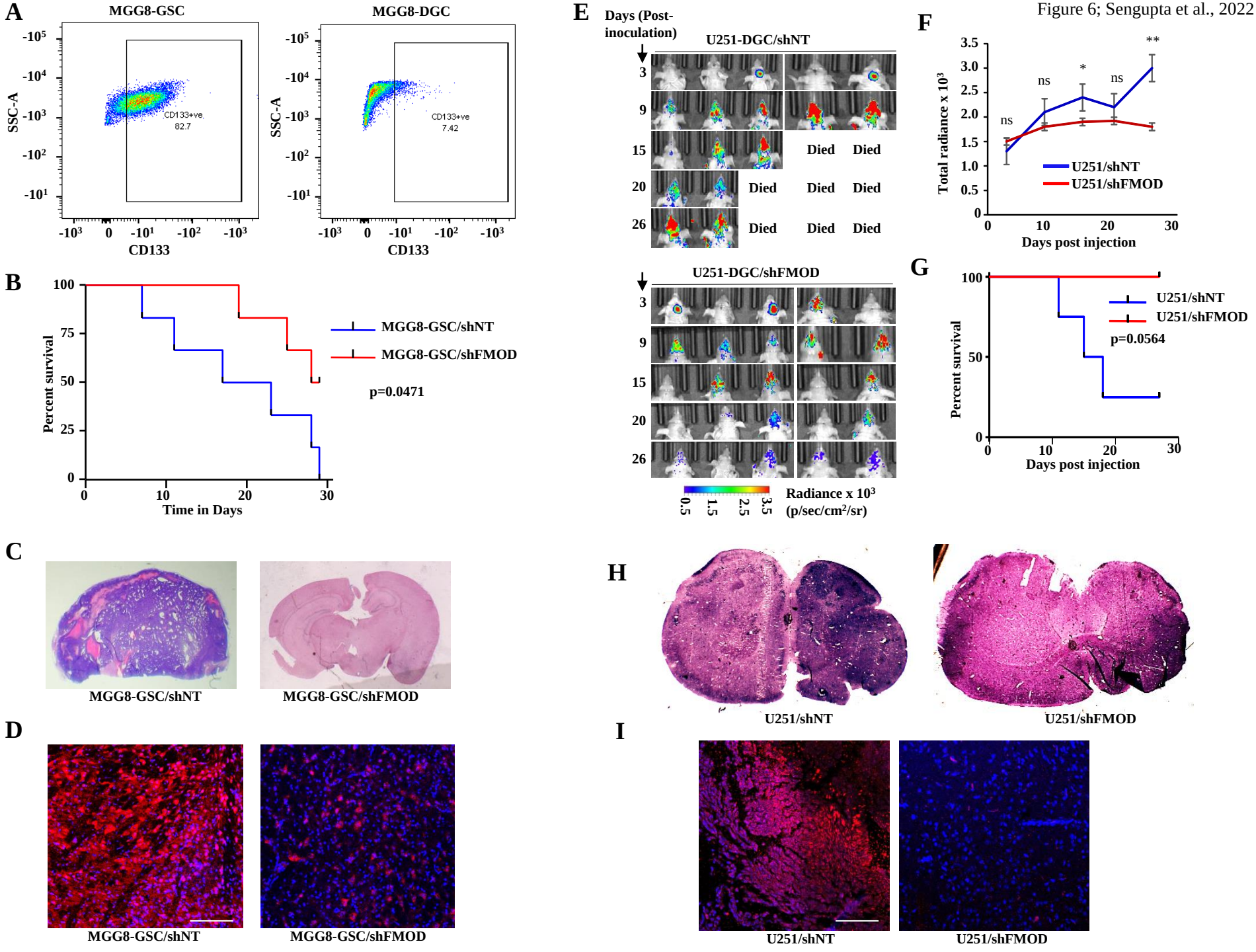
A
MGG8-GSC
MGG8-DGC
SSC-A
CD133
CD133+ve
82.7
CD133+ve
7.42
B
Percent survival
Time in Days
MGG8-GSC/shNT
MGG8-GSC/shFMOD
p=0.0471
C
MGG8-GSC/shNT
MGG8-GSC/shFMOD
D
MGG8-GSC/shNT
MGG8-GSC/shFMOD
E
Days (Post-inoculation)
U251-DGC/shNT
U251-DGC/shFMOD
Died
Radiance x 10³ (p/sec/cm²/sr)
F
Total radiance x 10³
Days post injection
U251/shNT
U251/shFMOD
ns
*
**
G
Percent survival
Days post injection
U251/shNT
U251/shFMOD
p=0.0564
H
U251/shNT
U251/shFMOD
I
U251/shNT
U251/shFMOD

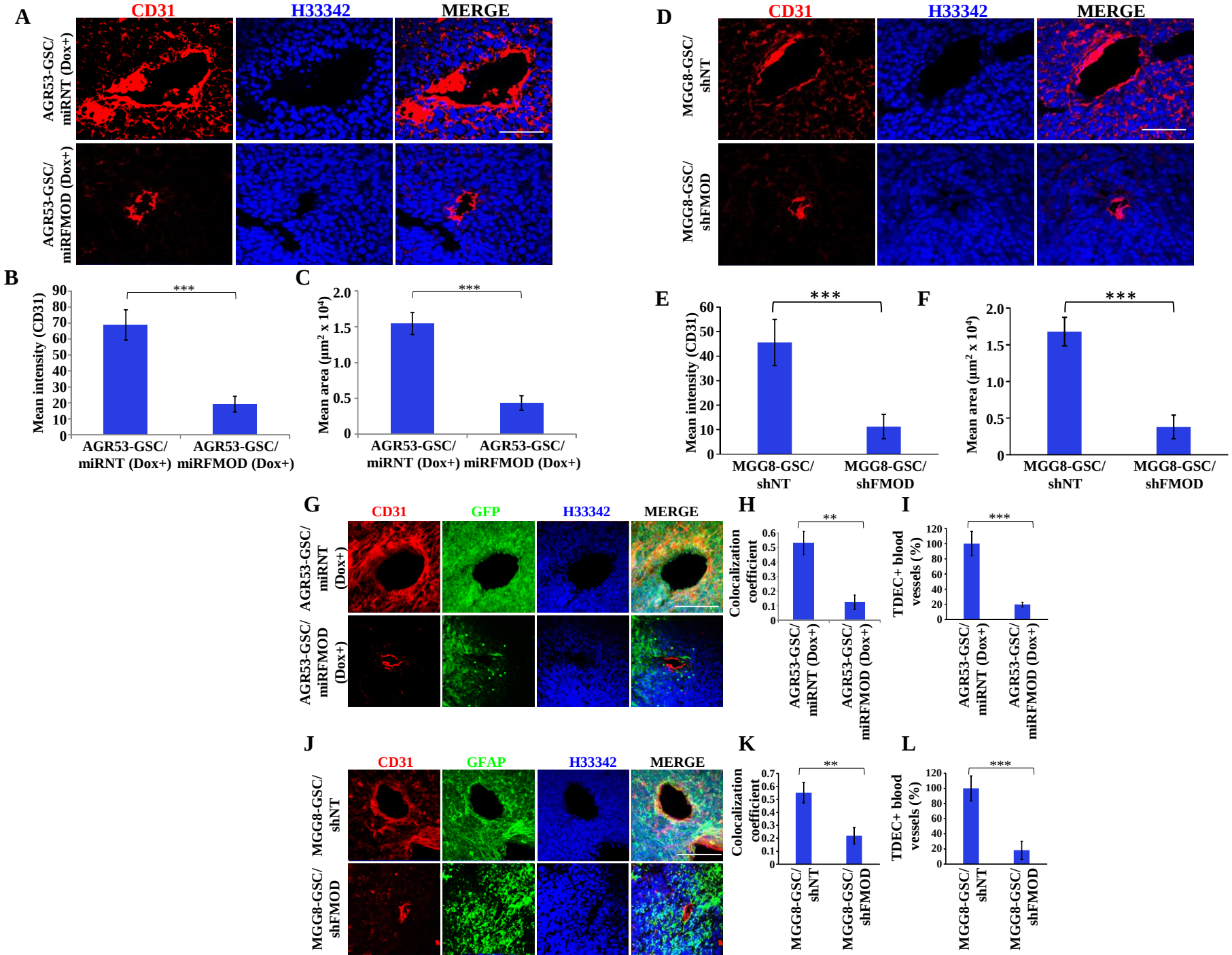
A
CD31
H33342
MERGE
AGR53-GSC/ miRNT (Dox+)
AGR53-GSC/ miRFMOD (Dox+)
D
MGG8-GSC/ shNT
MGG8-GSC/ shFMOD
B
Mean intensity (CD31)
***
AGR53-GSC/ miRNT (Dox+)
AGR53-GSC/ miRFMOD (Dox+)
C
Mean area (μm² x 10⁴)
E
MGG8-GSC/ shNT
MGG8-GSC/ shFMOD
F
G
GFP
AGR53-GSC/ miRNT (Dox+)
AGR53-GSC/ miRFMOD (Dox+)
H
Colocalization coefficient
**
I
TDEC+ blood vessels (%)
J
GFAP
K
L

bioRxiv preprint doi: https://doi.org/10.1101/2022.04.03.486893; this version posted April 6, 2022. The copyright holder for this preprint (which was not certified by peer review) is the author/funder, who has granted bioRxiv a license to display the preprint in perpetuity. It is made available under aCC-BY 4.0 International license.

Supplementary information

The role of FMOD on GSC, DGC growth, and their plasticity *in vitro*

Before studying the importance of DGC secreted FMOD on tumor growth, we decided to investigate its requirement for the GSC, DGC growth, and their plasticity to form the other type. We have earlier shown that FMOD is not required for the proliferation of established glioma cell lines **(Mondal et al., 2017).** We used two human glioma cell lines- MGG8 and U251, two murine glioma cell lines-AGR53 (***Angel et al., 2020***), and DBT-Luc (**Yun et al., 2007**).

MGG8 GSCs transduced with a small hairpin RNA targeting FMOD (MGG8 GSC/shFMOD) grew as neurospheres with equal efficiency as measured by neurosphere formation and limiting dilution assays and also differentiated to form DGCs as efficiently as control MGG8 GSCs transduced with non-targeting shRNA (MGG8 GSC/shNT) (**Supplementary figure 6A, B, C and D).** As expected, the differentiation was accompanied by the downregulation of glioma reprogramming factors in both MGG8 GSC/shNT and MGG8 GSC/shFMOD cells (**Supplementary figure 6E)**. Concordance with human GSCs, we found a higher expression of FMOD in AGR53-DGCs than AGR53-GSCs. (**Supplementary figures 7A, B, and C**). To silence the expression of FMOD in AGR53-DGC, we used a doxycycline-inducible FMOD shRNA (miRFMOD) construct that contains an inducible mCherry-shRNA cassette downstream of the Tet-responsive element (***Angel et al., 2020***; **Figure 2A**). Efficient silencing of FMOD in doxycycline-treated AGR53-DGC/miRFMOD cells was observed compared to AGR53-DGC/miRNT cells (**Supplementary figure 7D and E).** Next, we investigated the impact of FMOD silencing on AGR53-GSC growth and differentiation to DGCs *in vitro*. Like human GSCs, AGR53-GSC/miRNT and AGR53-GSC/miRFMOD grew as neurospheres with equal efficiency both in the absence and presence of doxycycline (**Supplementary figure 8A).** Further, both AGR53-GSC/miRNT and AGR53-GSC/miRFMOD differentiated efficiently to grow as a monolayer (**Supplementary figure 8C**). The differentiation resulted in the significant upregulation of astrocytic markers (**Supplementary figures 8D**). These results confirm that FMOD is overexpressed in both human and murine DGCs but is not required for GSC growth and their differentiation to DGCs.

bioRxiv preprint doi: https://doi.org/10.1101/2022.04.03.486893; this version posted April 6, 2022. The copyright holder for this preprint (which was not certified by peer review) is the author/funder, who has granted bioRxiv a license to display the preprint in perpetuity. It is made available under aCC-BY 4.0 International license.

To study the role of FMOD on reprogramming of DGCs to form GSCs, AGR53-DGC and DBT-Luc DGC were tested for their ability to reprogram. DBT-Luc is a luciferase-expressing glioblastoma-derived cell line, which grows as a differentiated monolayer (referred here onward as DBT-Luc-DGC) in FBS containing medium (**37**). AGR53-DGC/miRNT and AGR53-DGC/miRFMOD (both in the absence and presence of doxycycline) cells grow as a monolayer efficiently and reprogrammed to form neurospheres (**Supplementary figure 9A**). The reprogramming resulted in the significant upregulation of stem cell markers (**Supplementary figures 9B**). Similarly, DBT-Luc-DGC could readily reprogram to form DBT-Luc neurospheres (DBT-Luc-GSC; data not shown) with concomitant upregulation of stem cell markers and downregulation of astrocyte markers (**Supplementary figure 10A and B**). DBT-Luc-DGCs expressed higher levels of FMOD transcript and protein compared to DBT-Luc-GSCs (**Supplementary figure 10C and D, respectively**). To silence the expression of FMOD in DBT-Luc-DGC, we used the doxycycline-inducible shFMOD (miRFMOD) construct as explained above (***Angel et al., 2020***; **Figure 2A**). The addition of doxycycline resulted in downregulation of FMOD transcript and protein in DBT-Luc-DGC/miRFMOD but not in DBT-Luc-DGC/miRNT cells (**Supplementary figure 10E and F).** As expected, both DBT-Luc-DGC/miRFMOD and DBT-Luc-DGC/miRNT cells showed mCherry expression after doxycycline treatment (**Supplementary figure 10G).** Both DBT-Luc-DGC/miRNT and DBT-Luc-DGC/miRFMOD (both in the absence and presence of doxycycline) cells reprogrammed to form neurospheres with equal efficiency (data not shown). We next explored the impact of FMOD silencing on the ability of U251 cells, an established human glioma cell line, to form neurospheres through reprogramming. U251 cells, which grow as differentiated monolayer cells (referred here as U251-DGC) in an FBS-containing medium, can reprogram and form neurospheres enriched in CD133 expression (***Tao et al., 2018***). Both U251-DGC/shNT and U251-DGC/shFMOD cells could reprogram with equal efficiency, as measured by neurosphere formation and limiting dilution assays (**Supplementary figure 11A, B, and C**). The neurospheres formed through reprogramming showed an upregulation of glioma reprogramming factors in U251-GSC/shNT and U251-GSC/shFMOD cells (**Supplementary figure 11D**). Collectively, these observations indicate that FMOD is not required for GSC or DGC growth and differentiation or reprogramming processes.

bioRxiv preprint doi: https://doi.org/10.1101/2022.04.03.486893; this version posted April 6, 2022. The copyright holder for this preprint (which was not certified by peer review) is the author/funder, who has granted bioRxiv a license to display the preprint in perpetuity. It is made available under aCC-BY 4.0 International license.

Bioinformatics analysis of FMOD, HES1, and JAG1 transcript levels in GBM– classification, coorelation, and prognosis.

The transcript data of FMOD, HES1, and JAG1 in different data sets were used for deriving 1) transcriptional upregulation in GBM over control brain, 2) survival prediction by Kaplan meier analysis, and 3) coorelation between transcripts (**see Table below more detail**). We used a total of 1885 samples that included GBMs (n=1833) and control brain samples (n=52). Whereever, the data is not available (NA), the specific analysis is not carried out. A p value less than 0.05 is considered significant with **** as less than 0.0001, *** as less than 0.001, ** as less than 0.01 and * as less than 0.05. The non significant data is denoted as "ns". The data is shown in Supplementary Figure 21 and 22.

S. No	Dataset	Source	Control	Survival Information	Control brain (n)	GBM samples (n)	FMOD: GBM vs Control		HES1: GBM vs Control		JAG1: GBM vs Control		FMOD survival Kaplan -Meier		FMOD to HES1 correlation		FMOD to JAG1 correlation	
							log2 fold change	p value	log2 fold change	p value	log2 fold chang	p value	Hazard Ratio	Low vs High p value	R value	p value	R value	p value
1	TCGA Affymetrix	TCGA	Yes	Yes	10	528	6.87	< 0.000	8.98	< 0.000	8.64	< 0.000	1.40	0.00	0.30	< 0.0001	0.08	0.08
2	TCGA Agilent	TCGA	Yes	Yes	10	489	1.42	0.00	0.98	< 0.000	2.04	< 0.000	1.34	0.00	0.36	< 0.0001	0.17	0.00
3	Gravendeel	GSE16011	Yes	Yes	8	159	1.90	0.00	1.42	0.00	1.84	< 0.000	2.01	< 0.0001	0.35	< 0.0001	0.12	0.15
4	TCGA RNA Seq	TCGA	Yes	Yes	4	156	2.91	0.00	1.01	0.01	2.32	< 0.000	1.31	0.13	0.22	0.01	0.05	0.58
5	CGGA RNA Seq	CGGA	Yes	Yes	20	105	12.94	0.01	9.62	0.01	NA		2.25	0.00	0.06	0.58	NA	
6	Lee Y	GSE13041	No	Yes	NA	191	NA						1.46	0.01	0.36	< 0.0001	0.29	< 0.0001
7	Oh	GSE58401	No	No	NA	105							NA		0.33	0.00	0.25	0.01
8	Bao	GSE48865	No	No	NA	100									0.57	< 0.0001	0.25	0.01

For survival prediction based on the methylation status of FMOD promoter, the samples were divided into methylation high (above median β value) and low (below median β value) for two CpG IDs- cg03764585 and cg04704856, derived from TCGA and GSE48461 data sets. The data is presented in Supplementary Figure 22.

Investigating Integrin heterodimeric subunits that are required in rhFMOD treated endothelial cells.

Integrins are a family of α/β heterodimeric transmembrane adhesion receptors. To identify the integrin α and β subunits that are involved in rhFMOD activation of integrin signaling in endothelial cells, we resorted to an unbiased approach where we analyzed the transcriptome data of microvessels isolated through laser capture microdissection (LCM) from human brain samples (**Song et al., 2020, 10: 12358, Scientific Reports**). The transcript abundance of all integrins subunits (α subunits (n=19) and β subunits (n=13) are shown in the table below. Three integrin

bioRxiv preprint doi: https://doi.org/10.1101/2022.04.03.486893; this version posted April 6, 2022. The copyright holder for this preprint (which was not certified by peer review) is the author/funder, who has granted bioRxiv a license to display the preprint in perpetuity. It is made available under aCC-BY 4.0 International license.

subunits with maximum transcript abundance – ITGA6, ITGB1, and ITGAV, were chosen for testing. The ability of rhFMOD to induce pFAK levels in ST1 cells silenced for any of the above three integrins was investigated. The results show that all three integrins are essential for rhFMOD activation of integrin signaling in endothelial cells (**Supplementary figure 18**).

High abundant integrins in endothelail cells[$]					
S. No.	**Integrins**	**Microvessels 1**	**Microvessels 2**	**Microvessels 3**	**Average**
		FPKM (log2)			**FPKM (log2)**
1	**ITGA6**	191	68	249	169
2	**ITGB1**	78	26	151	85
3	**ITGAV**	57	91	61	70
4	ITGA7	23	28	76	42
5	ITGA1	30	4	79	38
6	ITGB8	19	41	15	25
7	ITGB5	39	9	21	23
8	ITGA5	13	11	38	20
9	ITGA10	11	9	40	20
10	ITGB1BP1	16	7	26	16
11	ITGA3	1	15	12	9
12	ITGA2	11	4	8	8
13	ITGA9	0	18	4	7
14	ITGB2	12	6	2	7
15	ITGB4	0	6	13	7
16	ITGB3BP	2	0	16	6
17	ITGAE	5	1	6	4
18	ITGB7	0	0	11	4
19	ITGB3	6	0	3	3
20	ITGA4	7	0	0	2
21	ITGAL	1	0	5	2
22	ITGA8	0	1	4	2
23	ITGAX	4	0	0	1
24	ITGAM	2	0	0	1
25	ITGA11	1	0	0	0
26	ITGB1BP2	0	0	1	0
27	ITGA2B	0	0	0	0
28	ITGBL1	0	0	0	0
29	ITGA9-AS1	0	0	0	0
30	ITGAD	0	0	0	0
31	ITGB2-AS1	0	0	0	0
32	ITGB6	0	0	0	0

bioRxiv preprint doi: https://doi.org/10.1101/2022.04.03.486893; this version posted April 6, 2022. The copyright holder for this preprint (which was not certified by peer review) is the author/funder, who has granted bioRxiv a license to display the preprint in perpetuity. It is made available under aCC-BY 4.0 International license.

Supplementary figure legends

Supplementary Figure 1: Gene ontology analysis of differentially abundant proteins in GSC and DGC CMs. A. Gene Ontology (GO) analysis of proteins exhibiting higher abundance in the GSC CM. **B.** Gene Ontology (GO) analysis of proteins exhibiting higher abundance in DGC CM. Enrichment factor is calculated by-log (q-value). The q-value is a modified Fisher exact p-value provided by the Uniprot Database for annotation, visualization, and integrated discovery enrichment analysis.

Supplementary Figure 2: TGF-β pathway is activated in DGCs over GSCs. A. Gene Set Enrichment Analysis (GSEA) shows a negative enrichment of multiple TGF-β-related gene sets in GSCs over DGCs, suggesting an activated TGF-β signaling in the DGCs. All these gene sets have positive normalized enrichment score (NES) and significant FDR q-value and p value.

Supplementary Figure 3: TGF-β is activated in GBM over normal samples in multiple datasets. Gene Set Enrichment Analysis (GSEA) shows the positive enrichment of multiple TGF-β-related gene sets in GBM over normal in multiple publicly available datasets and darker to lighter red indicates highest to lowest normalized enrichment score (NES), while % and green indicates the significant gene sets. p value less than 0.05 is considered significant. NA indicates Not Available.

Supplementary Figure 4: Mesenchymal gene expression signature and TGF-β signaling pathway are enriched in DGCs. Table indicating the subtypes of MGG4, MGG6, and MGG8 GSCs vs. DGCs (each in triplicates). The darkest red indicates the highest value for a subtype that is most enriched in that particular sample, with decreasing color intensity indicating the other lesser enriched subtypes in a gradual manner. The Table also indicates the enrichment of the TGF-β hallmark gene set from MSigDb. The intensity of the red color indicates the varying enrichment scores, with darkest red depicting highest enrichment and gradual lighter colors indicating gradually decreasing enrichment scores.

Supplementary Figure 5: FMOD expression and TGF-β signaling activation are significantly higher in mesenchymal GBM over the other subtypes. A. Box plots depicting significantly higher expression of FMOD in mesenchymal GBM samples over the other subtypes

bioRxiv preprint doi: https://doi.org/10.1101/2022.04.03.486893; this version posted April 6, 2022. The copyright holder for this preprint (which was not certified by peer review) is the author/funder, who has granted bioRxiv a license to display the preprint in perpetuity. It is made available under aCC-BY 4.0 International license.

in the TCGA Agilent dataset. **B.** Box plots depicting significantly higher enrichment of the TGF-β hallmark gene set from MSigDb in mesenchymal GBM samples over the other subtypes in the TCGA Agilent dataset. **** indicates the ANOVA p value for **A** and **B**. **C.** Bar diagram showing increased SBE-Luc activity indicating activated TGF-β pathway in MGG8-DGCs, that is inhibited upon TGF-β inhibitor treatment. **D.** Bar diagram showing increased FMOD promoter Luc activity in MGG8-DGCs, that is inhibited upon TGF-β inhibitor treatment. p-value is calculated by unpaired t-test with Welch's correction are indicated. P-value less than 0.05 is considered significant with *, **, *** representing p-value less than 0.05, 0.01 and 0.001 respectively.

Supplementary Figure 6: FMOD does not play a role in GSC neurosphere formation/maintenance and differentiation in human GSCs A. Western blotting showing silencing of FMOD in MGG8-GSCs. **B.** Bar diagram, quantifying number of spheres, shows no significant difference in sphere formation of MGG8 GSCs between shNT and shFMOD conditions (spheres are divided into different sizes, 50-200μm2, 200-440μm2, and 400-800μm2). **C.** Limiting dilution assay shows no significant decrease (p=0.92) in the sphere-forming capacity of MGG8 GSCs between MGG8-GSC/shNT (black line) and MGG8-GSC/shFMOD (red line) conditions. **D.** Representative images showing MGG8-GSCs showing no difference in sphere formation and differentiation between shNT and shFMOD conditions. Magnification,=4X, Scale=200 μm **E.** Real-time qPCR analysis shows that the four GSC reprogramming factors (OLIG2, SOX2, POU3F2, and SALL2) have similar less expression in both MGG8-DGC/shNT and MGG8-DGC/shFMOD (depicted by solid blue and solid red respectively), but undergo an expected similar significant increase in MGG8-GSC/shNT and MGG8-GSC/shFMOD cells (depicted by striped blue and striped red bars respectively). p values calculated by unpaired t test with Welch's correction are indicated. p value less than 0.05 is considered significant with *, **, *** representing p value less than 0.05, 0.01 and 0.001 respectively. ns stands for non-significant.

Supplementary Figure 7: Difference in the level of FMOD expression between GSC and DGC of mouse glioma cell line AGR53 and confirmation of efficient conditional knockdown. A. Real time qRT-PCR analysis showing significantly higher FMOD expression in AGR53-DGCs, compared with AGR53-GSCs. **B.** Western blotting showing FMOD is expressed

bioRxiv preprint doi: https://doi.org/10.1101/2022.04.03.486893; this version posted April 6, 2022. The copyright holder for this preprint (which was not certified by peer review) is the author/funder, who has granted bioRxiv a license to display the preprint in perpetuity. It is made available under aCC-BY 4.0 International license.

more at protein level intra-cellularly, in AGR53-DGCs, compared with AGR53-GSCs **C.** Western blotting showing FMOD is secreted more by AGR53-DGCs compared to AGR53-GSCs. Ponceau stained blot is used to ensure equal loading. **D.** Doxycycline addition induced FMOD knockdown at the mRNA level as well as at the **E.** protein level of AGR53-DGC/miRFMOD cells but not in the AGR53-DGC/miRNT cells. p value less than 0.05 is considered significant with *, **, *** representing p value less than 0.05, 0.01 and 0.001 respectively. ns stands for non-significant.

Supplementary Figure 8: FMOD does not play a role in GSC neurosphere formation and differentiation in murine GSCs. A. Bar diagram, quantifying number of spheres, shows no significant difference in sphere formation of AGR53-GSC/miRNT and AGR53-GSC/miRFMOD cells with or without doxycycline treatment. **B.** Limiting dilution assay shows no significant decrease (p=0.749) in the sphere-forming capacity of AGR53-GSC/miRNT and AGR53-GSC/miRFMOD cells with or without doxycycline treatment. **C.** Representative images showing no difference in neurosphere formation and subsequent differentiation of AGR53-GSC/miRNT and AGR53-GSC/miRFMOD cells with or without doxycycline treatment. Scale= 10X, Magnification= 200 μm. **D.** Real time qRT-PCR analysis showing that the addition of doxycycline did not hamper the differentiation potential of AGR53-GSC/miRNT and AGR53-GSC/miRFMOD cells with or without doxycycline treatment, as indicated by an upregulation of the astrocytic markers in all groups of cells. Embryonic Neuronal Stem Cells (ENSCs) were used as a negative control and astrocytes were used as a positive control. p values calculated by unpaired t test with Welch's correction are indicated. p value less than 0.05 is considered significant with *, **, *** representing p value less than 0.05, 0.01 and 0.001 respectively. ns stands for non-significant.

Supplementary Figure 9: FMOD does not play a role in GSC differentiation and reprogramming of murine GSCs. A. Representative images showing no difference in differentiation and subsequent neurosphere formation AGR53-DGC/miRNT and AGR53-DGC/miRFMOD cells with or without doxycycline treatment. Magnification=4X, Scale= 100 μm **B. Real-time** qRT-PCR analysis showing that the addition of doxycycline did not hamper the neurosphere formation potential of AGR53-DGC/miRNT and AGR53-DGC/miRFMOD cells with or without doxycycline treatment, as indicated by an upregulation of the stem cell markers in all groups of cells. Embryonic Neuronal Stem Cells (ENSCs) were used as a positive control

bioRxiv preprint doi: https://doi.org/10.1101/2022.04.03.486893; this version posted April 6, 2022. The copyright holder for this preprint (which was not certified by peer review) is the author/funder, who has granted bioRxiv a license to display the preprint in perpetuity. It is made available under aCC-BY 4.0 International license.

and astrocytes were used as a negative control. p values calculated by unpaired t-test with Welch's correction are indicated. P-value less than 0.05 is considered significant with *, **, *** representing p-value less than 0.05, 0.01 and 0.001 respectively. ns stands for non-significant.

Supplementary Figure 10: Validation of FMOD levels and knockdown in DBT-Luc mouse glioma cell-line. A. DBT-Luc cells were reprogrammed from DGCs to GSCs, and it was found that the mouse-stem-cell markers (MELK, NESTIN, BMI1, KLF4, TWIST2, PTGS2, and S100A6) were significantly upregulated in the DBT-Luc-GSCs, compared with the DBT-Luc-DGCs, at the mRNA level. **B.** It was also observed that the astrocytic markers (ASBG1, ALD1H1, GFAP, S100B) were significantly higher the mRNA level, in the DBT-Luc-DGCs compared with the DBT-Luc-GSCs. **C.** FMOD mRNA level was significantly higher in the DBT-Luc-DGCs compared with DBT-Luc-GSCs. **D.** FMOD protein level was also significantly higher in the DBT-Luc-DGCs compared to DBT-Luc-GSCs. **E.** Upon Doxycycline addition, a significant reduction in FMOD mRNA level was seen in DBT-Luc-DGC/miRFMOD (Dox+) group compared with DBT-Luc-DGC/miRFMOD (Dox-) group. No difference was seen in FMOD mRNA level between DBT Luc-DGC/miRNT (Dox-) and DBT-Luc-DGC/miRNT (Dox+) group of cells. **F.** Upon Doxycycline addition, a significant reduction in FMOD protein level was seen in DBT-Luc-DGC/miRFMOD(Dox+) group compared to DBT-Luc-DGC/miRFMOD(Dox-) group. No difference was seen in FMOD protein level between DBT-Luc-DGC/miRNT(Dox-) and DBT-Luc-DGC/miRNT(Dox+) group of cells. **G.** Upon Doxycycline addition, mCherry expression was seen in both DBT-Luc-DGC/miRNT and DBT-Luc-DGC/miRFMOD group of cells. Magnification- 4X, Scale- 200µm. p values calculated by unpaired t-test with Welch's correction are indicated. p-value less than 0.05 is considered significant with *, **, *** representing p-value less than 0.05, 0.01 and 0.001 respectively. ns stands for non-significant.

Supplementary Figure 11: FMOD does not have a role in de-differentiation of DGCs to GSCs A. U251-DGC/shNT and U251-DGC/shFMOD cells show no difference in growth in DMEM, or in neurosphere formation, when plated in stem-cell media in ultra-low attachment plates. Magnification = 10X, Scale: 100µm. Bar diagram, quantified from **A,** shows that there is no significant decrease in sphere formation of U251 de-differentiated cells (U251/GSCs) between U251-GSC/shNT and U251-GSC/shFMOD conditions. **B.** Limiting dilution assay

bioRxiv preprint doi: https://doi.org/10.1101/2022.04.03.486893; this version posted April 6, 2022. The copyright holder for this preprint (which was not certified by peer review) is the author/funder, who has granted bioRxiv a license to display the preprint in perpetuity. It is made available under aCC-BY 4.0 International license.

shows no significant decrease (p=0.89) in neurosphere forming capacity of U251 neurospheres between U251-GSC/shNT (black line) and U251-GSC/shFMOD (red line) conditions. **C.** Real-time qPCR analysis shows that the four GSC reprogramming factors (OLIG2, SOX2, POU3F2, and SALL2) have similar less expression in both U251-DGC/shNT and U251-DGC/shFMOD (depicted by solid blue and solid red respectively), but undergo an expected similar significant increase in U251-GSC/shNT and U251-GSC/shFMOD cells (depicted by striped blue and striped, red bars respectively). p values calculated by unpaired t-test with Welch's correction are indicated. P-value less than 0.05 is considered significant with *, **, *** representing p-value less than 0.05, 0.01 and 0.001 respectively. ns stands for non-significant.

Supplementary Figure 12: Induction with doxycycline reduces FMOD level in DBT-GSC-Luc+DBT-DGC-Luc/miRFMOD(Dox+) tumors. Western blot validating a decreased FMOD expression in tumors formed by co-injecting DBT-GSC-Luc cells with DBT-DGC-Luc/miRFMOD, upon doxycycline induction. Expression of FMOD was higher in all the other co-injection tumor groups (DBT-GSC-Luc+DBT-DGC-Luc/miRNT(Dox+), DBT-GSC-Luc+DBT-DGC-Luc/miRNT(Dox-) DBT-GSC-Luc+DBT-DGC-Luc/miRFMOD(Dox-)) and the DBT-Luc-DGC(Dox-) tumors, while it was low in the DBT-Luc-GSC(Dox -)tumor.

Supplementary Figure 13: DGC-secreted FMOD induces angiogenesis by endothelial cells of various origins.A. Representative images of the decrease in the number of networks formed by ST1 cells when treated with U251/siFMOD CM, compared with U251/siNT CM, which is rescued by the exogenous addition of rhFMOD. **B.** Representative images (left) and quantification (right) of the decrease in the number of networks formed by ST1 cells when treated with U251/shFMOD CM, compared with U251/shFMOD CM. **C.** Representative images (top) and quantification (bottom) of the number of networks formed by the ST1 cells **show** that the cells form significantly less networks when an FMOD neutralizing antibody is added, as compared to control antibody (IgG). BSA is used as a control for rhFMOD. **D.** Quantification of the number of networks formed in *in vitro* angiogenesis assay upon treatment of ST1 cells with the CM from MGG4, MGG6 and MGG8 GSCs and their corresponding DGCs. **E.** Representative images of the decrease in the number of networks formed by ST1 cells when treated with MGG8-DGC/siFMOD CM, compared with MGG8-DGC/siFMOD CM, which is rescued by the exogenous addition of rhFMOD(left). Quantification of the number of networks formed (right). p values calculated by unpaired t-test with Welch's correction are indicated. P-

bioRxiv preprint doi: https://doi.org/10.1101/2022.04.03.486893; this version posted April 6, 2022. The copyright holder for this preprint (which was not certified by peer review) is the author/funder, who has granted bioRxiv a license to display the preprint in perpetuity. It is made available under aCC-BY 4.0 International license.

value less than 0.05 is considered significant with *, **, *** representing p-value less than 0.05, 0.01 and 0.001 respectively.

Supplementary Figure 14: FMOD enhances angiogenesis as well as the migration and invasion, but not the proliferation of endothelial cells. A. Representative images (left) and quantification (right) from Boyden chamber assay showing increased migration of ST1 cells upon rhFMOD treatment over BSA. Magnification=10x scale=100μm.**B.** Representative images (left) and quantification (right) from Boyden chamber assay showing reduced migration of ST1 cells upon MGG8-DGC/shFMOD CM treatment compared with MGG8-DGC/shNT CM treatment. Magnification=10x scale=100μm.**C.** Representative images (left) and quantification (right) from Boyden chamber assay showing increased invasion of ST1 cells upon rhFMOD treatment over BSA. Magnification=10x scale=100μm.**D.** Representative images (left) and quantification (right) from Boyden chamber assay showing reduced invasion of ST1 cells upon MGG8-DGC/shFMOD CM treatment compared with MGG8-DGC/shNT CM treatment. Magnification=10x scale=100μm. **E.** MTT cell-proliferation assay shows no difference in the proliferation of ST1 cells treated with either BSA or rfFMOD, over a period of 96 hours. **F.** Representative images (top) and quantification (bottom) of the decrease in the number of networks formed by immortalized mouse brain-derived endothelial cells, B.End3, upon treatment with MGG8-DGC/shFMOD CM, compared with MGG8-DGC/shNT CM, which is rescued upon exogenous addition of rhFMOD. p values calculated by unpaired t-test with Welch's correction are indicated. P-value less than 0.05 is considered significant with *, **, *** representing p-value less than 0.05, 0.01 and 0.001 respectively. ns stands for non-significant.

Supplementary Figure 15: FMOD induces GBM cells to undergo transdifferentiation. A. Real-time qRT-PCR analysis showing the expression of CD31(blue bars) and FMOD (orange bars) in ST1 cells and U87 cells, before and after transdifferentiation (TDECs represent the transdifferentiated cells).). **B.** Western blotting showing the expression of FMOD (top) and CD31 (bottom) in U87 cells, before and after transdifferentiation (TDECs represent the transdifferentiated cells). **C**. Representative images of *in vitro* network formation by U87 and U87 TDECs upon BSA and rhFMOD treatments. Magnification 10X, Scale bar = 100 μm. **D.** Quantification of the number of complete networks formed in **C.** p-value is calculated by unpaired t-test with Welch's correction are indicated. P-value less than 0.05 is considered

bioRxiv preprint doi: https://doi.org/10.1101/2022.04.03.486893; this version posted April 6, 2022. The copyright holder for this preprint (which was not certified by peer review) is the author/funder, who has granted bioRxiv a license to display the preprint in perpetuity. It is made available under aCC-BY 4.0 International license.

significant with *, **, *** representing p value less than 0.05, 0.01 and 0.001 respectively. ns stands for non-significant.

Supplementary Figure 16: FMOD induces activation of Notch signaling in endothelial cells. **A.** rhFMOD induces a significant increase in CSL Luc (Notch pathway-dependent reporter luciferase construct) activity in ST1 cells, an effect reduced by cell pretreatment with γ-secretase inhibitor (GSI, 10μM), a Notch pathway inhibitor. **B**. rhFMOD induces a significant increase in HES Luc activity (Notch pathway-dependent reporter (HES1 promoter) luciferase construct), which is reduced when ST1 cells are pre-treated with GSI. **C.** Western blotting showing a time-dependent translocation of the Notch intracellular domain (NICD) from the cytoplasm to the nucleus in ST1 cells, upon treatment with rhFMOD. Histone H3 was used as a nuclear loading control, GAPDH as a cytoplasmic loading control. **D.** Immunocytochemical analysis showing that rhFMOD treatment of endothelial cells causes translocation of NICD from the cytoplasm to the nucleus in a time-dependent manner. BSA is used as a control. Magnification = 40X, Scale bar= 50μm. **E.** rhFMOD-mediated increase in the reporter-luciferase activity of CSL Luc significantly decreases in ST1 endothelial cells pre-treated with the RGD peptide. **F.** rhFMOD-mediated increase in the reporter-luciferase activity of HES Luc significantly decreases in ST1 cells pre-treated with the RGD peptide. p-value is calculated by unpaired t-test with Welch's correction are indicated. P-value less than 0.05 is considered significant with *, **, *** representing p-value less than 0.05, 0.01 and 0.001 respectively. ns stands for non-significant.

Supplementary Figure 17: ST1 cells stably expressing NICD are independent of FMOD in forming angiogenic networks. **A.** Western blotting confirming the overexpression of NICD in ST1 cells. **B.** Immunocytochemistry analysis confirming the overexpression of NICD in ST1 cells. **C.** Representative images of network formation by control and NICD overexpressed ST1 cells in the presence of BSA and rhFMOD. Magnification = 63x, Scale=20 μm. **D**. Quantification of the number of networks formed in **C.** p-values calculated by unpaired t-test with Welch's correction are indicated. P-value less than 0.05 is considered significant with *, **, *** representing p-value less than 0.05, 0.01 and 0.001, respectively. ns stands for non-significant.

Supplementary Figure 18: FMOD-Type I collagen interaction is crucial for FMOD-mediated activation of downstream signaling pathways. **A**. Bar diagram showing that

bioRxiv preprint doi: https://doi.org/10.1101/2022.04.03.486893; this version posted April 6, 2022. The copyright holder for this preprint (which was not certified by peer review) is the author/funder, who has granted bioRxiv a license to display the preprint in perpetuity. It is made available under aCC-BY 4.0 International license.

rhFMOD cannot activate Notch-dependent reporter luciferase activity of CSL Luc in ST1 cells in the presence of WT peptide but can do so in the presence of mutant peptide. **B.** Bar diagram showing that rhFMOD cannot activate Notch-dependent reporter luciferase activity of HES Luc in ST1 cells in the presence of WT peptide but can do so in the presence of mutant peptide. **C.** Bar diagram quantifying the number of networks formed in *in vitro* angiogenesis assay shows that the WT (wild-type) peptide competes with rhFMOD to bind to Type I Collagen, whereas the mutant peptide cannot. Hence, rhFMOD induces more angiogenesis in the presence of the mutant peptide, as Type I Collagen is free for it to bind. However, because of the competition with the WT peptide, rhFMOD less efficiently induces angiogenesis in endothelial cells. **D.** Western blotting shows reduced induction in pFAk levels in rhFMOD-treated ST1/shITGB1 cells compared with the rhFMOD-treated ST1/shNT cells, where pFAK levels increae at 30 and 60 mins, while total FAK remains constant in both the cases. **E.** Western blotting shows reduced induction in pFAk levels in rhFMOD-treated ST1/shITGAV cells compared with the rhFMOD-treated ST1/shNT cells, where pFAK levels increae at 30 and 60 mins, while total FAK remains constant in both the cases. **F.** Western blotting shows reduced induction in pFAk levels in rhFMOD-treated ST1/shITGA6 cells compared with the rhFMOD-treated ST1/shNT cells, where pFAK levels increae at 30 and 60 mins, while total FAK remains constant in both the cases. **G.** Western blotting showing knockdown of ITGB1 in shITGB1 transduced ST1 cells compared with ST1/shNT cells. **H.** Western blotting showing knockdown of ITGAV in shITGAV transduced ST1 cells compared with ST1/shNT cells. **I.** Western blotting showing knockdown of ITGA6 in shITGA6 transduced ST1 cells compared with ST1/shNT cells. p values calculated by unpaired t test with Welch's correction are indicated. p value less than 0.05 is considered significant with *, **, *** representing p value less than 0.05, 0.01 and 0.001 respectively. ns stands for non-significant.

Supplementary Figure 19: FMOD-mediated activation of Integrin-dependent Notch signaling in endothelial cells involve the integrin pathway downstream molecules FAK and Src. A. Bar diagram showing that rhFMOD cannot activate Notch dependent reporter luciferase activity of CSL Luc in ST1 cells pre-treated with FAK inhibitor. **B.** Bar diagram showing that rhFMOD cannot activate Notch dependent reporter luciferase activity of HES Luc in ST1 cells pre-treated with FAK inhibitor. **C.** Bar diagram showing that rhFMOD cannot activate Notch dependent reporter luciferase activity of CSL Luc in ST1 cells pre-treated with the specific Src

bioRxiv preprint doi: https://doi.org/10.1101/2022.04.03.486893; this version posted April 6, 2022. The copyright holder for this preprint (which was not certified by peer review) is the author/funder, who has granted bioRxiv a license to display the preprint in perpetuity. It is made available under aCC-BY 4.0 International license.

inhibitor PP2, but not when treated with the inactive structural analog, PP3. **D.** Bar diagram showing that rhFMOD cannot activate Notch dependent reporter luciferase activity of HES Luc in ST1 cells pre-treated with the specific Src inhibitor PP2, but not when treated with the inactive structural analog, PP3. **E.** Real-time qRT-PCR analysis shows that rhFMOD treatment of ST1 cells cause a time-dependent increase in HES1 mRNA which is inhibited in cells pre-treated with FAK inhibitor. **F.** Western blotting showing that rhFMOD treatment of ST1 cells cause a time-dependent increase in HES1 protein which is inhibited in cells pre-treated with FAK inhibitor. **G.** Real-time qRT-PCR analysis shows that rhFMOD treatment of ST1 cells cause a time-dependent increase in HES1 mRNA which is inhibited in cells pre-treated with the specific Src inhibitor PP2, but not when treated with the inactive structural analog, PP3. **H.** Western blotting showing that rhFMOD treatment of ST1 cells cause a time-dependent increase in HES1 protein which is inhibited in cells pre-treated with the specific Src inhibitor PP2, but not when treated with the inactive structural analog, PP3. p value less than 0.05 is considered significant with *, **, *** representing p value less than 0.05, 0.01 and 0.001 respectively.

Supplementary Figure 20: FMOD-mediated crosstalk of the integrin and Notch signaling pathways occurs via JAG1 upregulation. A. Real-time qRT-PCR analysis shows the rhFMOD-mediated increase in the mRNA levels of Notch ligands in a time-dependent manner. In cells that are pre-treated with RGD (10 μM), the rhFMOD-mediated increase of JAG1 and DLL3 are significantly reduced. **B.** Real-time qRT-PCR analysis shows that rhFMOD treatment of ST1 cells causes a time-dependent increase in JAG1 mRNA which is inhibited in cells pre-treated with FAK inhibitor. **C.** Real-time qRT-PCR analysis shows that rhFMOD treatment of ST1 cells cause a time-dependent increase in JAG1 mRNA which is inhibited in cells pre-treated with the specific Src inhibitor PP2, but not when treated with the inactive structural analog, PP3. **D.** rhFMOD-mediated CSL-Luc reporter-luciferase activity is significantly decreased in ST1/shJAG1 cells compared with ST1/shNT cells. **E.** rhFMOD-mediated HES-Luc reporter-luciferase activity is significantly decreased in ST1/shJAG1 cells compared with ST1/shNT cells. **F.** Real-time qRT-PCR analysis shows that rhFMOD treatment of ST1 upregulates 2 out of a set of 5 TFs in ST1, of which the expression of KLF8 (blue bar) shows a significant inhibition when the cells are pre-treated with RDG. **G.** Western blotting showing knockdown of KLF8 in siKLF8 transfected ST1 cells compared with ST1/siNT cells. **H.** Western blotting showing that rhFMOD treatment of ST1 cells cause a time-dependent increase in JAG1 protein which is inhibited in

bioRxiv preprint doi: https://doi.org/10.1101/2022.04.03.486893; this version posted April 6, 2022. The copyright holder for this preprint (which was not certified by peer review) is the author/funder, who has granted bioRxiv a license to display the preprint in perpetuity. It is made available under aCC-BY 4.0 International license.

cells are silenced for KLF8. p value less than 0.05 is considered significant with *, **, *** representing p value less than 0.05, 0.01 and 0.001 respectively. ns stands for non-significant.

Supplementary Figure 21: Clinical relevance of the FMOD-JAG1-HES1 signaling. A. FMOD is upregulated at the transcript level in GBM samples over normal samples across multiple publicly available datasets. **B.** HES1 is upregulated at the transcript level in GBM samples over normal samples across multiple publicly available datasets. **C.** JAG1 is upregulated at the transcript level in GBM samples over normal samples across multiple publicly available datasets. **D.** FMOD and HES1 mRNAs are significantly positively correlated across multiple publicly available datasets. **E.** FMOD and JAG1 mRNAs are significantly positively correlated across multiple publicly available datasets.

Supplementary Figure 22: Clinical relevance of the FMOD-JAG1-HES1 signaling. A. High FMOD mRNA levels in patients show poorer survival than low FMOD patients, in multiple publicly available datasets. **B.** FMOD promoter hypomethylation (in CpGs cg03764585 and cg04704856) in patients show poorer survival than low patients with FMOD promoter hypermethylation, in multiple publicly available datasets.

Supplementary Figure 23: Conditional silencing of FMOD in DGCs formed *de novo* by GSC-initiated tumors inhibits tumor growth. A. *In vivo* fluorescent imaging of mice injected with either DBT-Luc-GSC/miRNT or DBT-Luc-GSC/miRFMOD cells. **B.** Haematoxylin and Eosin staining shows a larger tumor (depicted by dark blue color due to extremely high cellular density) in mice brain injected with DBT-Luc-GSC/miRFMOD (Dox-), but not in DBT-Luc-GSC/miRFMOD (Dox+) cells. **C.** Kaplan-Meier survival graphs showing the survival of mice injected with DBT-Luc-GSC/miRFMOD(Dox-) or DBT-Luc-GSC/miRFMOD (Dox+) cells. **D.** Immunohistochemical analysis showing FMOD expression in brains of mice injected with DBT-Luc-GSC/miRFMOD(Dox-) or DBT-Luc-GSC/miRFMOD(Dox+) cells. Red represents FMOD and blue represents H33342. The merged images have been shown for representation. Magnification = 20x, Scale=100 μm.

Supplementary Figure 24: FMOD-silencing does not hamper the differentiation potential of tumor cells in murine glioma models. A. Immunohistochemical analysis of brain-derived sections obtained from mice injected with AGR53-GSC/miRNT cell show FMOD, GFAP, and

bioRxiv preprint doi: https://doi.org/10.1101/2022.04.03.486893; this version posted April 6, 2022. The copyright holder for this preprint (which was not certified by peer review) is the author/funder, who has granted bioRxiv a license to display the preprint in perpetuity. It is made available under aCC-BY 4.0 International license.

CD133 expression, and co-localization of FMOD with GFAP, and not with CD133 (left, after doxycycline injection). **B.** Bar diagram quantifying mean fluorescence intensity of CD133 and GFAP in AGR53-GSC/miRNT cells after doxycycline injection. **C.** Bar diagram quantifying co-localization of FMOD with CD133 and GFAP, respectively, in AGR53-GSC/miRNT cells after doxycycline injection. **D.** Immunohistochemical analysis of brain-derived sections obtained from mice injected with AGR53-GSC/miFMOD cell show low FMOD, and hifg GFAP, and CD133 expression, and loss of co-localization of FMOD with GFAP (right, after doxycycline injection). **E.** Bar diagram quantifying mean fluorescence intensity of CD133 and GFAP in AGR53-GSC/miRFMOD cells after doxycycline injection. **F.** Bar diagram quantifying co-localization of FMOD with CD133 and GFAP, respectively, in AGR53-GSC/miRNT cells after doxycycline injection. Magnification for panels **A** and **D** =20 X, Scale= 100 μm. p-values for panels **B, C, E**, and **F** are calculated by Student's t-test, p-value are represented by *, **, *** indicate values <0.05, <0.01, and <0.001 respectively.

Supplementary Figure 25: FMOD-silencing does not hamper the differentiation potential of tumor cells in murine glioma models. **A.** Immunohistochemical analysis of brain-derived sections obtained from mice injected with DBT-Luc-GSC/miRFMOD cell show FMOD, GFAP, and CD133 expression, and co-localization of FMOD with GFAP, and not with CD133 (left, before doxycycline injection). **B.** Bar diagram quantifying mean fluorescence intensity of CD133 and GFAP in DBT-Luc-GSC/miRFMOD cells without doxycycline injection. **C.** Bar diagram quantifying co-localization of FMOD with CD133 and GFAP, respectively, in DBT-Luc-GSC/miRFMOD cells before doxycycline injection. **D.** Immunohistochemical analysis of brain-derived sections obtained from mice injected with DBT-Luc-GSC/miRFMOD cell show low FMOD, and high GFAP, and CD133 expression, and loss of co-localization of FMOD with GFAP (right, with doxycycline injection). **E.** Bar diagram quantifying mean fluorescence intensity of CD133 and GFAP in DBT-Luc-GSC/miRFMOD cells after doxycycline injection. **F.** Bar diagram quantifying co-localization of FMOD with CD133 and GFAP, respectively, in DBT-Luc-GSC/miRFMOD cells after doxycycline injection. Magnification for panels **A** and **D** =20 X, Scale= 100 μm. p-values for panels **B, C, E**, and **F** are calculated by Student's t-test, p-value are represented by *, **, *** indicate values <0.05, <0.01, and <0.001 respectively.

bioRxiv preprint doi: https://doi.org/10.1101/2022.04.03.486893; this version posted April 6, 2022. The copyright holder for this preprint (which was not certified by peer review) is the author/funder, who has granted bioRxiv a license to display the preprint in perpetuity. It is made available under aCC-BY 4.0 International license.

Supplementary Figure 26: FMOD-silencing does not hamper the differentiation potential of tumor cells. A. Immunohistochemical analysis of brain-derived sections obtained from mice injected with MGG8-GSC/shNT cells show FMOD, GFAP, and CD133 expression, and co-localization of FMOD with GFAP, and not with CD133 (left). **B.** Bar diagram quantifying mean fluorescence intensity of CD133 and GFAP in MGG8-GSC/shNT cells. **C.** Bar diagram quantifying co-localization of FMOD with CD133 and GFAP, respectively, in MGG8-GSC/shNT cells. **D.** Immunohistochemical analysis of brain-derived sections obtained from mice injected with MGG8-GSC/shFMOD cells show low FMOD, and high GFAP, and CD133 expression, and loss of co-localization of FMOD with GFAP (right, after doxycycline injection). **E.** Bar diagram quantifying mean fluorescence intensity of CD133 and GFAP in MGG8-GSC/shFMOD cells. **F.** Bar diagram quantifying co-localization of FMOD with CD133 and GFAP, respectively, in MGG8-GSC/shFMOD cells. Magnification for panels **A** and **D** =20 X, Scale= 100 μm. p-values for panels **B, C, E**, and **F** are calculated by Student's t-test, p-value are represented by *, **, *** indicate values <0.05, <0.01, and <0.001 respectively.

Supplementary Figure 27: FMOD-silencing affects angiogenesis and vascular mimicry *in vivo*. A. Immunohistochemical analysis shows that the expression of von Willebrand Factor (vWF), a blood vessel marker, lining the blood vessels in both AGR53-GSC/miRNT and AGR53-GSC/miRFMOD groups, after doxycycline injection. Brain sections of two time points, day21 and day 55 were stained for the expression of vWF. At both time points, AGR53-GSC/miRFMOD shows lesser vWF staining than the AGR53-GSC/miRNT group. Magnification=20x, Scale= 100 μm. **B.** Bar diagram showing the mean intensity of vWF and **C.** The mean area of blood vessels in the AGR53-GSC/miRNT and AGR53-GSC/miRFMOD groups. **D.** Immunohistochemical analysis shows that the expression of CD31, lining the blood vessels in both DBT-Luc-GSC/miRFMOD(Dox-) and DBT-Luc-GSC/miRFMOD(Dox+) groups. **E.** Bar diagram showing the mean intensity of vWF and **F.** The mean area of blood vessels in the DBT-Luc-GSC/miRFMOD(Dox-) and DBT-Luc-GSC/miRFMOD(Dox+) groups. **G.** Immunohistochemical analysis showing overlap of CD31 (red) and GFP (green) expression in brains of mice injected with both DBT-Luc-GSC/miRFMOD cells, with or without doxycycline injection. Yellow allow indicates the region depicting the colocalization of both the two markers. **H.** Quantification of the colocalization coefficient in both DBT-Luc-GSC/miRFMOD(Dox-) and DBT-Luc-GSC/miRFMOD(Dox+) groups. **I.** Quantification of the VM+ blood vessels,

bioRxiv preprint doi: https://doi.org/10.1101/2022.04.03.486893; this version posted April 6, 2022. The copyright holder for this preprint (which was not certified by peer review) is the author/funder, who has granted bioRxiv a license to display the preprint in perpetuity. It is made available under aCC-BY 4.0 International license.

indicating the measure of vascular mimicry (VM) in both DBT-Luc-GSC/miRFMOD(Dox-) and DBT-Luc-GSC/miRFMOD(Dox+) groups. p values calculated by unpaired t test with Welch's correction are indicated. p value less than 0.05 is considered significant with *, **, *** representing p value less than 0.05, 0.01 and 0.001, respectively. ns stands for non-significant. Magnification = 20x, Scale=100 μm.

Supplementary Figure 28: FMOD-dependent activation of the integrin-FAK-JAG1-HES1 signaling axis is maintained *in vivo*. A. Immunohistochemical analysis shows co-staining of CD31 with FMOD, pFAK, JAG1, and HES 1 in brain section derived from MGG8/shNT groups of animals. **B.** Immunohistochemical analysis shows co-staining of CD31 with FMOD, pFAK, JAG1, and HES 1 in brain section derived from AGR53-GSC/miRNT group of animals, after doxycycline injection. **C.** Immunohistochemical analysis shows co-staining of CD31 with FMOD, pFAK, JAG1, and HES 1 in brain section derived from DBT-Luc-GSC/miRFMOD group of animals, without doxycycline injection. Magnification = 20x, Scale=100 μm.

@@

Supplementary figures 1 to 12

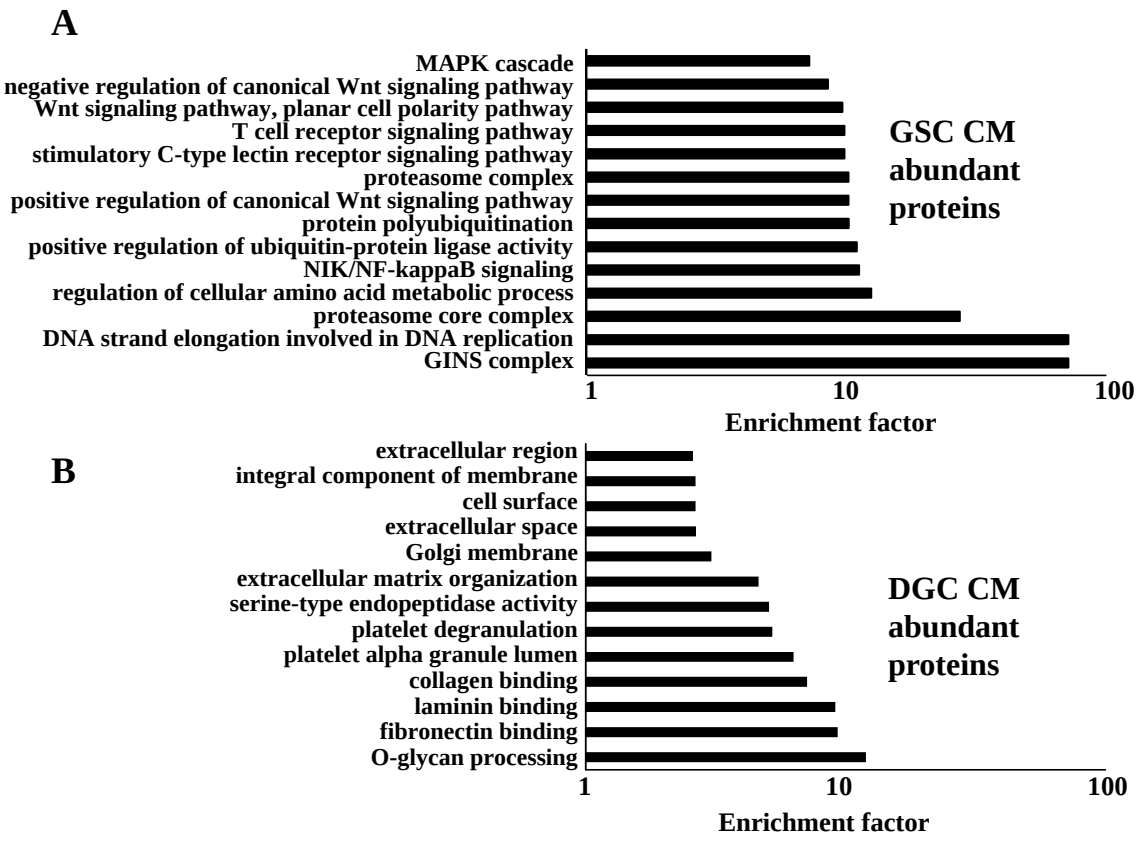
A
MAPK cascade
negative regulation of canonical Wnt signaling pathway
Wnt signaling pathway, planar cell polarity pathway
T cell receptor signaling pathway
stimulatory C-type lectin receptor signaling pathway
proteasome complex
positive regulation of canonical Wnt signaling pathway
protein polyubiquitination
positive regulation of ubiquitin-protein ligase activity
NIK/NF-kappaB signaling
regulation of cellular amino acid metabolic process
proteasome core complex
DNA strand elongation involved in DNA replication
GINS complex
GSC CM abundant proteins
1
10
100
Enrichment factor
B
extracellular region
integral component of membrane
cell surface
extracellular space
Golgi membrane
extracellular matrix organization
serine-type endopeptidase activity
platelet degranulation
platelet alpha granule lumen
collagen binding
laminin binding
fibronectin binding
O-glycan processing
DGC CM abundant proteins
1
10
100
Enrichment factor

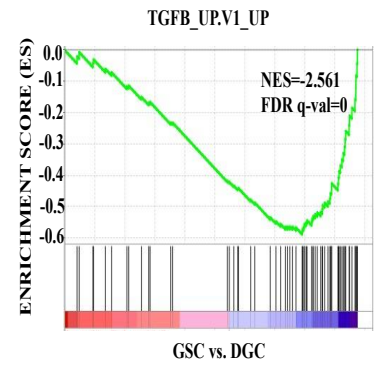
TGFB_UP.V1_UP
NES=-2.561
FDR q-val=0
ENRICHMENT SCORE (ES)
GSC vs. DGC

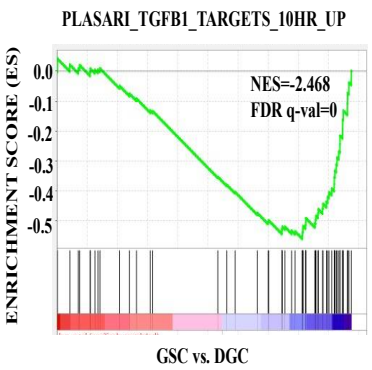
PLASARI_TGFB1_TARGETS_10HR_UP
NES=-2.468
FDR q-val=0
ENRICHMENT SCORE (ES)
GSC vs. DGC

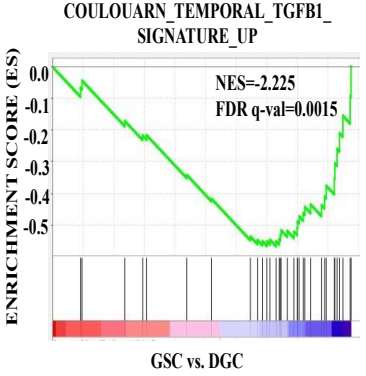
COULOUARN_TEMPORAL_TGFB1_SIGNATURE_UP
NES=-2.225
FDR q-val=0.0015
ENRICHMENT SCORE (ES)
GSC vs. DGC

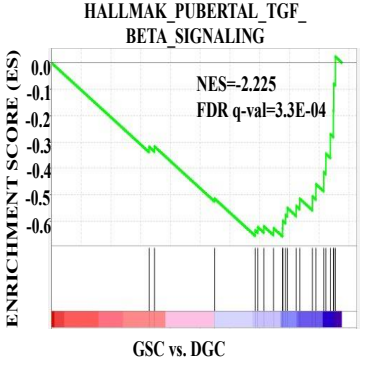
HALLMAK_PUBERTAL_TGF_BETA_SIGNALING
NES=-2.225
FDR q-val=3.3E-04
ENRICHMENT SCORE (ES)
GSC vs. DGC

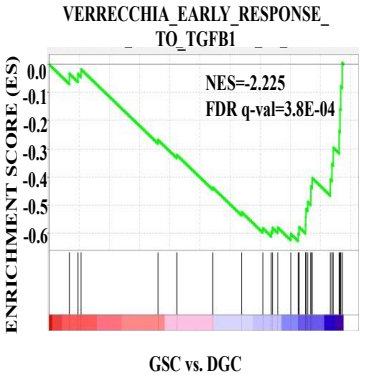
VERRECCHIA_EARLY_RESPONSE_TO_TGFB1
NES=-2.225
FDR q-val=3.8E-04
ENRICHMENT SCORE (ES)
GSC vs. DGC

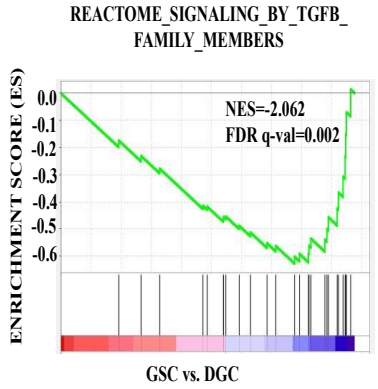
REACTOME_SIGNALING_BY_TGFB_FAMILY_MEMBERS
NES=-2.062
FDR q-val=0.002
ENRICHMENT SCORE (ES)
GSC vs. DGC

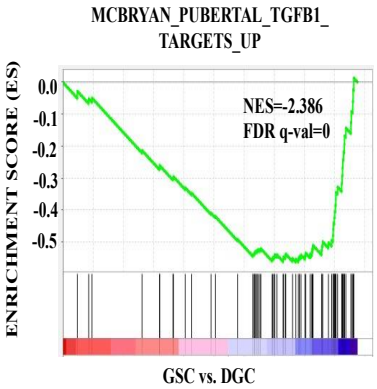
MCBRYAN_PUBERTAL_TGFB1_TARGETS_UP
NES=-2.386
FDR q-val=0
ENRICHMENT SCORE (ES)
GSC vs. DGC

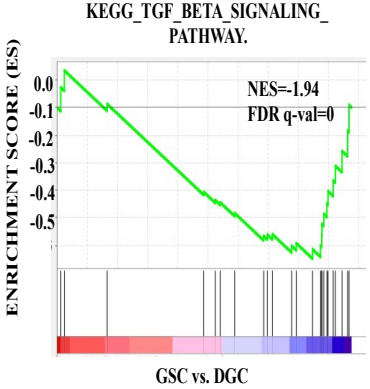
KEGG_TGF_BETA_SIGNALING_PATHWAY.
NES=-1.94
FDR q-val=0
ENRICHMENT SCORE (ES)
GSC vs. DGC

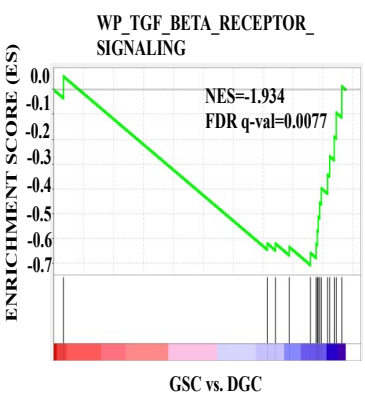
WP_TGF_BETA_RECEPTOR_SIGNALING
NES=-1.934
FDR q-val=0.0077
ENRICHMENT SCORE (ES)
GSC vs. DGC

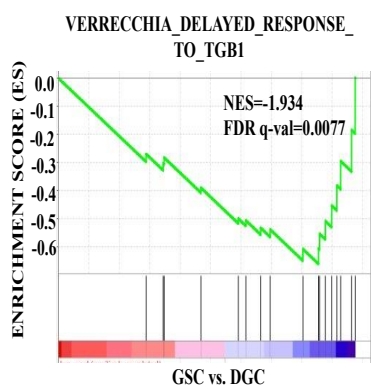
VERRECCHIA_DELAYED_RESPONSE_TO_TGB1
NES=-1.934
FDR q-val=0.0077
ENRICHMENT SCORE (ES)
GSC vs. DGC

TGF Beta signaling pathway gene sets[#]	Gill[&]		Graveendeel[&]		Grzmil[&]		TCGA_affymetrix[&]		TCGA_agilent[&]		TCGA_RNA Seq[&]	
	NES[*]	p-value[%]	NES[*]	p-value[%]	NES*	p-value[%]	NES*	p-value[%]	NES*	p-value[%]	NES*	p-value[%]
COULOUARN_TEMPORAL_TGFB1_SIGNATURE_UP	1.53	0.02	1.86	0.00	1.20	0.25	2.05	0.00	1.95	0.00	1.61	0.01
HALLMARK_TGF_BETA_SIGNALING	2.10	0.00	1.91	0.00	NA	NA	1.82	0.02	1.69	0.01	1.72	0.02
KEGG_TGF_BETA_SIGNALING_PATHWAY	1.46	0.04	1.94	0.01	1.36	0.13	1.80	0.01	1.62	0.02	1.16	0.23
MCBRYAN_PUBERTAL_TGFB1_TARGETS_UP	2.66	0.00	2.58	0.00	2.09	0.00	2.63	0.00	2.63	0.00	2.52	0.00
PLASARI_TGFB1_TARGETS_10HR_UP	1.78	0.00	1.97	0.00	1.90	0.00	0.97	0.53	1.42	0.03	1.15	0.18
REACTOME_SIGNALING_BY_TGFB_FAMILY_MEMBERS	1.16	0.26	1.59	0.02	NA	NA	1.57	0.04	1.33	0.12	0.76	0.85
TGFB_UP.V1_UP	1.61	0.01	1.56	0.01	0.79	0.75	0.86	0.70	-0.57	0.97	1.04	0.40
VERRECCHIA_DELAYED_RESPONSE_TO_TGFB1	2.55	0.00	1.76	0.02	NA	NA	1.96	0.00	2.19	0.00	2.27	0.00
VERRECCHIA_EARLY_RESPONSE_TO_TGFB1	3.06	0.00	3.11	0.00	NA	NA	3.08	0.00	2.85	0.00	2.69	0.00
WP_TGFBETA_RECEPTOR_SIGNALING	1.94	0.01	1.85	0.01	NA	NA	1.76	0.01	1.90	0.01	1.35	0.09
WP_TGFBETA_RECEPTOR_SIGNALLING_IN_SKELETAL_DYSPLA	1.87	0.00	1.83	0.00	NA	NA	1.88	0.01	1.92	0.00	1.27	0.15

*-Postive NES score
1.00
2.00
3.00
4.00

Significance
% -p-val < 0.05 considered significant
NA = Not available

&- Datasets used
Gill-GSE59612
Gravendeel-GSE16011
Grzmil-GSE59612
TCGA_Affymetrix-from TCGA
TCGA_Agilent-from TCGA
TCGA_RNASeq-from TCGA

Enrichment of mesenchymal gene expression signature and TGF beta signaling pathway in DGCs

Gene expression sub type# or signaling pathway[$]	Glioma stem-like cells (GSCs)[&]									Differentiated glioma cells (DGCs)[&]								
	MGG4_GSC_1	MGG4_GSC_2	MGG4_GSC_3	MGG6_GSC_1	MGG6_GSC_2	MGG6_GSC_3	MGG8_GSC_1	MGG8_GSC_2	MGG8_GSC_3	MGG4_DGC_1	MGG4_DGC_2	MGG4_DGC_3	MGG6_DGC_1	MGG6_DGC_2	MGG6_DGC_3	MGG8_DGC_1	MGG8_DGC_2	MGG8_DGC_3
VERHAAK_GLIOBLASTOMA_CLASSICAL	-0.21	-0.25	-0.30	0.17	0.14	0.19	-0.23	-0.06	-0.27	-0.14	-0.02	-0.08	0.10	-0.09	-0.11	-0.10	-0.20	-0.13
VERHAAK_GLIOBLASTOMA_MESENCHYMAL	-0.47	-0.45	-0.47	-0.47	-0.39	-0.47	-0.50	-0.45	-0.49	0.32	0.31	0.33	0.39	0.35	0.28	0.24	0.23	0.18
VERHAAK_GLIOBLASTOMA_NEURAL	-0.02	0.08	0.09	-0.17	-0.06	-0.28	0.03	-0.28	-0.03	0.07	0.06	0.09	0.08	0.03	-0.10	0.00	0.07	0.11
VERHAAK_GLIOBLASTOMA_PRONEURAL	0.12	0.10	0.15	0.22	0.19	0.15	0.26	0.04	0.32	-0.31	-0.36	-0.38	-0.41	-0.33	-0.46	-0.35	-0.21	-0.24
HALLMARK_TGF_BETA_SIGNALING[$]	-0.33	-0.28	-0.22	-0.28	-0.42	-0.31	-0.47	-0.34	-0.54	0.08	-0.02	0.01	0.19	0.18	0.31	0.29	0.27	0.30

#- Verhaak RG, Hoadley KA, Purdom E, Wang V, Qi Y, Wilkerson MD, Miller CR, Ding L, Golub T, Mesirov JP, et al. Integrated genomic analysis identifies clinically relevant subtypes of glioblastoma characterized by abnormalities in PDGFRA, IDH1, EGFR, and NF1. Cancer Cell. 2010;17:98–110.

$- HALLMARK_TGF_BETA_SIGNALING gene set from the Hallmark gene sets of the Molecular Signatures Database (MSigDB), containing genes up-regulated in response to TGFB1.

& - Suva, M. L., E. Rheinbay, S. M. Gillespie, A. P. Patel, H. Wakimoto, et.al. Reconstructing and reprogramming the tumor-propagating potential of glioblastoma stem-like cells. Cell.2014;157:580-94.

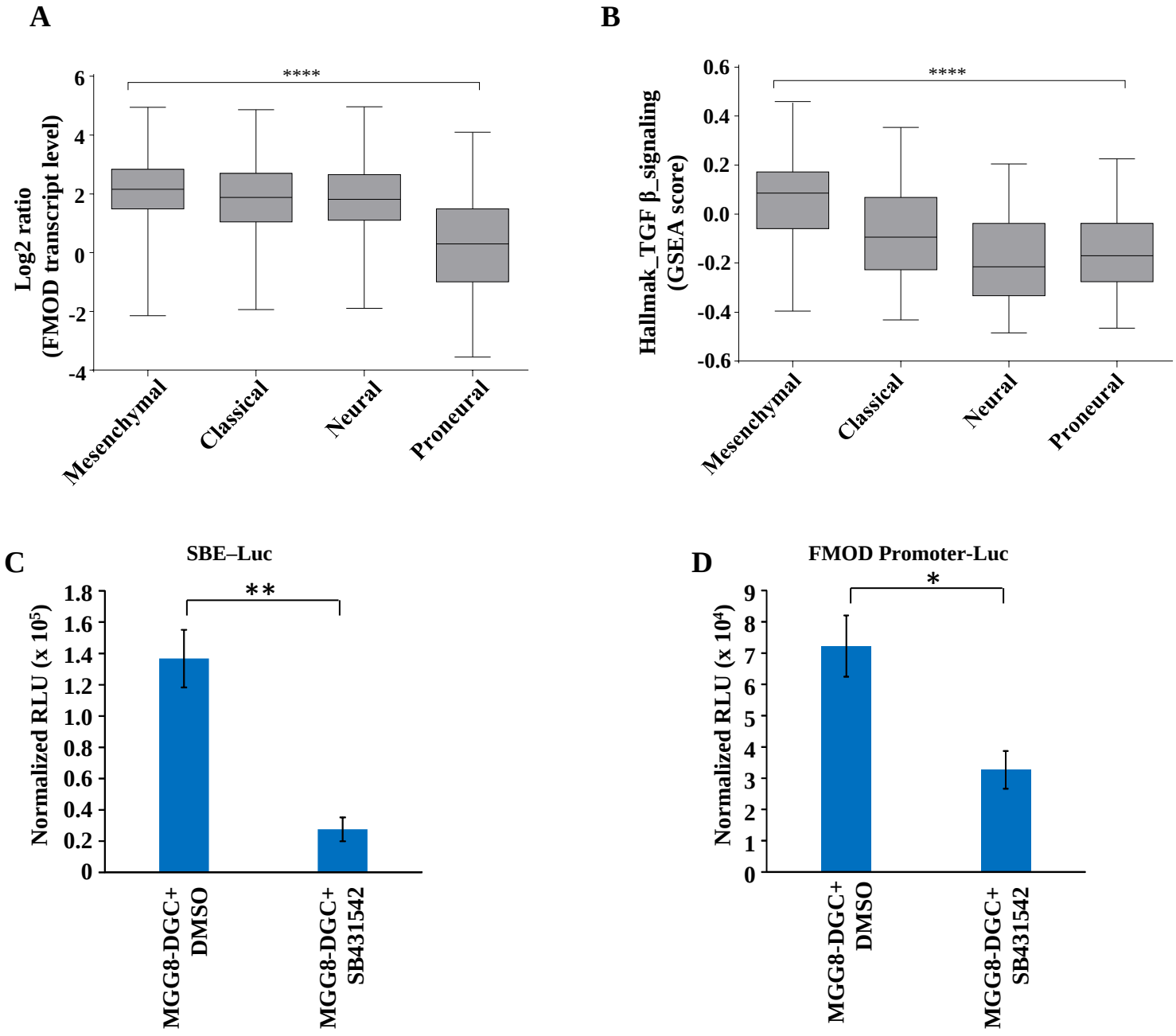
A
Log2 ratio
(FMOD transcript level)
6
4
2
0
-2
-4
****
Mesenchymal
Classical
Neural
Proneural
B
Hallmak_TGF β_signaling
(GSEA score)
0.6
0.4
0.2
0.0
-0.2
-0.4
-0.6
****
Mesenchymal
Classical
Neural
Proneural
C
SBE–Luc
Normalized RLU (x 10^5)
1.8
1.6
1.4
1.2
1.0
0.8
0.6
0.4
0.2
0
**
MGG8-DGC+ DMSO
MGG8-DGC+ SB431542
D
FMOD Promoter-Luc
Normalized RLU (x 10^4)
9
8
7
6
5
4
3
2
1
0
*
MGG8-DGC+ DMSO
MGG8-DGC+ SB431542

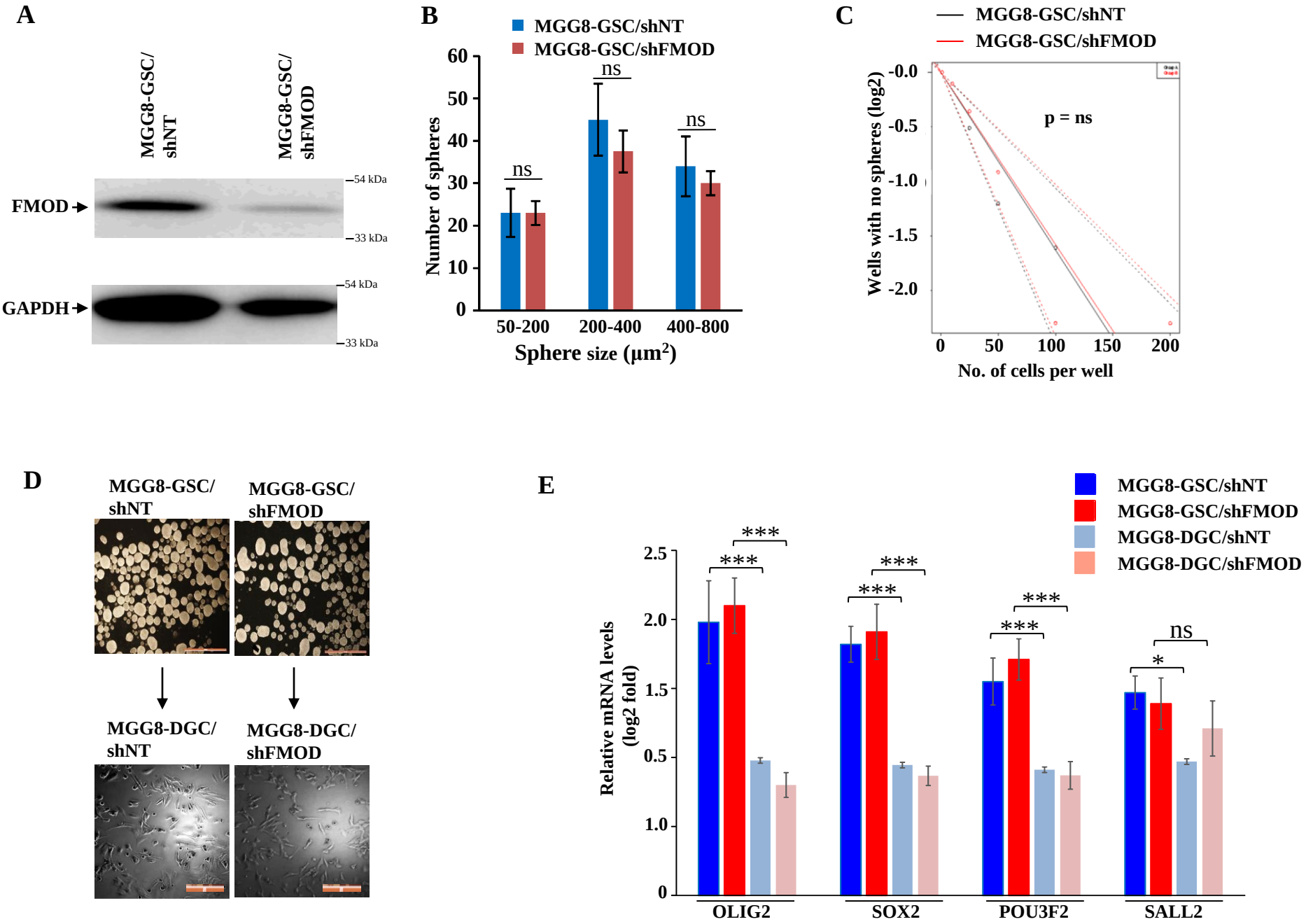
A
MGG8-GSC/ shNT
MGG8-GSC/ shFMOD
FMOD
54 kDa
33 kDa
GAPDH
54 kDa
33 kDa
B
MGG8-GSC/shNT
MGG8-GSC/shFMOD
Number of spheres
ns
ns
ns
50-200
200-400
400-800
Sphere size (µm²)
C
MGG8-GSC/shNT
MGG8-GSC/shFMOD
Wells with no spheres (log2)
p = ns
No. of cells per well
D
MGG8-GSC/ shNT
MGG8-GSC/ shFMOD
MGG8-DGC/ shNT
MGG8-DGC/ shFMOD
E
MGG8-GSC/shNT
MGG8-GSC/shFMOD
MGG8-DGC/shNT
MGG8-DGC/shFMOD
Relative mRNA levels (log2 fold)
OLIG2
SOX2
POU3F2
SALL2

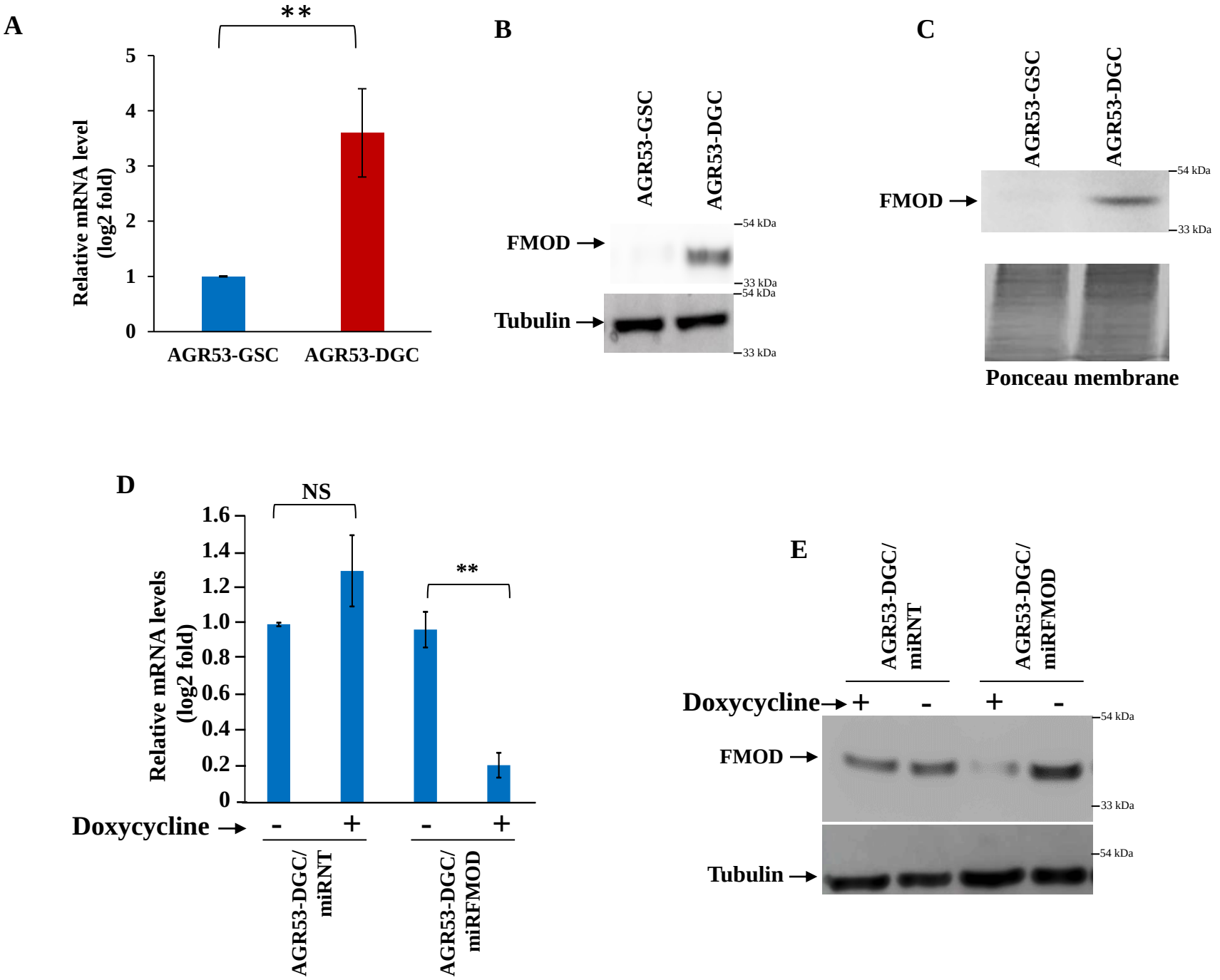
A
**
Relative mRNA level (log2 fold)
5
4
3
2
1
0
AGR53-GSC
AGR53-DGC
B
AGR53-GSC
AGR53-DGC
FMOD
54 kDa
33 kDa
54 kDa
Tubulin
33 kDa
C
AGR53-GSC
AGR53-DGC
FMOD
54 kDa
33 kDa
Ponceau membrane
D
NS
**
Relative mRNA levels (log2 fold)
1.6
1.4
1.2
1.0
0.8
0.6
0.4
0.2
0
Doxycycline
-
+
-
+
AGR53-DGC/ miRNT
AGR53-DGC/ miRFMOD
E
AGR53-DGC/ miRNT
AGR53-DGC/ miRFMOD
Doxycycline
+
-
+
-
FMOD
54 kDa
33 kDa
Tubulin
54 kDa

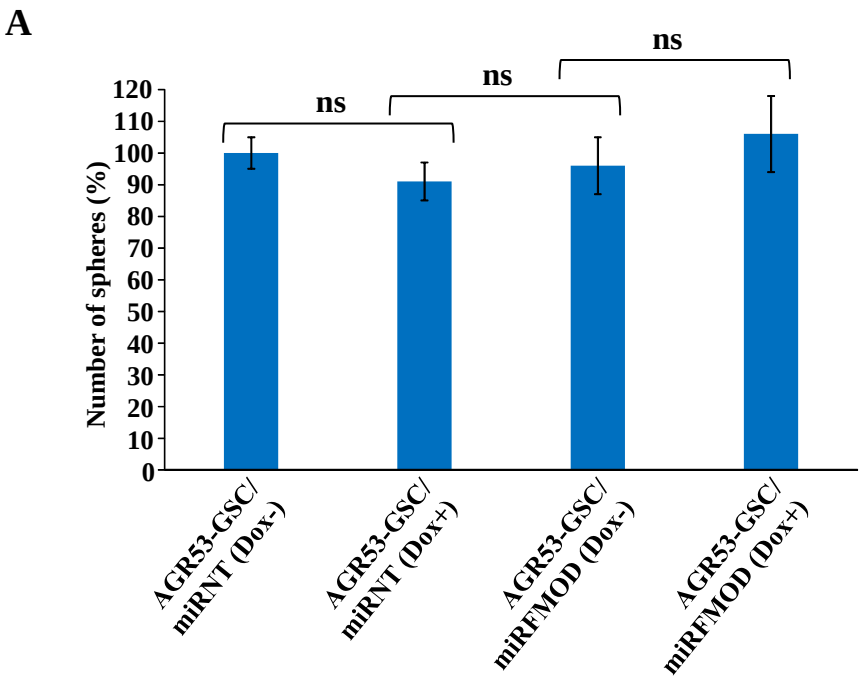
A
ns
ns
ns
Number of spheres (%)
120
110
100
90
80
70
60
50
40
30
20
10
0
AGR53-GSC/ miRNT (Dox-)
AGR53-GSC/ miRNT (Dox+)
AGR53-GSC/ miRFMOD (Dox-)
AGR53-GSC/ miRFMOD (Dox+)

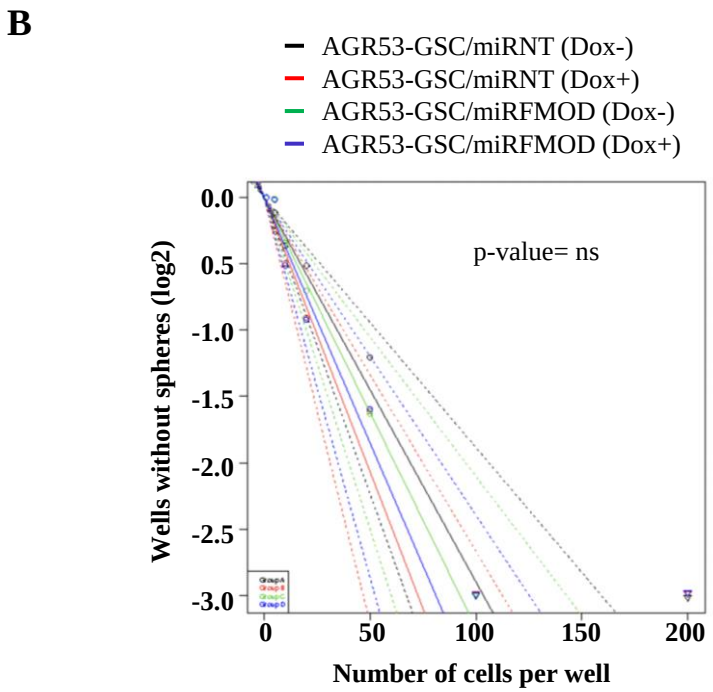
B
AGR53-GSC/miRNT (Dox-)
AGR53-GSC/miRNT (Dox+)
AGR53-GSC/miRFMOD (Dox-)
AGR53-GSC/miRFMOD (Dox+)
p-value= ns
Wells without spheres (log2)
0.0
0.5
-1.0
-1.5
-2.0
-2.5
-3.0
0
50
100
150
200
Number of cells per well

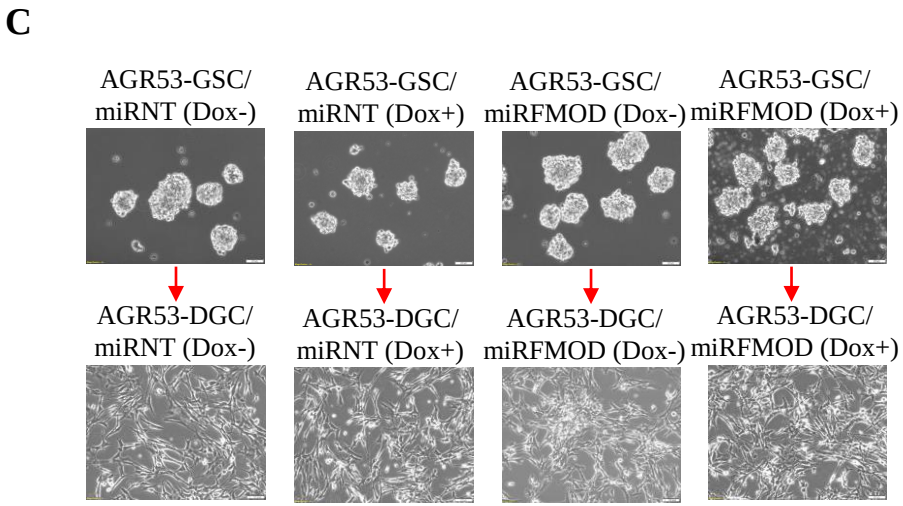
C
AGR53-GSC/ miRNT (Dox-)
AGR53-GSC/ miRNT (Dox+)
AGR53-GSC/ miRFMOD (Dox-)
AGR53-GSC/ miRFMOD (Dox+)
AGR53-DGC/ miRNT (Dox-)
AGR53-DGC/ miRNT (Dox+)
AGR53-DGC/ miRFMOD (Dox-)
AGR53-DGC/ miRFMOD (Dox+)

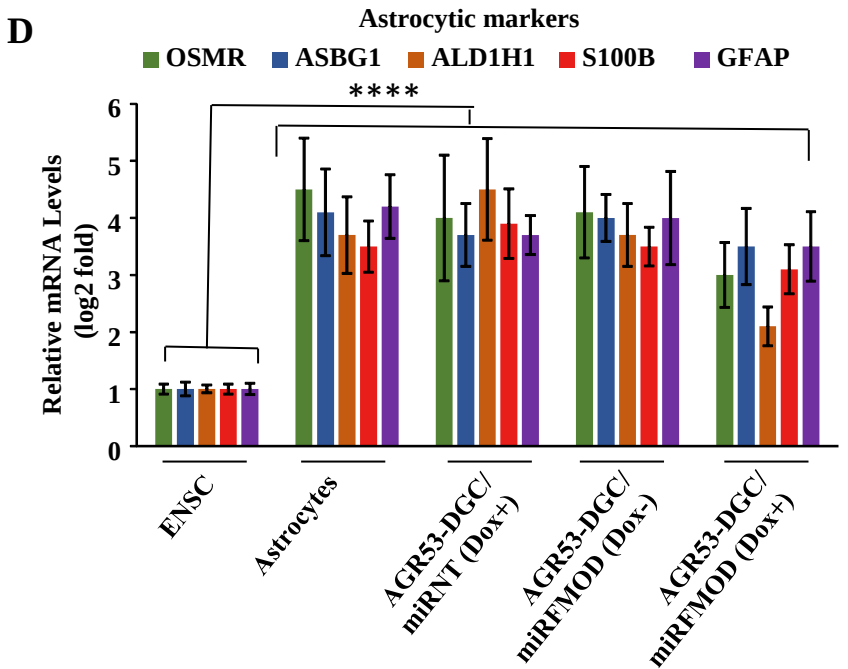
D
Astrocytic markers
OSMR
ASBG1
ALD1H1
S100B
GFAP
****
Relative mRNA Levels (log2 fold)
6
5
4
3
2
1
0
ENSC
Astrocytes
AGR53-DGC/ miRNT (Dox+)
AGR53-DGC/ miRFMOD (Dox-)
AGR53-DGC/ miRFMOD (Dox+)

A

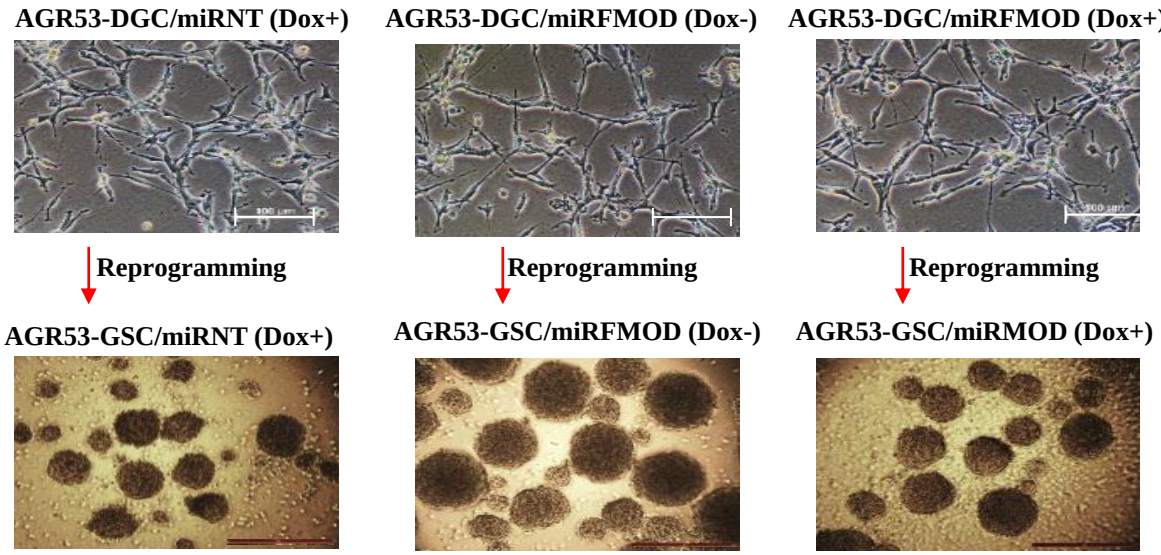
AGR53-DGC/miRNT (Dox+)
AGR53-DGC/miRFMOD (Dox-)
AGR53-DGC/miRFMOD (Dox+)
Reprogramming
Reprogramming
Reprogramming
AGR53-GSC/miRNT (Dox+)
AGR53-GSC/miRFMOD (Dox-)
AGR53-GSC/miRMOD (Dox+)

B

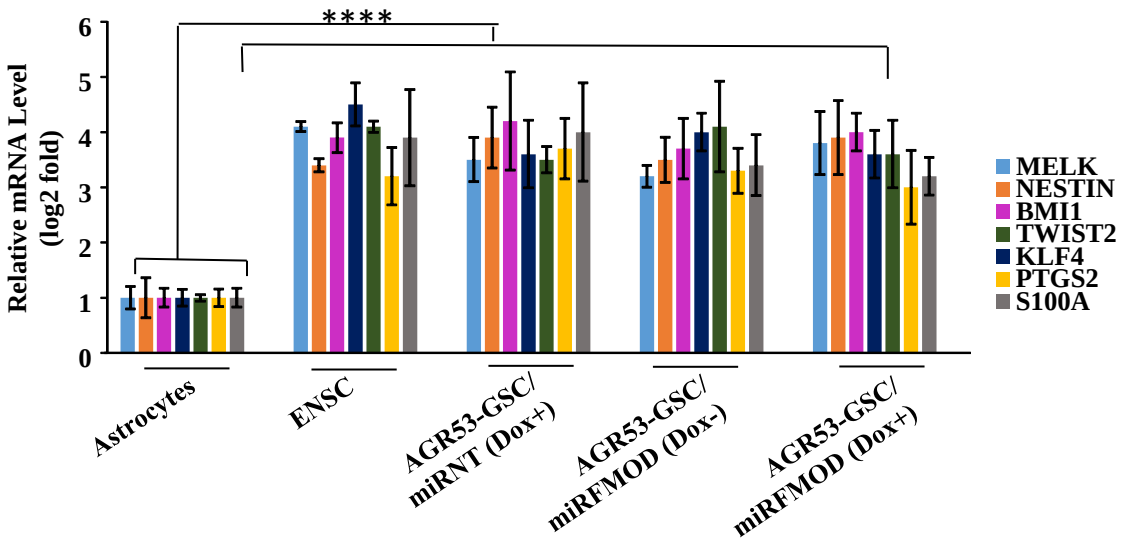
****
Relative mRNA Level (log2 fold)
0
1
2
3
4
5
6
Astrocytes
ENSC
AGR53-GSC/ miRNT (Dox+)
AGR53-GSC/ miRFMOD (Dox-)
AGR53-GSC/ miRFMOD (Dox+)
MELK
NESTIN
BMI1
TWIST2
KLF4
PTGS2
S100A

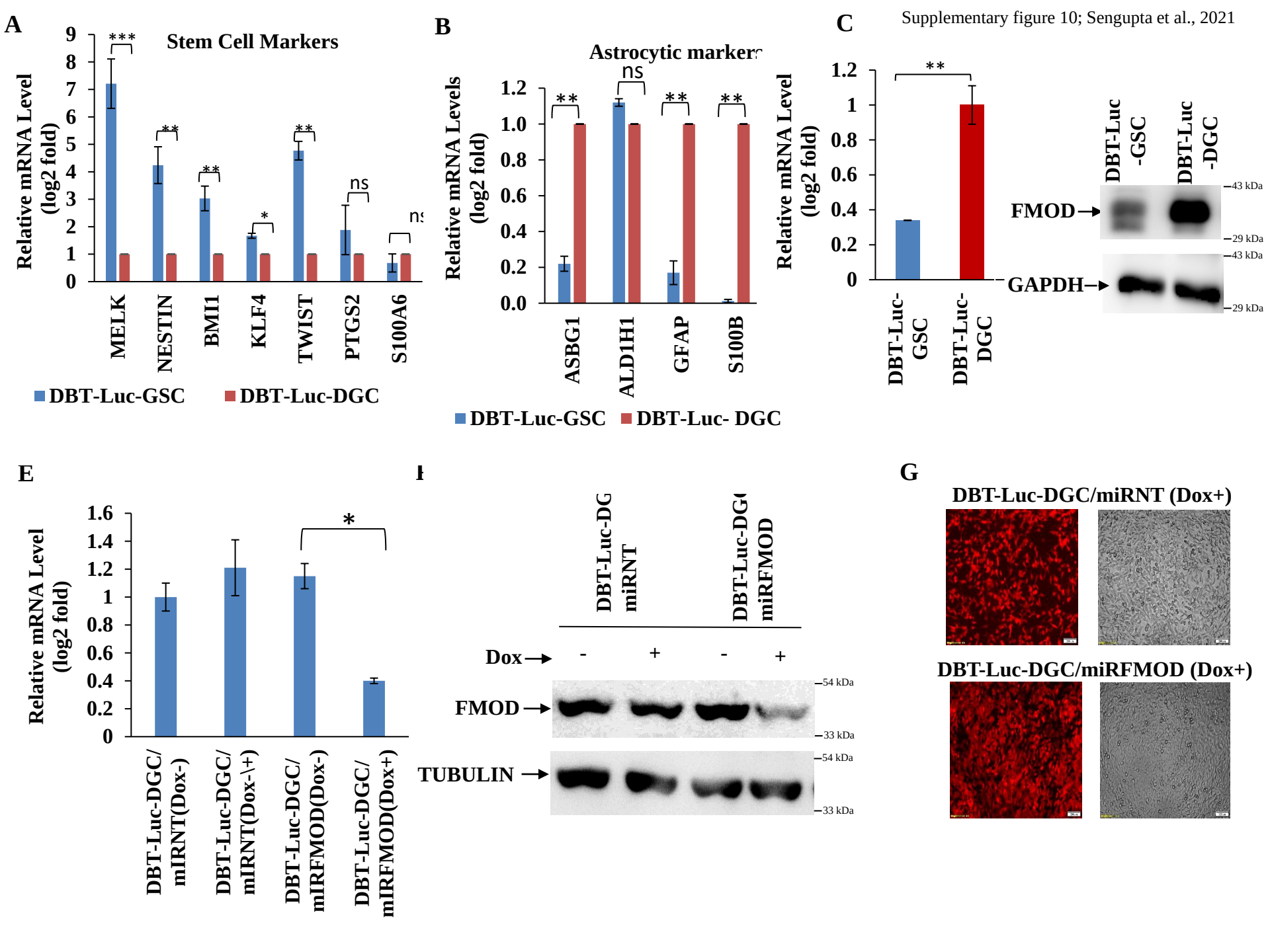
A
Stem Cell Markers
Relative mRNA Level (log2 fold)
MELK
NESTIN
BMI1
KLF4
TWIST
PTGS2
S100A6
DBT-Luc-GSC
DBT-Luc-DGC
B
Astrocytic markers
Relative mRNA Levels (log2 fold)
ASBG1
ALD1H1
GFAP
S100B
DBT-Luc-GSC
DBT-Luc- DGC
C
Relative mRNA Level (log2 fold)
DBT-Luc-GSC
DBT-Luc-DGC
DBT-Luc -GSC
DBT-Luc -DGC
FMOD
GAPDH
43 kDa
29 kDa
E
Relative mRNA Level (log2 fold)
DBT-Luc-DGC/ mIRNT(Dox-)
DBT-Luc-DGC/ mIRNT(Dox-\+)
DBT-Luc-DGC/ mIRFMOD(Dox-)
DBT-Luc-DGC/ mIRFMOD(Dox+)
F
DBT-Luc-DG miRNT
DBT-Luc-DG miRFMOD
Dox
FMOD
TUBULIN
54 kDa
33 kDa
G
DBT-Luc-DGC/miRNT (Dox+)
DBT-Luc-DGC/miRFMOD (Dox+)

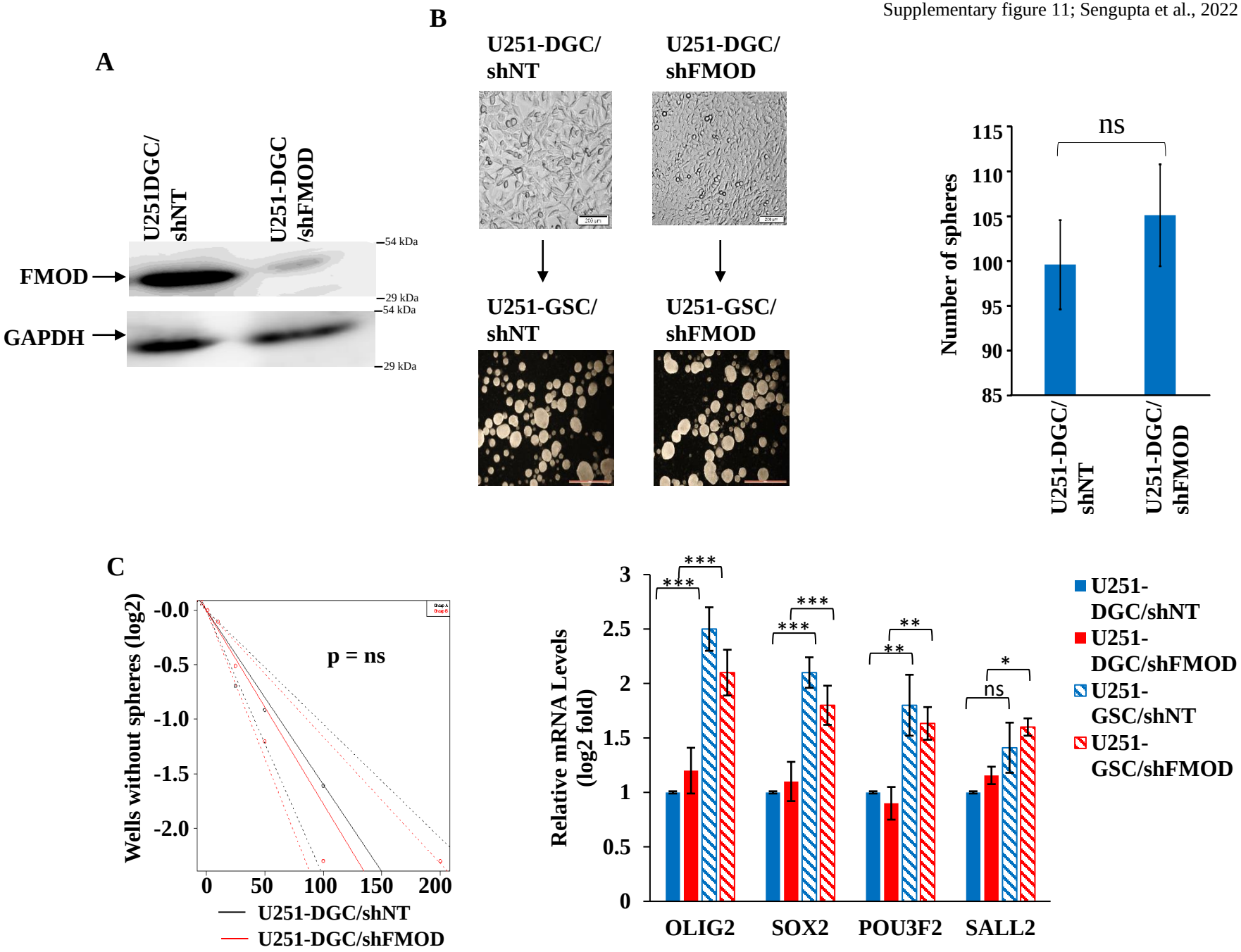
A
U251DGC/ shNT
U251-DGC /shFMOD
FMOD
GAPDH
54 kDa
29 kDa
54 kDa
29 kDa
B
U251-DGC/ shNT
U251-DGC/ shFMOD
U251-GSC/ shNT
U251-GSC/ shFMOD
ns
Number of spheres
115
110
105
100
95
90
85
U251-DGC/ shNT
U251-DGC/ shFMOD
C
Wells without spheres (log2)
-0.0
-0.5
-1.0
-1.5
-2.0
p = ns
0
50
100
150
200
U251-DGC/shNT
U251-DGC/shFMOD
Relative mRNA Levels (log2 fold)
3
2.5
2
1.5
1
0.5
0
***
***
***
***
**
**
*
ns
OLIG2
SOX2
POU3F2
SALL2
U251-DGC/shNT
U251-DGC/shFMOD
U251-GSC/shNT
U251-GSC/shFMOD

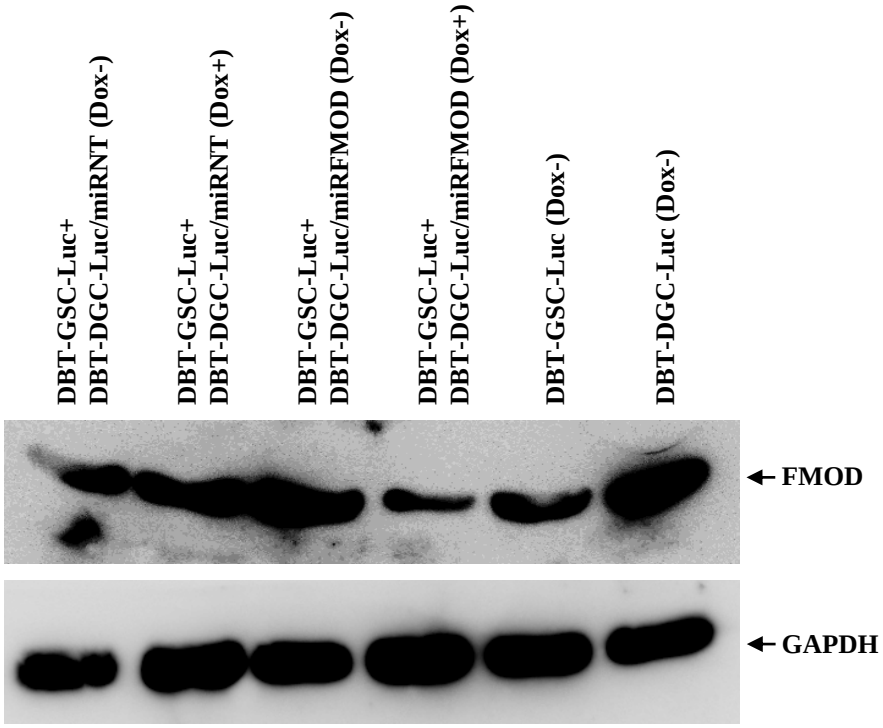
DBT-GSC-Luc+
DBT-DGC-Luc/miRNT (Dox-)
DBT-GSC-Luc+
DBT-DGC-Luc/miRNT (Dox+)
DBT-GSC-Luc+
DBT-DGC-Luc/miRFMOD (Dox-)
DBT-GSC-Luc+
DBT-DGC-Luc/miRFMOD (Dox+)
DBT-GSC-Luc (Dox-)
DBT-DGC-Luc (Dox-)
FMOD
GAPDH

Supplementary figures 13 to 22

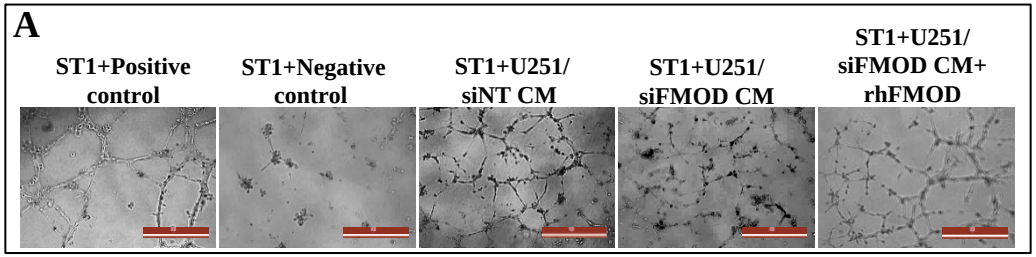
A
ST1+Positive control
ST1+Negative control
ST1+U251/ siNT CM
ST1+U251/ siFMOD CM
ST1+U251/ siFMOD CM+ rhFMOD

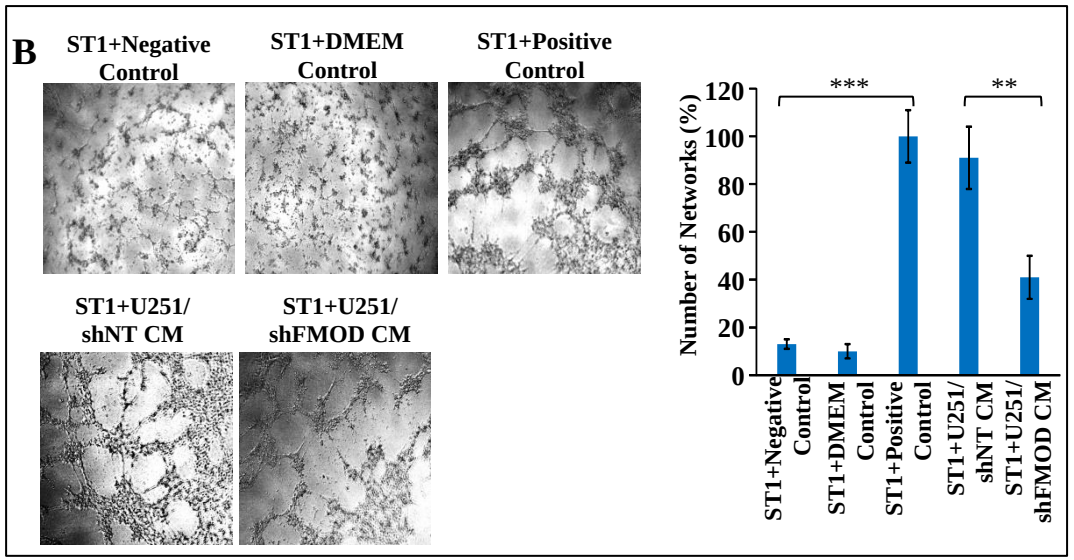
B
ST1+Negative Control
ST1+DMEM Control
ST1+Positive Control
ST1+U251/ shNT CM
ST1+U251/ shFMOD CM
Number of Networks (%)
0
20
40
60
80
100
120
***
**
ST1+Negative Control
ST1+DMEM Control
ST1+Positive Control
ST1+U251/ shNT CM
ST1+U251/ shFMOD CM

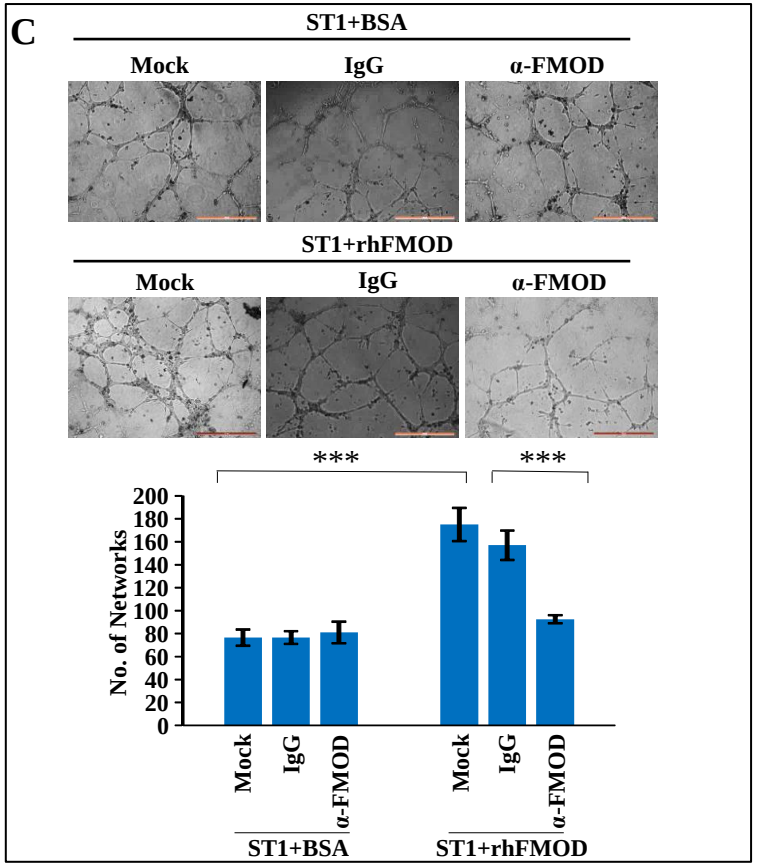
C
ST1+BSA
Mock
IgG
α-FMOD
ST1+rhFMOD
Mock
IgG
α-FMOD
No. of Networks
0
20
40
60
80
100
120
140
160
180
200
***
***
Mock
IgG
α-FMOD
Mock
IgG
α-FMOD
ST1+BSA
ST1+rhFMOD

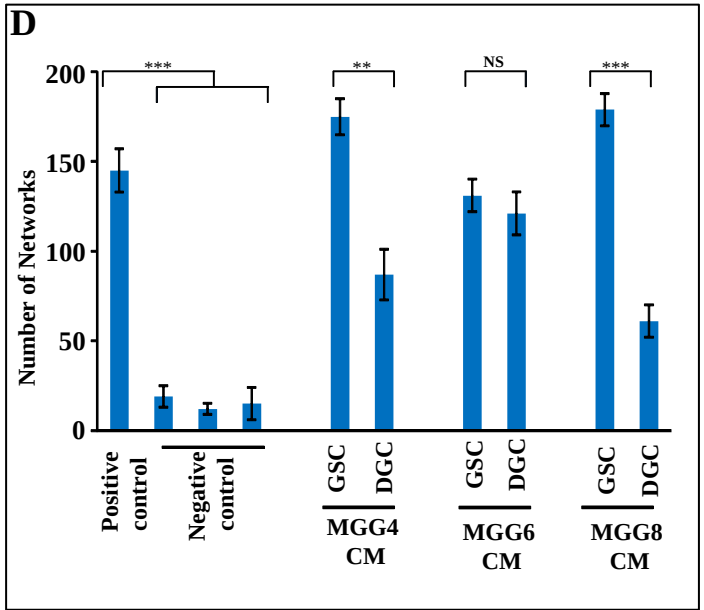
D
Number of Networks
0
50
100
150
200
***
***
**
NS
***
Positive control
Negative control
GSC
DGC
MGG4 CM
GSC
DGC
MGG6 CM
GSC
DGC
MGG8 CM

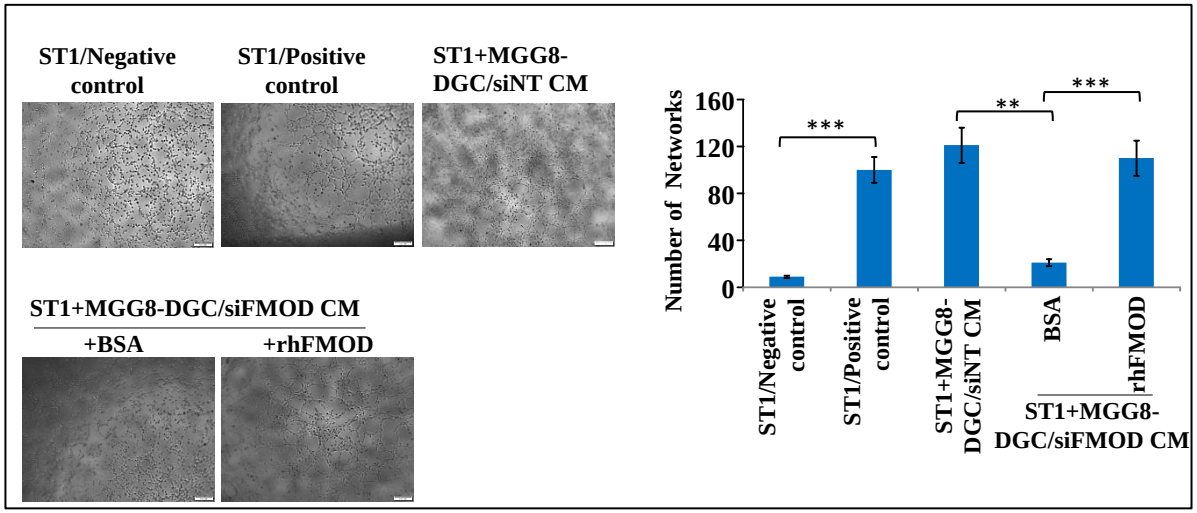
E
ST1/Negative control
ST1/Positive control
ST1+MGG8-DGC/siNT CM
ST1+MGG8-DGC/siFMOD CM
+BSA
+rhFMOD
Number of Networks
0
40
80
120
160
***
**
***
ST1/Negative control
ST1/Positive control
ST1+MGG8-DGC/siNT CM
BSA
rhFMOD
ST1+MGG8-DGC/siFMOD CM

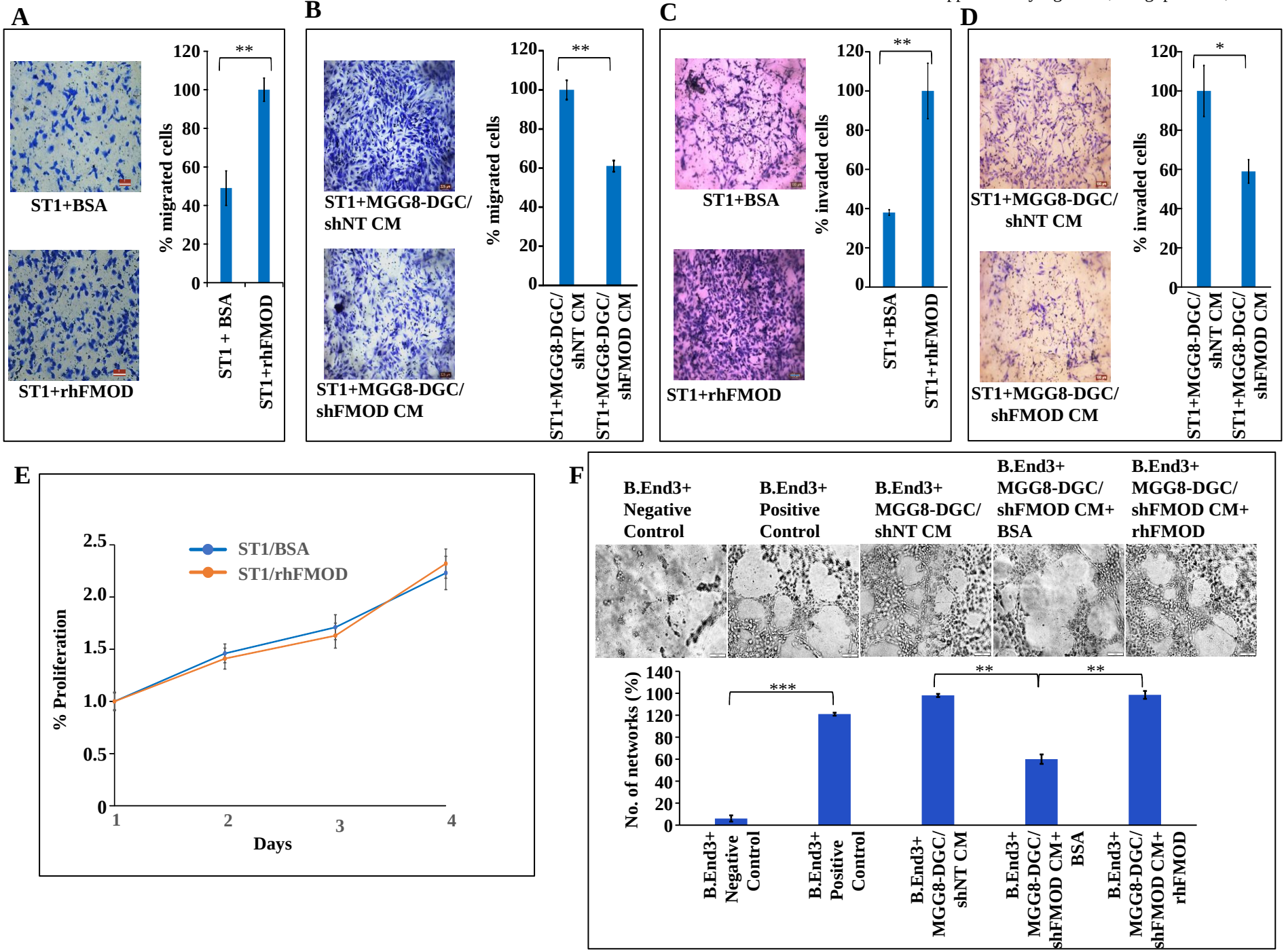
A
ST1+BSA
ST1+rhFMOD
% migrated cells
120
100
80
60
40
20
0
**
ST1 + BSA
ST1+rhFMOD
B
ST1+MGG8-DGC/ shNT CM
ST1+MGG8-DGC/ shFMOD CM
% migrated cells
**
ST1+MGG8-DGC/ shNT CM
ST1+MGG8-DGC/ shFMOD CM
C
ST1+BSA
ST1+rhFMOD
% invaded cells
**
ST1+BSA
ST1+rhFMOD
D
ST1+MGG8-DGC/ shNT CM
ST1+MGG8-DGC/ shFMOD CM
% invaded cells
*
ST1+MGG8-DGC/ shNT CM
ST1+MGG8-DGC/ shFMOD CM
E
% Proliferation
2.5
2.0
1.5
1.0
0.5
0
ST1/BSA
ST1/rhFMOD
1
2
3
4
Days
F
B.End3+ Negative Control
B.End3+ Positive Control
B.End3+ MGG8-DGC/ shNT CM
B.End3+ MGG8-DGC/ shFMOD CM+ BSA
B.End3+ MGG8-DGC/ shFMOD CM+ rhFMOD
No. of networks (%)
140
100
120
80
60
40
20
0
***
**
**
B.End3+ Negative Control
B.End3+ Positive Control
B.End3+ MGG8-DGC/ shNT CM
B.End3+ MGG8-DGC/ shFMOD CM+ BSA
B.End3+ MGG8-DGC/ shFMOD CM+ rhFMOD

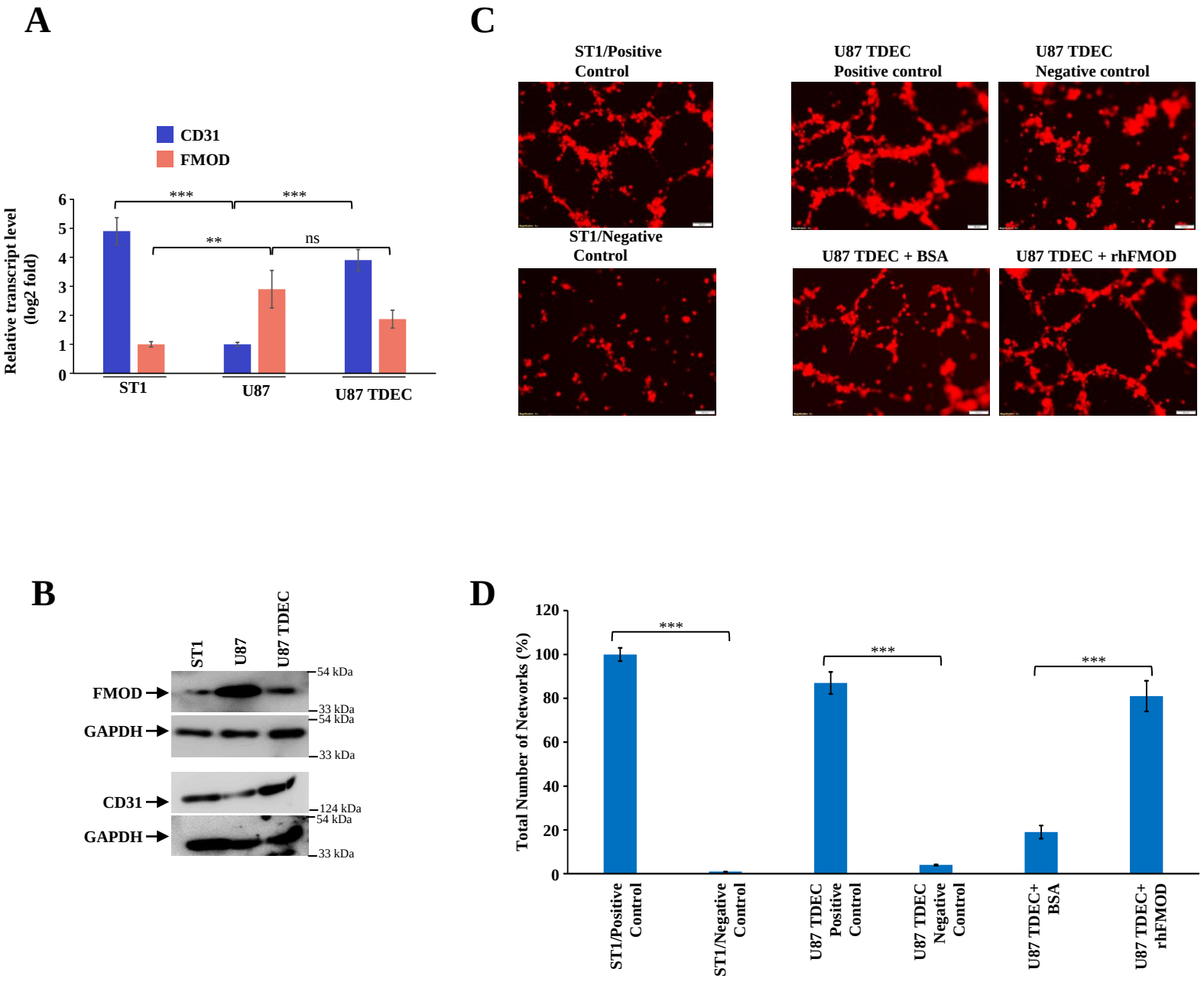
A
CD31
FMOD
Relative transcript level (log2 fold)
***
***
**
ns
ST1
U87
U87 TDEC
B
ST1
U87
U87 TDEC
FMOD
GAPDH
CD31
GAPDH
54 kDa
33 kDa
54 kDa
33 kDa
124 kDa
54 kDa
33 kDa
C
ST1/Positive Control
U87 TDEC Positive control
U87 TDEC Negative control
ST1/Negative Control
U87 TDEC + BSA
U87 TDEC + rhFMOD
D
Total Number of Networks (%)
***
***
***
ST1/Positive Control
ST1/Negative Control
U87 TDEC Positive Control
U87 TDEC Negative Control
U87 TDEC+ BSA
U87 TDEC+ rhFMOD

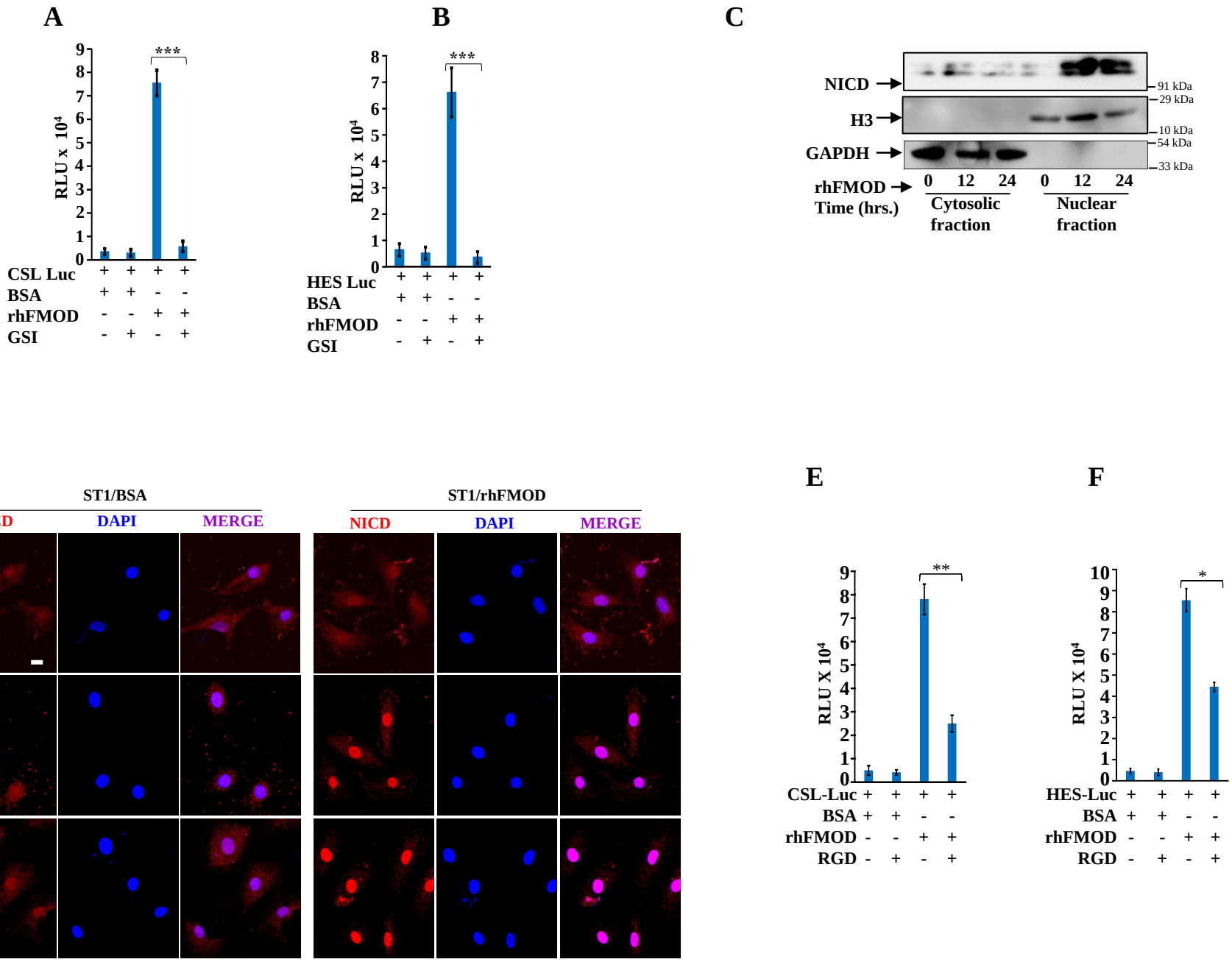
A
RLU x 10^4
***
CSL Luc + + + +
BSA + + - -
rhFMOD - - + +
GSI - + - +
B
RLU x 10^4
***
HES Luc + + + +
BSA + + - -
rhFMOD - - + +
GSI - + - +
C
NICD
H3
GAPDH
91 kDa
29 kDa
10 kDa
54 kDa
33 kDa
rhFMOD 0 12 24 0 12 24
Time (hrs.)
Cytosolic fraction
Nuclear fraction
D
Time (hrs)
ST1/BSA
ST1/rhFMOD
NICD
DAPI
MERGE
0
12
24
E
RLU X 10^4
**
CSL-Luc + + + +
BSA + + - -
rhFMOD - - + +
RGD - + - +
F
RLU X 10^4
*
HES-Luc + + + +
BSA + + - -
rhFMOD - - + +
RGD - + - +

A

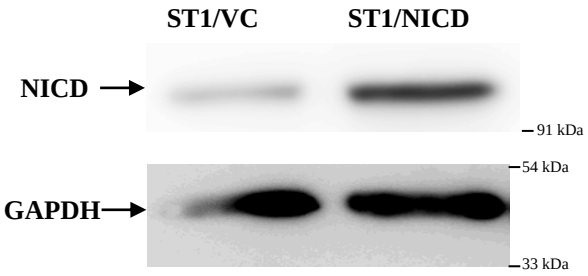
ST1/VC
ST1/NICD
NICD
91 kDa
54 kDa
GAPDH
33 kDa

B

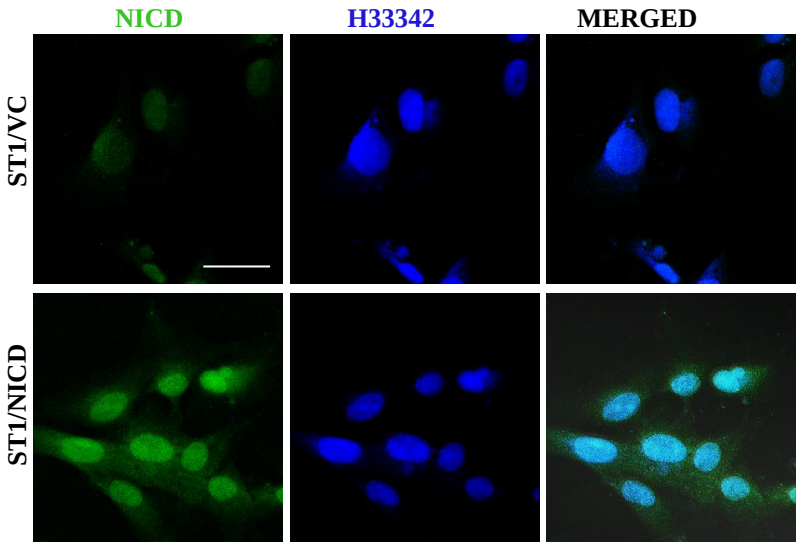
NICD
H33342
MERGED
ST1/VC
ST1/NICD

C

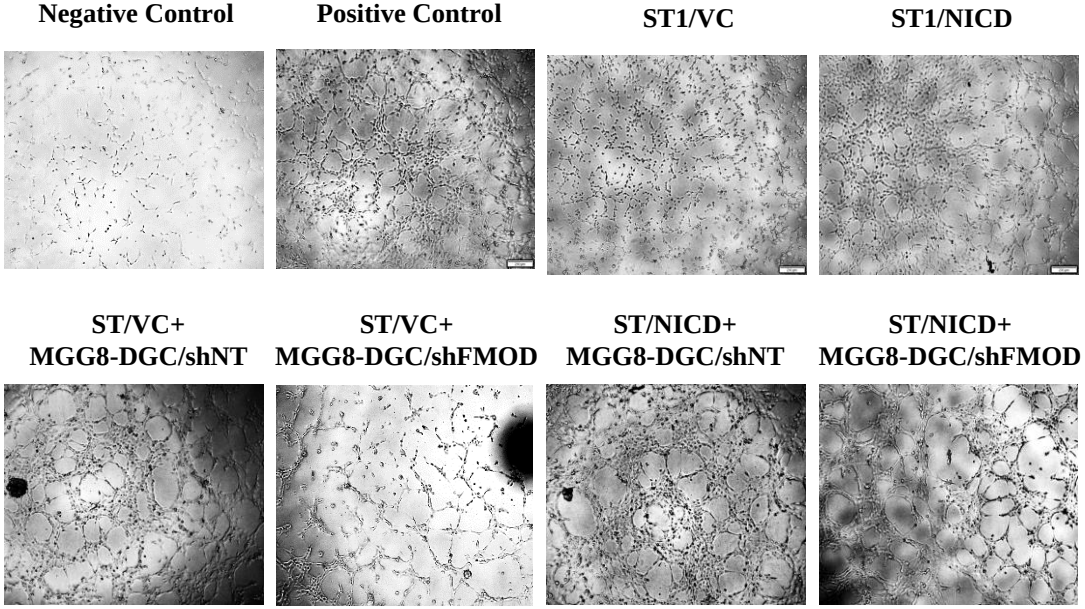
ST1+ Negative Control
ST1+ Positive Control
ST1/VC
ST1/NICD
ST/VC+ MGG8-DGC/shNT
ST/VC+ MGG8-DGC/shFMOD
ST/NICD+ MGG8-DGC/shNT
ST/NICD+ MGG8-DGC/shFMOD

D

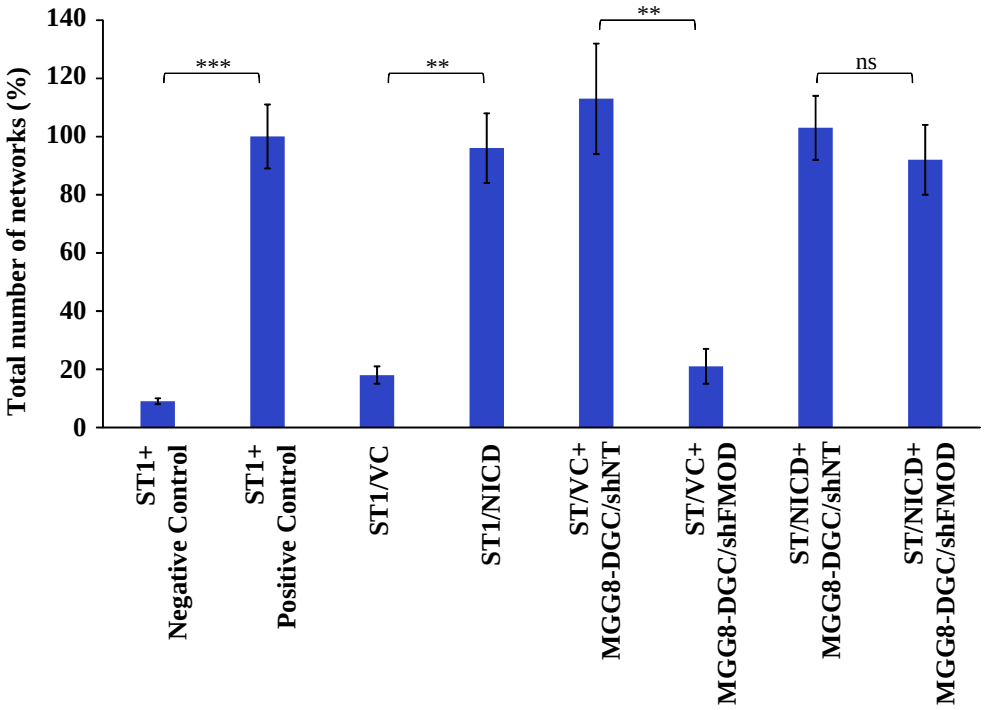
Total number of networks (%)
140
120
100
80
60
40
20
0
***
**
**
ns
ST1+ Negative Control
ST1+ Positive Control
ST1/VC
ST1/NICD
ST/VC+ MGG8-DGC/shNT
ST/VC+ MGG8-DGC/shFMOD
ST/NICD+ MGG8-DGC/shNT
ST/NICD+ MGG8-DGC/shFMOD

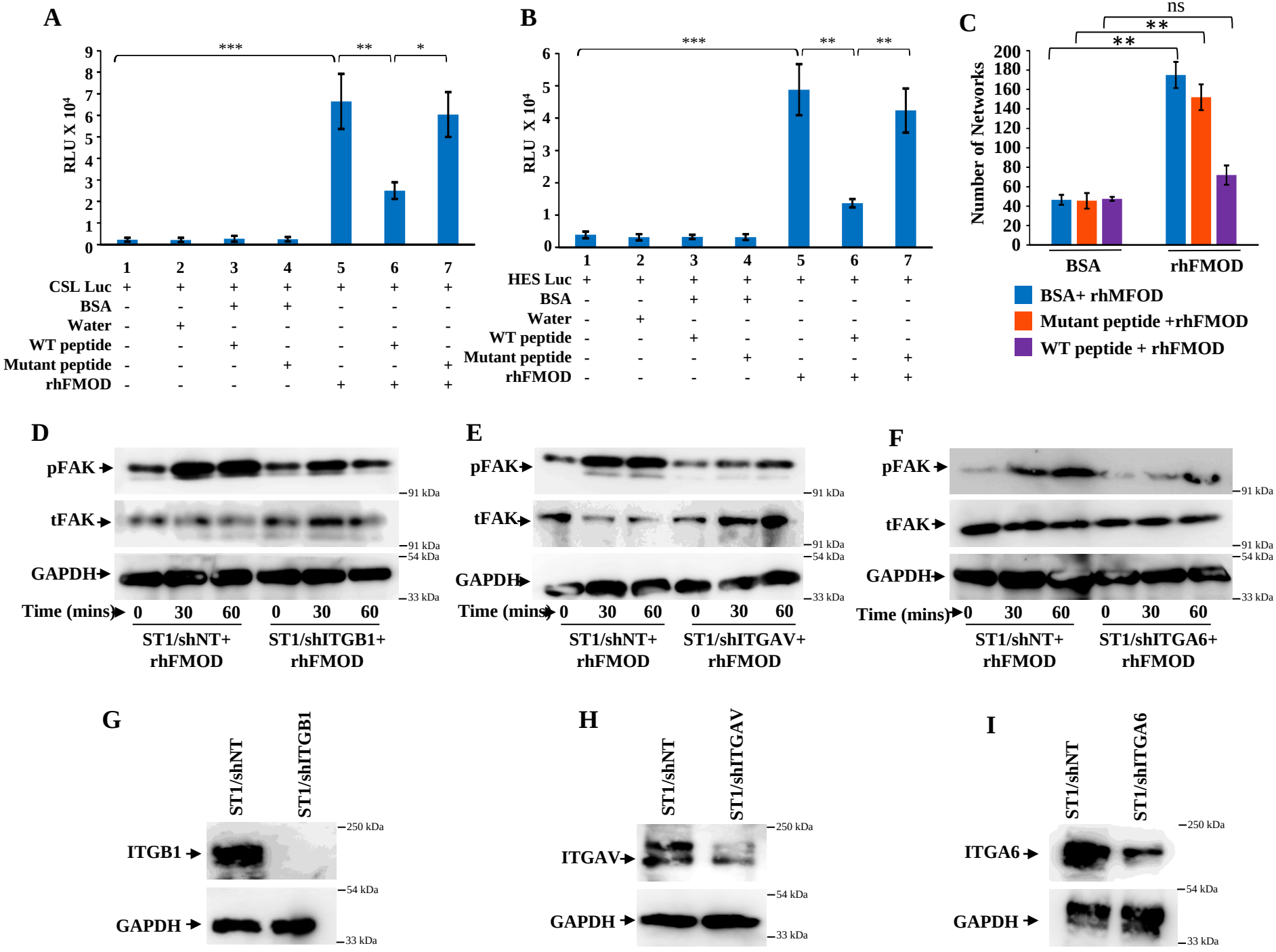
A
RLU X 10^4
***
**
*
1 2 3 4 5 6 7
CSL Luc + + + + + + +
BSA - - + + - - -
Water - + - - - - -
WT peptide - - + - - + -
Mutant peptide - - - + - - +
rhFMOD - - - - + + +
B
RLU X 10^4
***
**
**
1 2 3 4 5 6 7
HES Luc + + + + + + +
BSA - - + + - - -
Water - + - - - - -
WT peptide - - + - - + -
Mutant peptide - - - + - - +
rhFMOD - - - - + + +
C
ns
**
**
Number of Networks
BSA
rhFMOD
BSA+ rhMFOD
Mutant peptide +rhFMOD
WT peptide + rhFMOD
D
pFAK
tFAK
GAPDH
91 kDa
91 kDa
54 kDa
33 kDa
Time (mins) 0 30 60 0 30 60
ST1/shNT+ rhFMOD
ST1/shITGB1+ rhFMOD
E
pFAK
tFAK
GAPDH
91 kDa
91 kDa
54 kDa
33 kDa
Time (mins) 0 30 60 0 30 60
ST1/shNT+ rhFMOD
ST1/shITGAV+ rhFMOD
F
pFAK
tFAK
GAPDH
91 kDa
91 kDa
54 kDa
33 kDa
Time (mins) 0 30 60 0 30 60
ST1/shNT+ rhFMOD
ST1/shITGA6+ rhFMOD
G
ST1/shNT
ST1/shITGB1
ITGB1
GAPDH
250 kDa
54 kDa
33 kDa
H
ST1/shNT
ST1/shITGAV
ITGAV
GAPDH
250 kDa
54 kDa
33 kDa
I
ST1/shNT
ST1/shITGA6
ITGA6
GAPDH
250 kDa
54 kDa
33 kDa

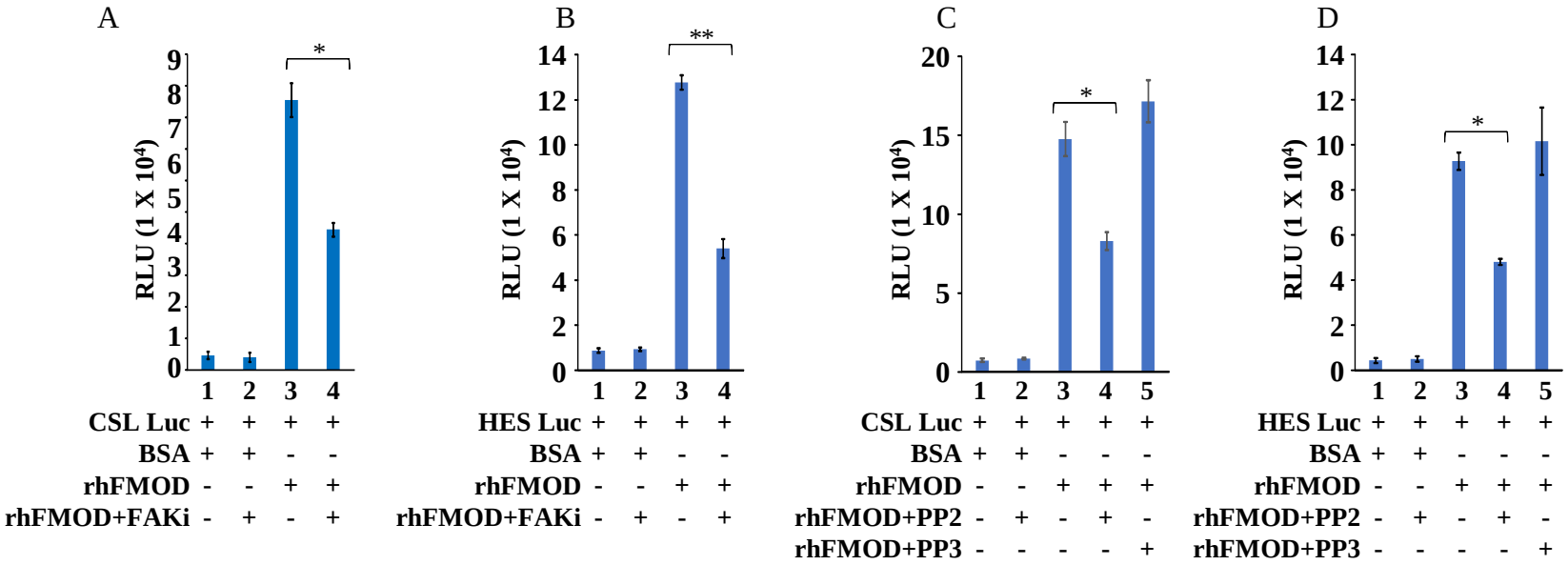
A
RLU (1 X 10⁴)
*
1 2 3 4
CSL Luc + + + +
BSA + + - -
rhFMOD - - + +
rhFMOD+FAKi - + - +
B
RLU (1 X 10⁴)
**
1 2 3 4
HES Luc + + + +
BSA + + - -
rhFMOD - - + +
rhFMOD+FAKi - + - +
C
RLU (1 X 10⁴)
*
1 2 3 4 5
CSL Luc + + + + +
BSA + + - - -
rhFMOD - - + + +
rhFMOD+PP2 - + - + -
rhFMOD+PP3 - - - - +
D
RLU (1 X 10⁴)
*
1 2 3 4 5
HES Luc + + + + +
BSA + + - - -
rhFMOD - - + + +
rhFMOD+PP2 - + - + -
rhFMOD+PP3 - - - - +

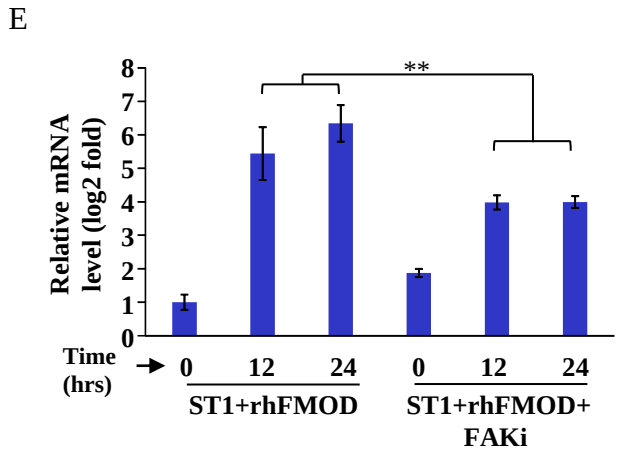
E
Relative mRNA level (log2 fold)
**
Time (hrs)
0 12 24 0 12 24
ST1+rhFMOD
ST1+rhFMOD+ FAKi

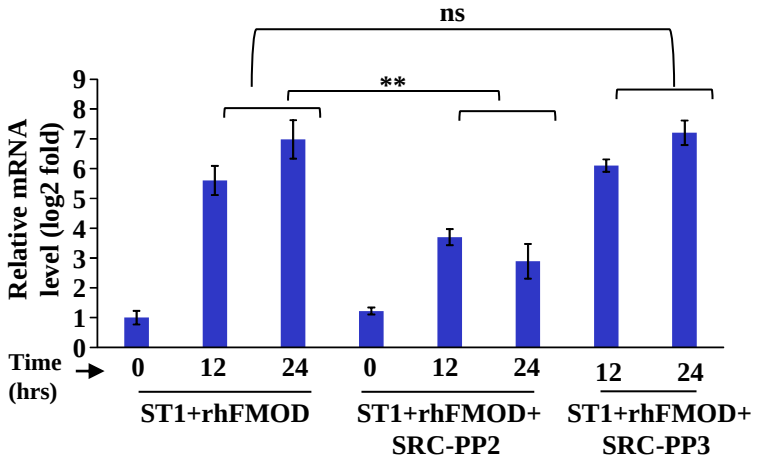
G
Relative mRNA level (log2 fold)
ns
**
Time (hrs)
0 12 24 0 12 24 12 24
ST1+rhFMOD
ST1+rhFMOD+ SRC-PP2
ST1+rhFMOD+ SRC-PP3

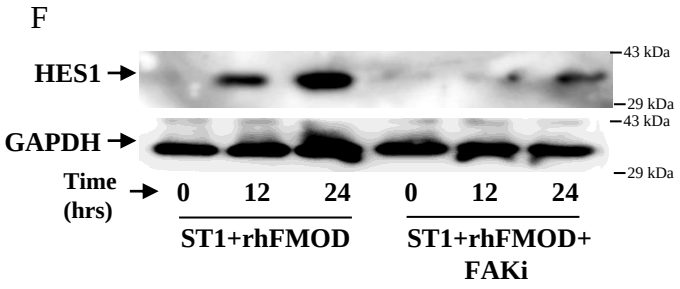
F
HES1
GAPDH
43 kDa
29 kDa
43 kDa
29 kDa
Time (hrs)
0 12 24 0 12 24
ST1+rhFMOD
ST1+rhFMOD+ FAKi

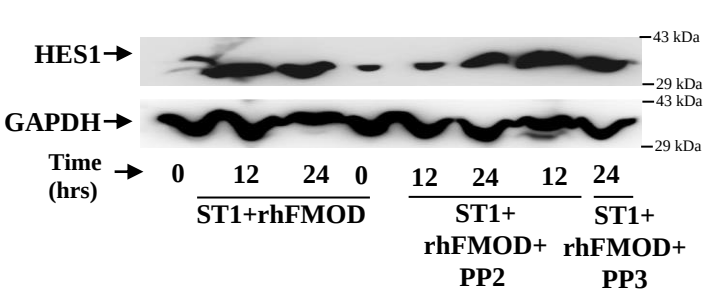
H
HES1
GAPDH
43 kDa
29 kDa
43 kDa
29 kDa
Time (hrs)
0 12 24 0 12 24 12 24
ST1+rhFMOD
ST1+ rhFMOD+ PP2
ST1+ rhFMOD+ PP3

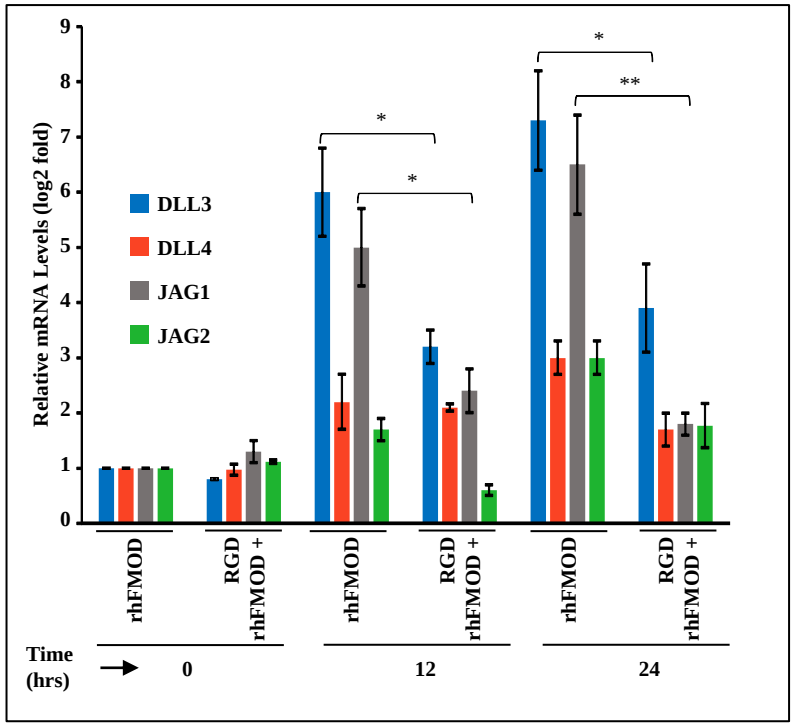
A
Relative mRNA Levels (log2 fold)
DLL3
DLL4
JAG1
JAG2
rhFMOD
RGD + rhFMOD
Time (hrs)
0
12
24

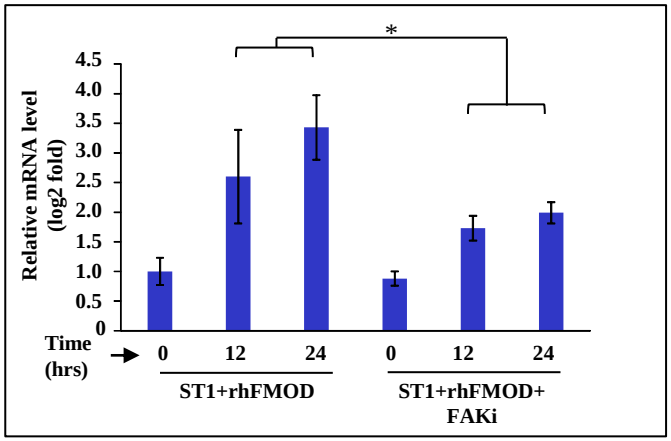
B
Relative mRNA level (log2 fold)
Time (hrs)
ST1+rhFMOD
ST1+rhFMOD+ FAKi

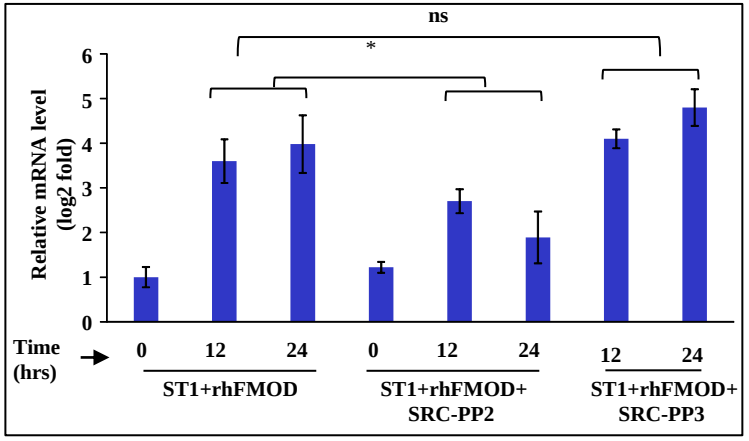
C
Relative mRNA level (log2 fold)
ns
Time (hrs)
ST1+rhFMOD
ST1+rhFMOD+ SRC-PP2
ST1+rhFMOD+ SRC-PP3

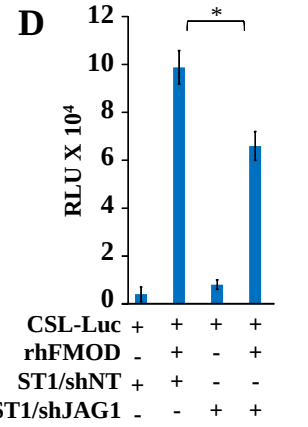
D
RLU X 10^4
CSL-Luc
rhFMOD
ST1/shNT
ST1/shJAG1

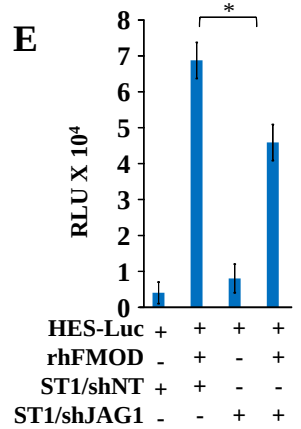
E
RLU X 10^4
HES-Luc
rhFMOD
ST1/shNT
ST1/shJAG1

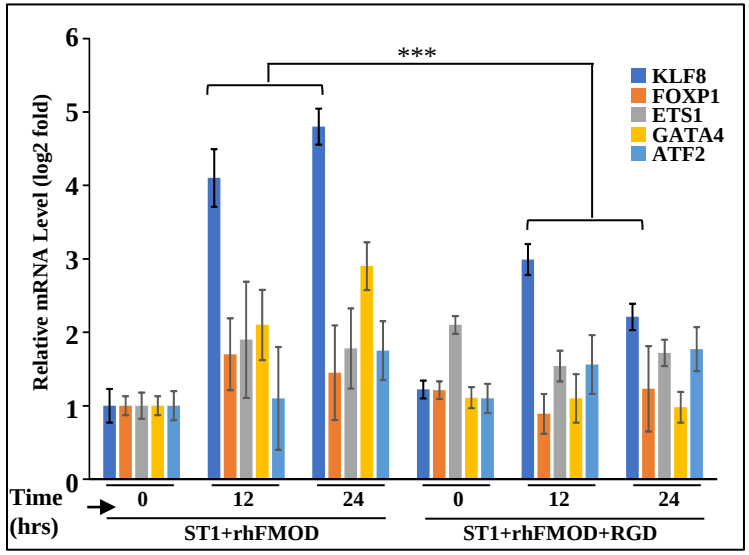
F
Relative mRNA Level (log2 fold)
KLF8
FOXP1
ETS1
GATA4
ATF2
Time (hrs)
ST1+rhFMOD
ST1+rhFMOD+RGD

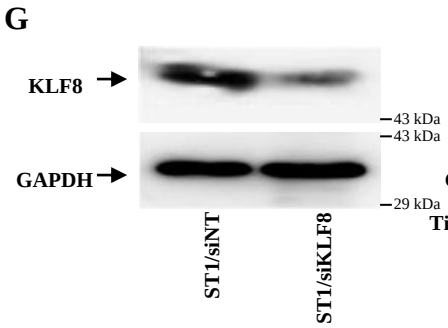
G
KLF8
GAPDH
43 kDa
43 kDa
29 kDa
ST1/siNT
ST1/siKLF8

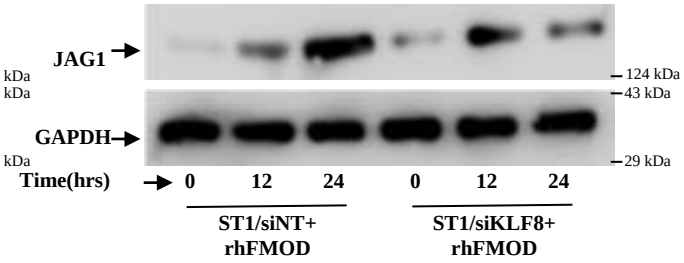
H
JAG1
GAPDH
124 kDa
43 kDa
29 kDa
Time(hrs)
ST1/siNT+ rhFMOD
ST1/siKLF8+ rhFMOD

Supplementary figure 21; Sengupta et al., 2022

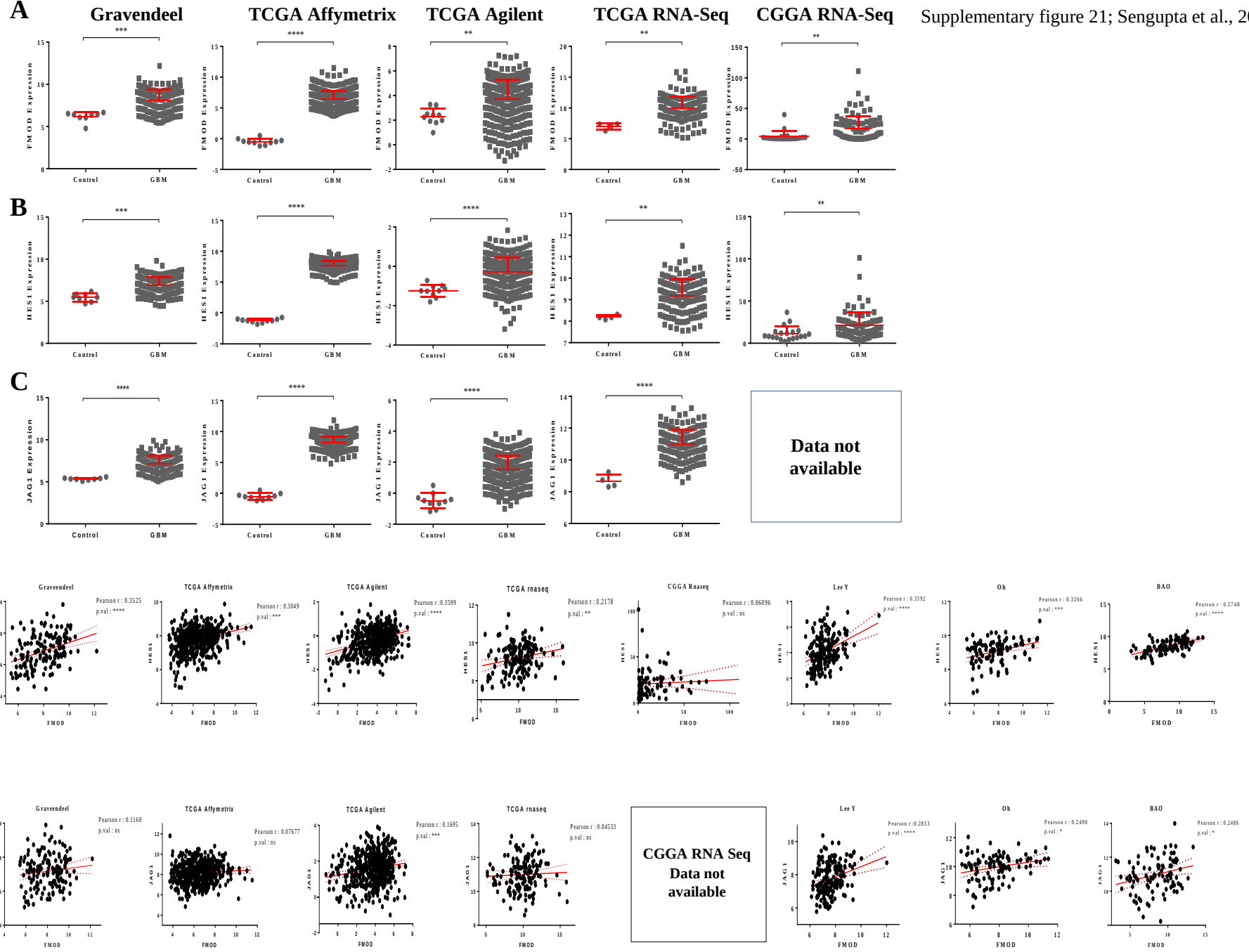

A

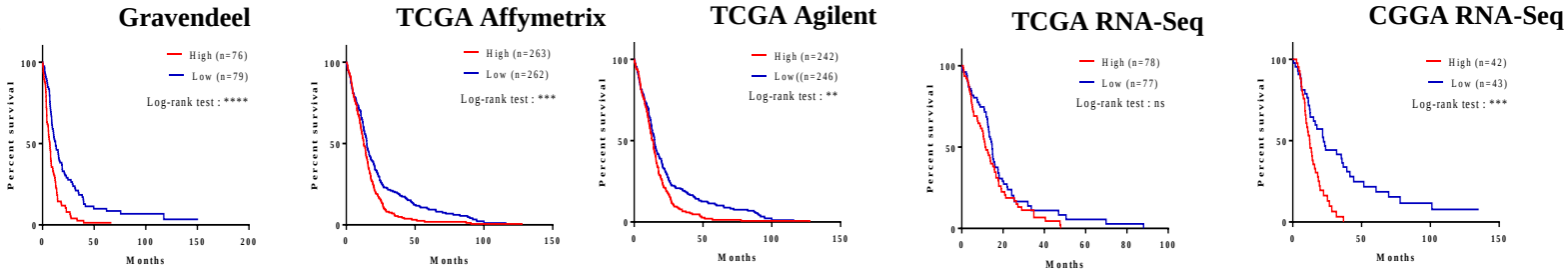
Gravendeel
High (n=76)
Low (n=79)
Log-rank test : ****
TCGA Affymetrix
High (n=263)
Low (n=262)
Log-rank test : ***
TCGA Agilent
High (n=242)
Low((n=246)
Log-rank test : **
TCGA RNA-Seq
High (n=78)
Low (n=77)
Log-rank test : ns
CGGA RNA-Seq
High (n=42)
Low (n=43)
Log-rank test : ***
Percent survival
Months

B

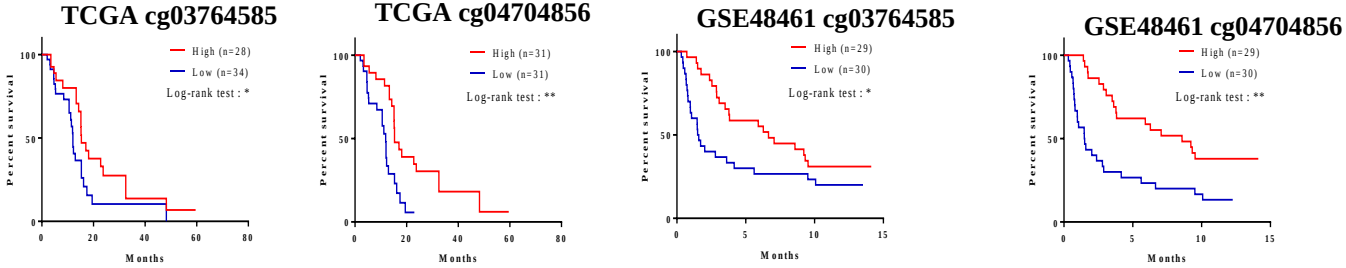
TCGA cg03764585
High (n=28)
Low (n=34)
Log-rank test : *
TCGA cg04704856
High (n=31)
Low (n=31)
Log-rank test : **
GSE48461 cg03764585
High (n=29)
Low (n=30)
Log-rank test : *
GSE48461 cg04704856
High (n=29)
Low (n=30)
Log-rank test : **
Percent survival
Months

Supplementary figures 23 to 28

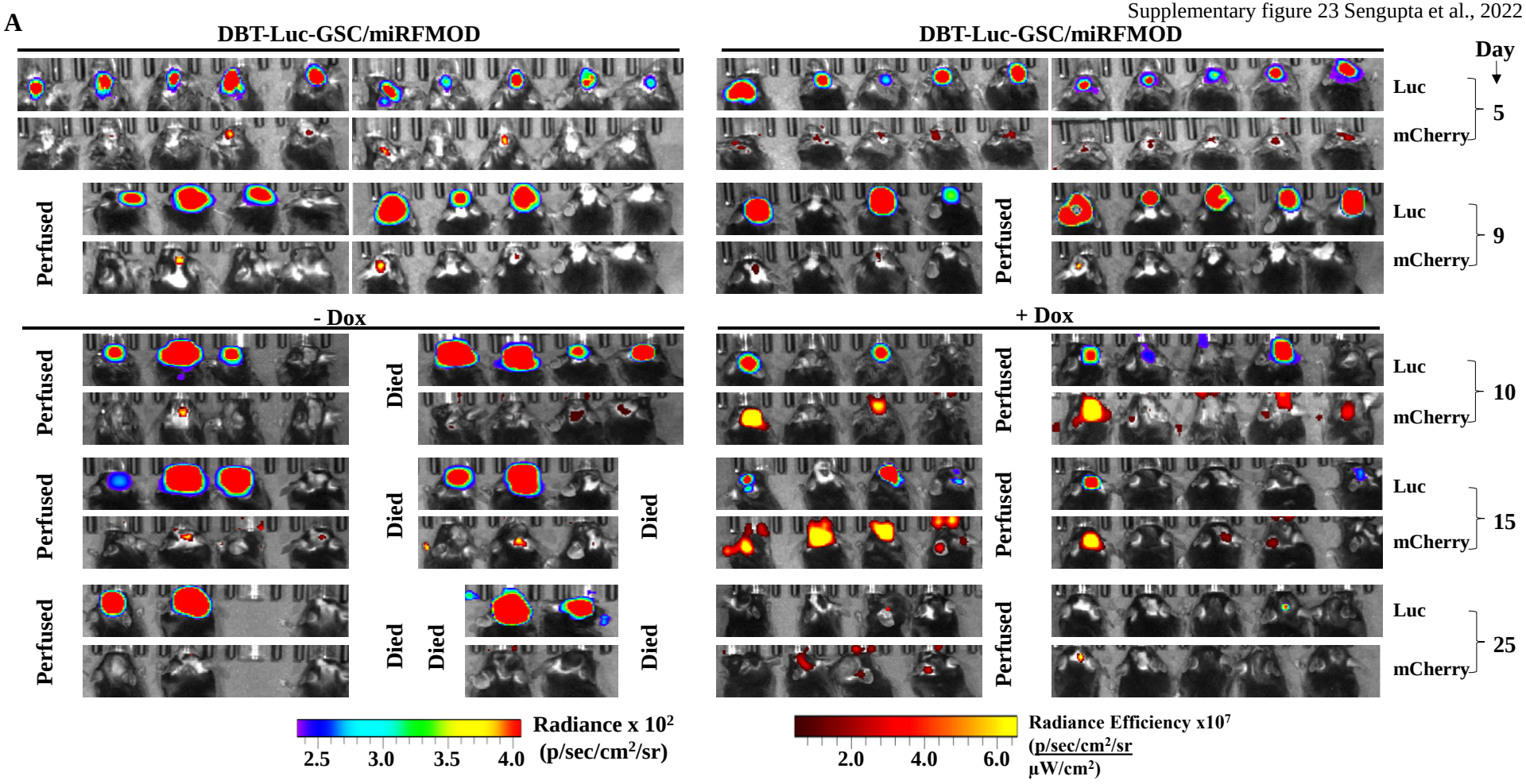
A
DBT-Luc-GSC/miRFMOD
DBT-Luc-GSC/miRFMOD
Day
Luc
mCherry
5
9
10
15
25
Perfused
Died
- Dox
+ Dox
Radiance x 10²
(p/sec/cm²/sr)
2.5
3.0
3.5
4.0
Radiance Efficiency x10⁷
(p/sec/cm²/sr
µW/cm²)
2.0
4.0
6.0

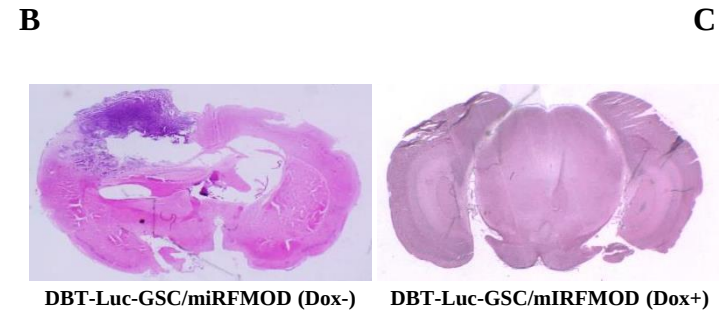
B
DBT-Luc-GSC/miRFMOD (Dox-)
DBT-Luc-GSC/mIRFMOD (Dox+)

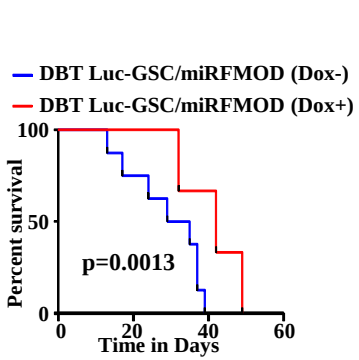
C
DBT Luc-GSC/miRFMOD (Dox-)
DBT Luc-GSC/miRFMOD (Dox+)
Percent survival
100
50
0
p=0.0013
0
20
40
60
Time in Days

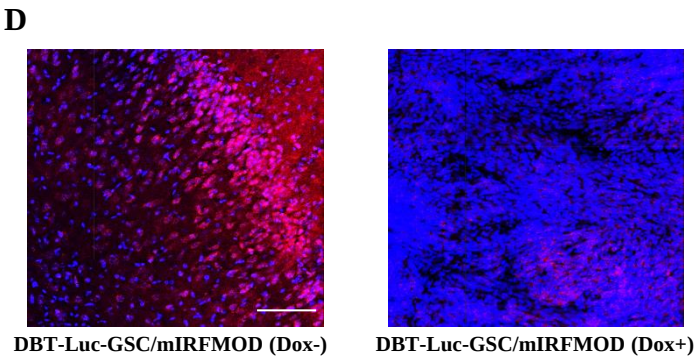
D
DBT-Luc-GSC/mIRFMOD (Dox-)
DBT-Luc-GSC/mIRFMOD (Dox+)

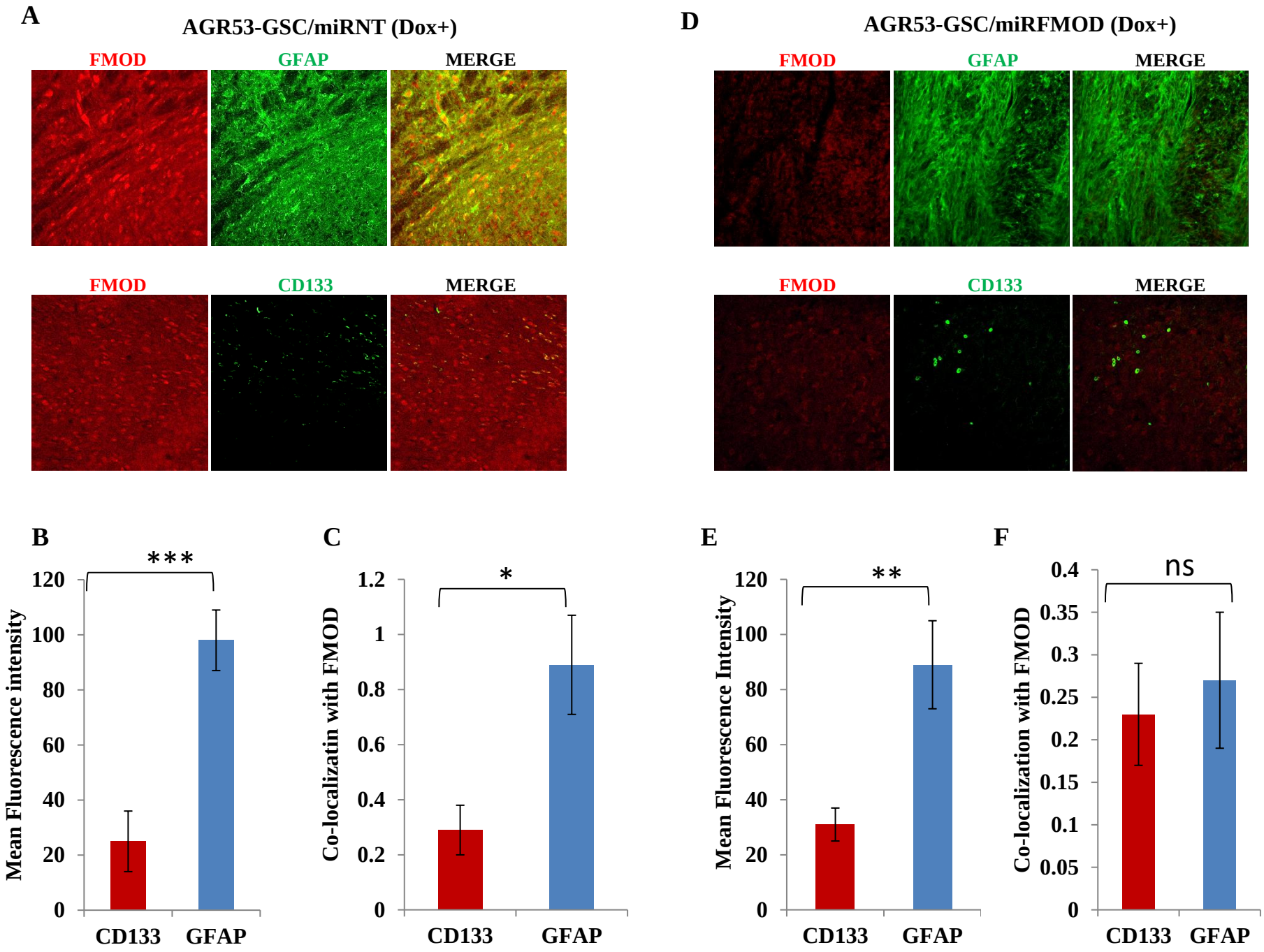
A
AGR53-GSC/miRNT (Dox+)
FMOD
GFAP
MERGE
FMOD
CD133
MERGE
D
AGR53-GSC/miRFMOD (Dox+)
FMOD
GFAP
MERGE
FMOD
CD133
MERGE
B
***
Mean Fluorescence intensity
120
100
80
60
40
20
0
CD133
GFAP
C
*
Co-localizatin with FMOD
1.2
1
0.8
0.6
0.4
0.2
0
CD133
GFAP
E
**
Mean Fluorescence Intensity
120
100
80
60
40
20
0
CD133
GFAP
F
ns
Co-localization with FMOD
0.4
0.35
0.3
0.25
0.2
0.15
0.1
0.05
0
CD133
GFAP

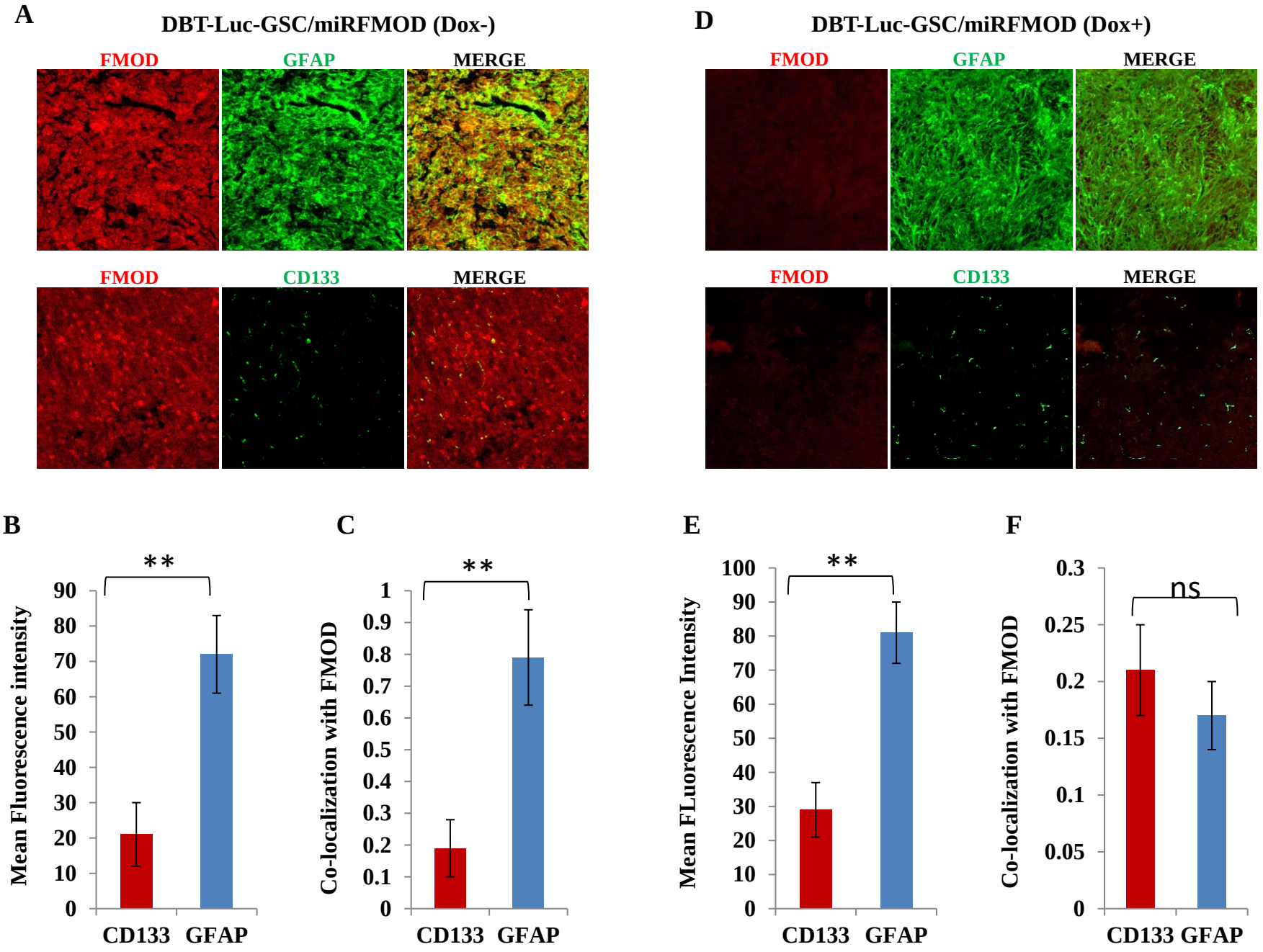
A
DBT-Luc-GSC/miRFMOD (Dox-)
FMOD
GFAP
MERGE
FMOD
CD133
MERGE
D
DBT-Luc-GSC/miRFMOD (Dox+)
FMOD
GFAP
MERGE
FMOD
CD133
MERGE
B
**
Mean Fluorescence intensity
90
80
70
60
50
40
30
20
10
0
CD133
GFAP
C
**
Co-localization with FMOD
1
0.9
0.8
0.7
0.6
0.5
0.4
0.3
0.2
0.1
0
CD133
GFAP
E
**
Mean FLuorescence Intensity
100
90
80
70
60
50
40
30
20
10
0
CD133
GFAP
F
ns
Co-localization with FMOD
0.3
0.25
0.2
0.15
0.1
0.05
0
CD133
GFAP

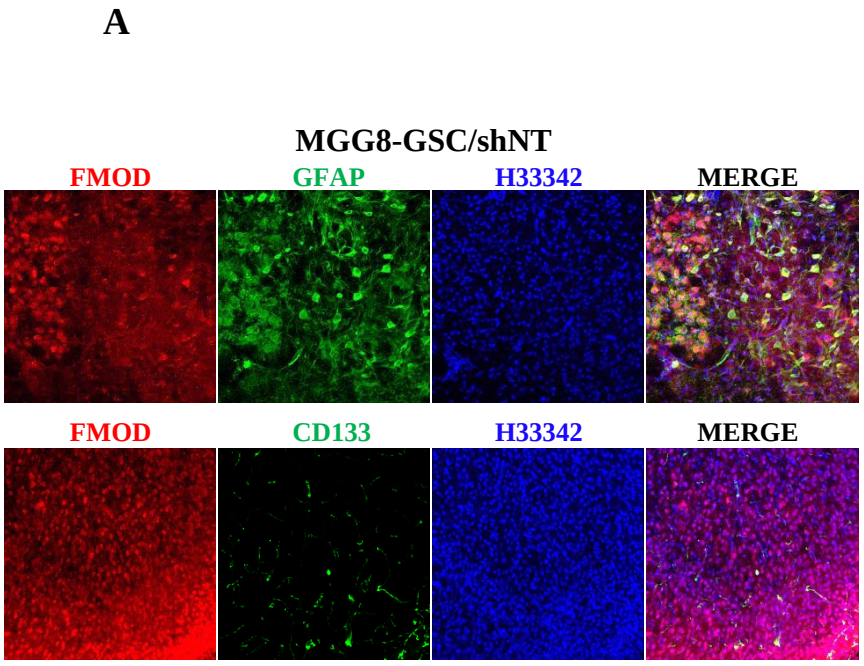
A
MGG8-GSC/shNT
FMOD
GFAP
H33342
MERGE
FMOD
CD133
H33342
MERGE

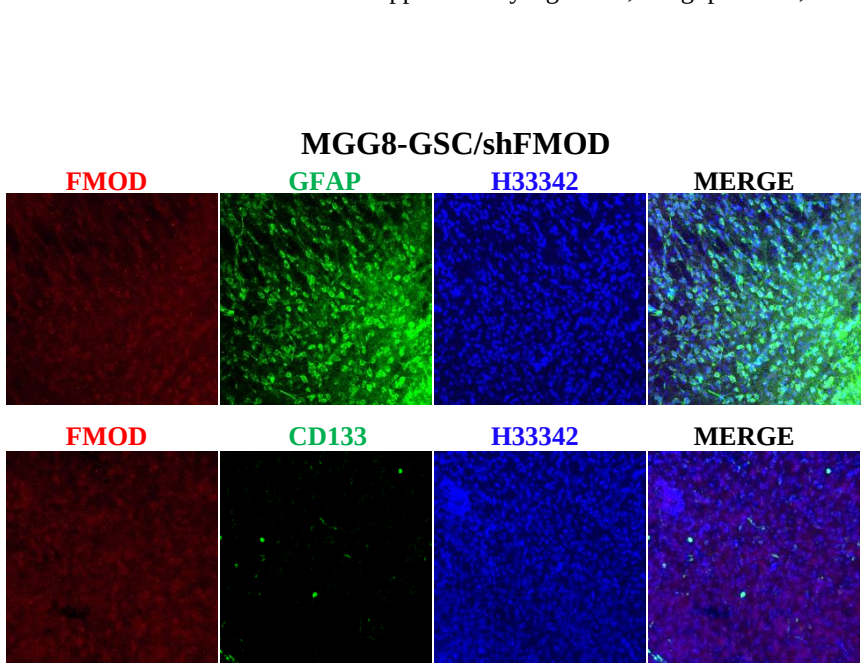
D
MGG8-GSC/shFMOD
FMOD
GFAP
H33342
MERGE
FMOD
CD133
H33342
MERGE

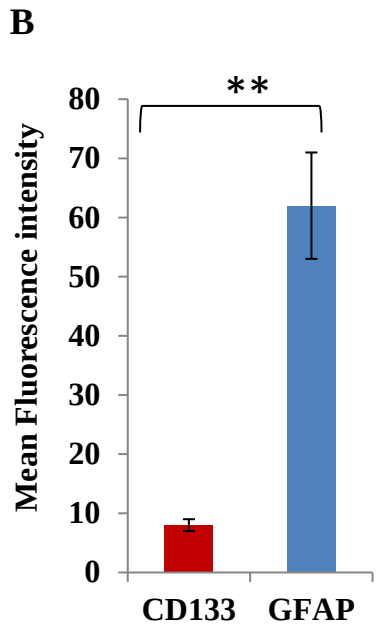
B
Mean Fluorescence intensity
80
70
60
50
40
30
20
10
0
**
CD133
GFAP

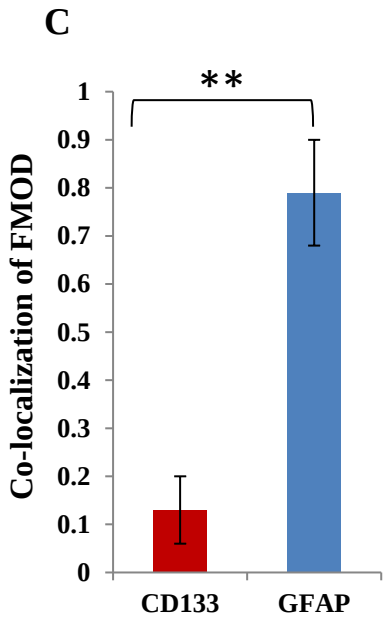
C
Co-localization of FMOD
1
0.9
0.8
0.7
0.6
0.5
0.4
0.3
0.2
0.1
0
**
CD133
GFAP

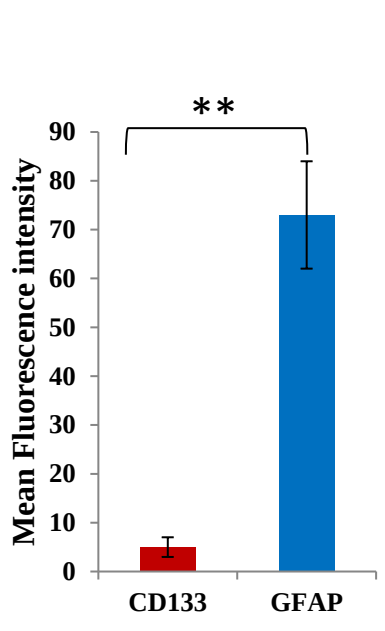
E
Mean Fluorescence intensity
90
80
70
60
50
40
30
20
10
0
**
CD133
GFAP

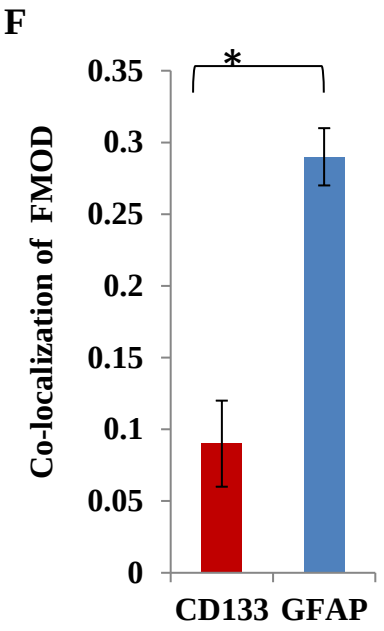
F
Co-localization of FMOD
0.35
0.3
0.25
0.2
0.15
0.1
0.05
0
*
CD133
GFAP

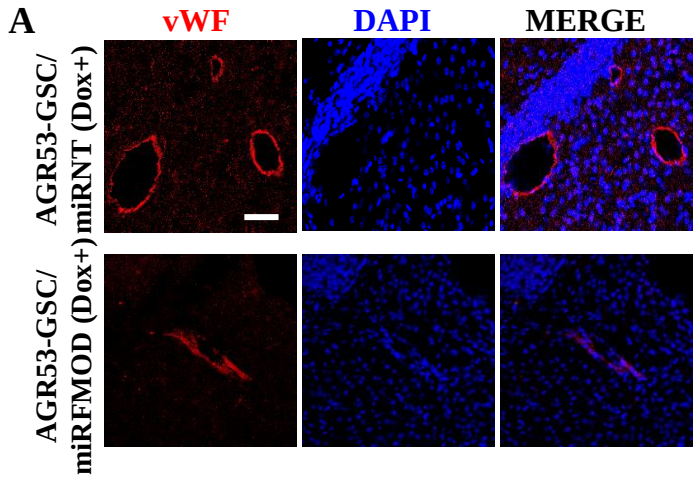
A
vWF
DAPI
MERGE
AGR53-GSC/ miRNT (Dox+)
AGR53-GSC/ miRFMOD (Dox+)

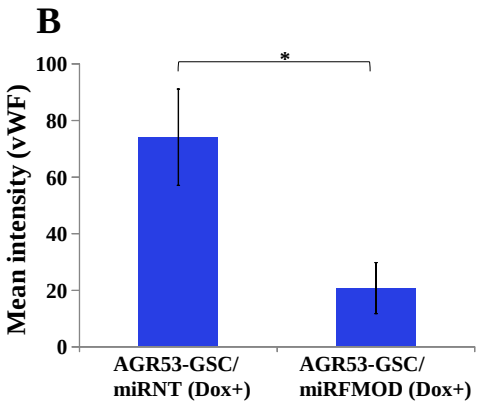
B
Mean intensity (vWF)
100
80
60
40
20
0
*
AGR53-GSC/ miRNT (Dox+)
AGR53-GSC/ miRFMOD (Dox+)

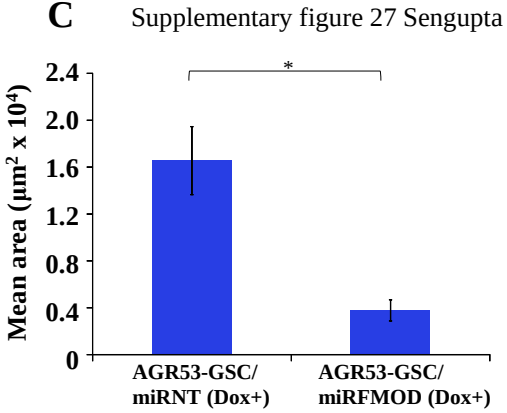
C
Mean area (µm² x 10⁴)
2.4
2.0
1.6
1.2
0.8
0.4
0
*
AGR53-GSC/ miRNT (Dox+)
AGR53-GSC/ miRFMOD (Dox+)

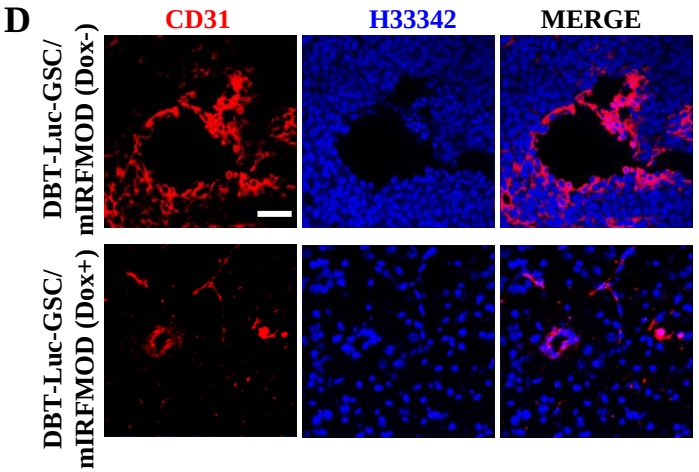
D
CD31
H33342
MERGE
DBT-Luc-GSC/ mIRFMOD (Dox-)
DBT-Luc-GSC/ mIRFMOD (Dox+)

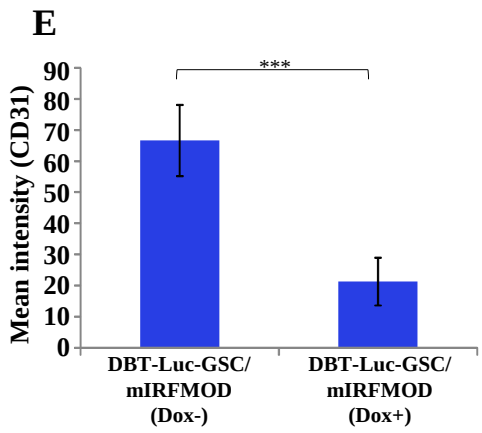
E
Mean intensity (CD31)
90
80
70
60
50
40
30
20
10
0
***
DBT-Luc-GSC/ mIRFMOD (Dox-)
DBT-Luc-GSC/ mIRFMOD (Dox+)

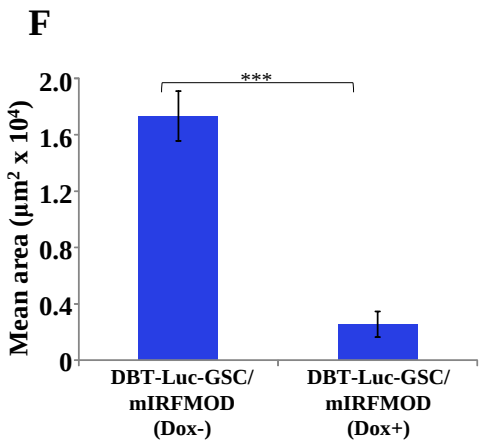
F
Mean area (µm² x 10⁴)
2.0
1.6
1.2
0.8
0.4
0
***
DBT-Luc-GSC/ mIRFMOD (Dox-)
DBT-Luc-GSC/ mIRFMOD (Dox+)

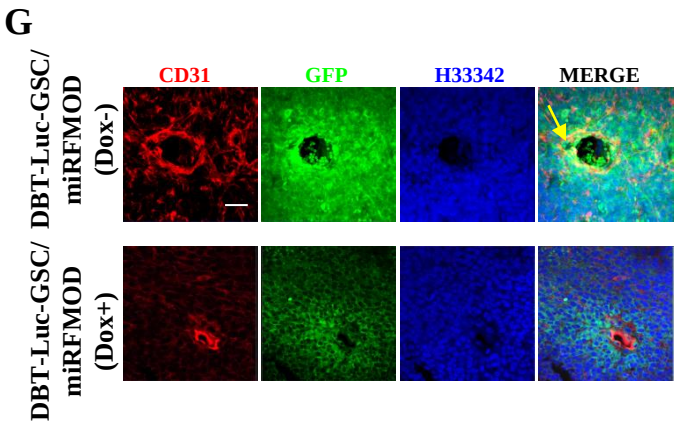
G
CD31
GFP
H33342
MERGE
DBT-Luc-GSC/ miRFMOD (Dox-)
DBT-Luc-GSC/ miRFMOD (Dox+)

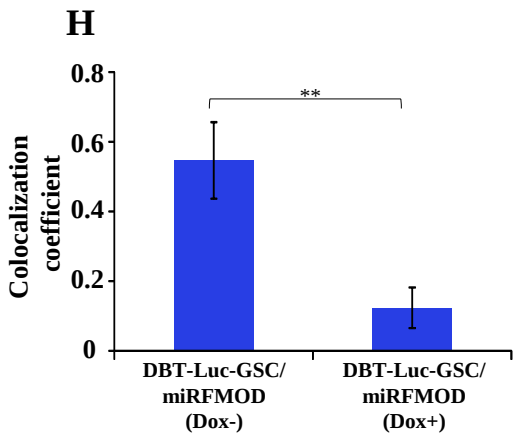
H
Colocalization coefficient
0.8
0.6
0.4
0.2
0
**
DBT-Luc-GSC/ miRFMOD (Dox-)
DBT-Luc-GSC/ miRFMOD (Dox+)

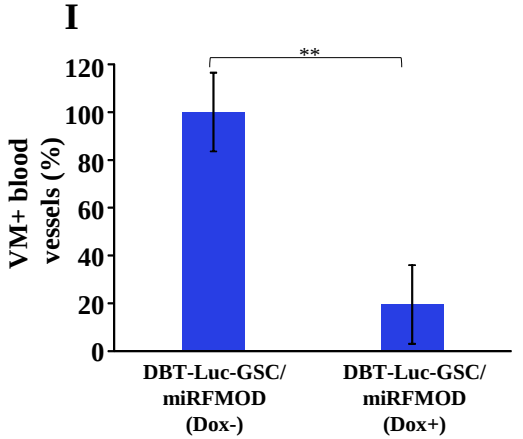
I
VM+ blood vessels (%)
120
100
80
60
40
20
0
**
DBT-Luc-GSC/ miRFMOD (Dox-)
DBT-Luc-GSC/ miRFMOD (Dox+)

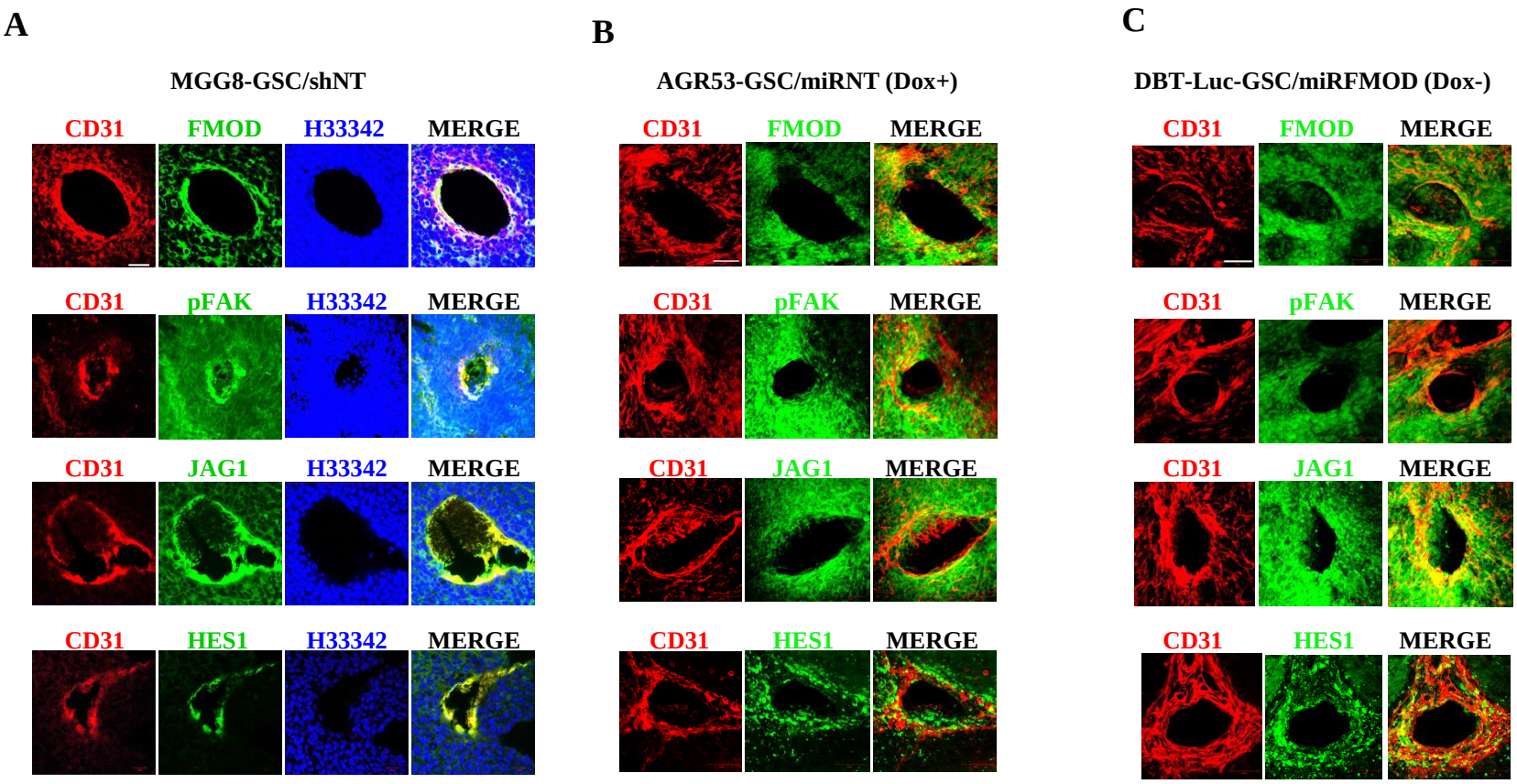
A
MGG8-GSC/shNT
CD31
FMOD
H33342
MERGE
CD31
pFAK
H33342
MERGE
CD31
JAG1
H33342
MERGE
CD31
HES1
H33342
MERGE
B
AGR53-GSC/miRNT (Dox+)
CD31
FMOD
MERGE
CD31
pFAK
MERGE
CD31
JAG1
MERGE
CD31
HES1
MERGE
C
DBT-Luc-GSC/miRFMOD (Dox-)
CD31
FMOD
MERGE
CD31
pFAK
MERGE
CD31
JAG1
MERGE
CD31
HES1
MERGE